# Effects of oxygen concentration on rapidly mixed type tubular flame combustion

## 急速混合型管状火炎燃焼に及ぼす酸素濃度の影響

学位取得年月　2012 年 9 月

石 保禄

**Doctoral Dissertation**

# Effects of oxygen concentration on rapidly mixed type tubular flame combustion

## (急速混合型管状火炎燃焼に及ぼす酸素濃度の影響)

by

Shi, Baolu

Mechanical Systems Engineering

Graduate School of Engineering

Hiroshima University, September, 2012

# CONTENTS

# Nomenclature

---

## Chap. 2: Experimental and Numerical Methods

| | |
|---|---|
| $A$ | cross-sectional area of the stream tube |
| | pre-exponential factor |
| $A_T$ | total sectional area of the tangential inlet slits |
| $c_p$ | constant-pressure heat capacity of the mixture |
| $c_{pk}$ | constant pressure heat capacity of the *k*th species |
| $D_e$ | exit throat diameter |
| $D_k^T$ | thermal diffusion coefficient for species *k* |
| $D_o$ | diameter of the main section of a swirl burner |
| $E_A$ | activation energy |
| $G_A$ | axial momenta |
| $G_w$ | angular momenta |
| $h_k$ | specific enthalpy of the *k*th species |
| $k_f$ | forward rate coefficient |
| L | quartz tube length |
| $\lambda$ | thermal conductivity of the mixture |
| $\dot{M}$ | mass flow rate |
| $p$ | static pressure in a cross section of the burner |
| $P$ | pressure |
| $R$ | radius of the burner exit |
| | universal gas constant in Chap.2 |
| $\rho$ | fluid density |

| | |
|---|---|
| $S_w$ | swirling number |
| $T$ | temperature |
| $u$ | velocity of the fluid mixture |
| $U$ | axial component of the velocity |
| $V_k$ | diffusion velocity of the *k*th species |
| $\upsilon_k$ | ordinary diffusion velocity |
| $W$ | tangential component of the velocity |
| W | slit width |
| $\bar{W}$ | mean molecular weight of the mixture |
| $W_j$ | molar mass of species *j* |
| $W_k$ | molecular weight of the *k*th species |
| $\dot{w}_k$ | molar rate of production by chemical reaction of the *k*th species per unit volume |
| $\omega_k$ | thermal diffusion velocity |
| $Y_k$ | mass fraction of the *k*th species |
| $X_k$ | mole fraction of the *k*th species |

### Chap. 3: Flame Characeristics of Rapidly Mixed Oxygen Enhanced Tubular Flame Combustion

| | |
|---|---|
| $A_S$ | section area of the throat |
| $\alpha_{nm}$ | the m-th solution for $dJ/dx = 0$ |
| $\beta$ | oxygen mole fraction in oxidizer |
| | temperature exponent |

| | |
|---|---|
| $C$ | sound speed (m/s) |
| $f$ | frequency of acoustic resonance |
| $f_0$ | frequency of Helmholtz resonance |
| $\Phi$ | equivalence ratio |
| $J_n$ | Bessel function of order n |
| $l$ | length of the combustor |
| $\Delta l$ | correction value for open exit |
| $L_S$ | length of the throat |
| $m$ | order of radial mode (=0,1,2, …) |
| $n$ | order of circumferential mode (=0,1,2, …) |
| $n_z$ | order of axial mode (=1,2, …) |
| $P_0$ | reference value of sound pressure level |
| $Q$ | flow rate |
| $r$ | burner radius |
| $V_C$ | volume of the Helmholtz resonator |

## Chap. 4 Numerical Calculation of Burning Velocities and Chemical Reaction Time

| | |
|---|---|
| $\delta_L$ | laminar flame thickness |
| $S_u$ | laminar burning velocity |
| $\tau_m$ | mixing time |
| $\tau_r$ | reaction time |
| $T_i$ | initial temperature of pre-mixture at inlet |
| $T_o$ | temperature of products at outlet |
| $T_b$ | burned gas temperature |
| $T_u$ | unburned gas temperature |

| | |
|---|---|
| $V_\mathrm{i}$ | axial velocity of pre-mixture at inlet |
| $V_\mathrm{o}$ | axial velocity of products at outlet |
| $x$ | length of calculation domain in Chemkin-Pro |

## Chap. 5 Mixing Process Analysis in Rapidly Mixed Type Tubular Flame Burner

| | |
|---|---|
| $a$ | velocity gradient |
| $D_{\mathrm{CH_4\text{-}O_2}}$ | mass diffusivity of methane/oxygen |
| $\delta$ | boundary layer thickness, measured length |
| $\delta_m$ | mixing layer thickness |
| $\Psi$ | stream function |
| $\Psi_0$ | outer stream line |
| $\Psi_\mathrm{i}$ | inner stream line |
| $K_0$ | coefficient of mixing layer thickness in boundary layer type flow |
| $K_2$ | coefficient of mixing layer thickness in axisymmetric flow |
| $r$ | radius |
| $r_0$ | outer radius |
| $r_\mathrm{i}$ | inner radius |
| $\tilde{r}$ | average radius |
| $\nu$ | kinematic viscosity |
| $V_t$ | injection velocity |
| $x$ | circumferential distance from the start point in flow visualization<br>distance from the starting point in the boundary layer thickness equation |
| Z | axial distance |

## Chap. 6 Discussion on the Requirement for Rapidly Mixed Oxygen Enhanced Tubular Flame Combustion

| | |
|---|---|
| $\lambda_1$ | width of the seeded flow in W=1 mm |
| $\lambda_2$ | width of the seeded flow in W=2 mm |
| $D_a$ | Damkohler Number |

# Chapter 1 Introductions

## 1.1 Introduction

Combustion certainly affects almost every aspect of human activities, from heating and lighting our homes to powering the various modes of transportation vehicles. As an important branch, combustion science and technology has been well studied from fundamental understanding to diverse applications. As a consequence of increased population and expansion of social development, human society has to face increasing challenges, say energy shortage, environmental pollution. According to the International Energy Agency (IEA), of the current total energy consumption over 80% is produced from fossil fuels [1]. While the rise in fossil fuel consumption, especially those with high carbon content such as coal, oil and other heavy hydrocarbons has led to increasing emissions of carbon dioxide which is believed to be responsible for global warming [2].

In order to mitigate the growing energy crisis as well as increasing $CO_2$ emissions, efficiency improvements must be put at the forefront of the effort to conserve resources and reduce the impact of energy consumption on the environment; on the other hand technology is expected to expand energy resources and the utilization, while accommodating carbon dioxide capture and sequestration (CCS) is another primary approach to lowering the $CO_2$ emissions [2-4].

In this study, oxygen enhanced combustion is proposed aiming to save energy and hence reduce the $CO_2$ emissions. An inherently safe technique of rapidly mixed type tubular flame combustion has been experimentally examined to extend it to higher oxygen concentrations including pure oxygen.

## 1.2 Two Challenges

### 1.2.1 Energy shortage

Energy is considered as the single most important challenge facing humanity today [5]. Energy consumption rates, now and in the near future, will keep a steady increase as a result of economic growth and expanding populations in the world. According to the reference case in International Energy Outlook 2011 [6], world energy consumption will increase by 53%, from 505 quadrillion Btu in 2008 to 770 quadrillion Btu in 2035. In detail, Fig. 1.1 shows the fuel consumption history from 1990 to 2008 as well as a projection till 2035. During the following two decades, despite great growth in renewable energy and nuclear, liquid fuel, coal and natural gas remain the main energy resources whose consumption rates increase continuously.

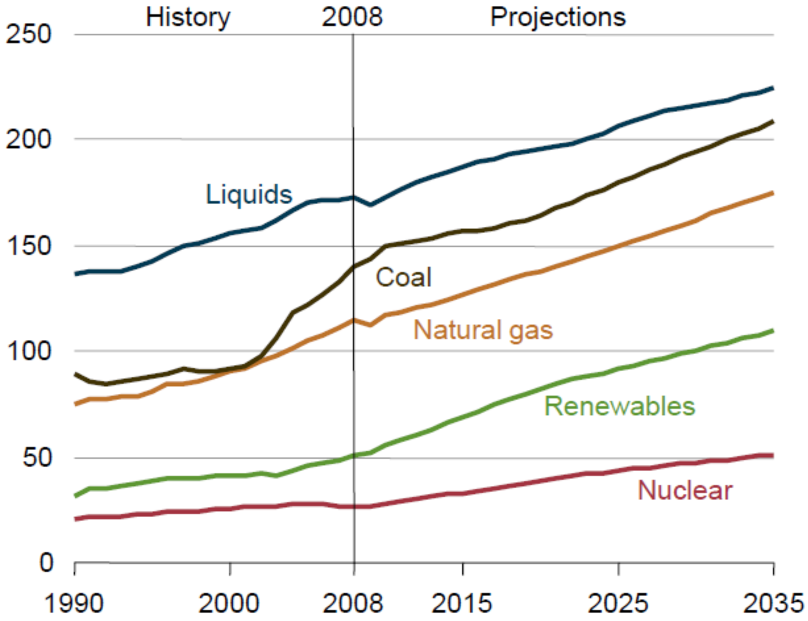

Fig. 1.1 World energy consumption by fuel 1990-2035(quadrillion Btu) [6].

If such an increasing trend would be kept, considering the limitations on fossil fuel resources and reserves, challenges of meeting the needs of a growing population are remarkably highlighted. Hence, plenty of research has been started to develop new techniques to improve efficiency and to exploit new energy resources [1-3,7-9]. Many agencies concerning energy have also been established, like IEA (International Energy Agency) [1] and EIA (U.S. Energy Information Administration) [6] et al.

A recent report, ETP 2010 ([1], drawing on the extensive expertise of IEA and its energy technology network) demonstrate the many opportunities to create a more secure and sustainable energy future. Interestingly, it analyzes two different cases: 1) Baseline scenario, assuming governments introduce no new energy and climate policies; 2) BLUE Map scenario, which sets the goal of halving global energy-related $CO_2$ emissions by 2050 (compared to 2007 levels) and examines the least-cost means of achieving that goal. An example is analyzed as shown in Fig. 1.2. In the Baseline scenario, fossil fuels in 2050 remain the major contributor of energy, despite strong growth in nuclear and renewable energy in absolute terms. The use of fossil fuels in 2050 in the BLUE Map scenario significantly reduces comparing with that in the Baseline scenario, and the share of fossil fuels in total demand is 59% lower than the Baseline scenario. In absolute terms, total demand for fossil fuels in the BLUE Map scenario in 2050 is 26% below the level of 2007. The reduction in fossil-fuel use can be attributed to energy efficiency improvement. The total demand of fossil fuels is reduced in the BLUE Map scenario, however, fossil fuels are still an important contributor to the energy system. New techniques contributing higher energy efficiency, hence promoting energy saving are in urgent demands. In this study oxygen-enriched air combustion, where oxygen is added into air to increase oxygen

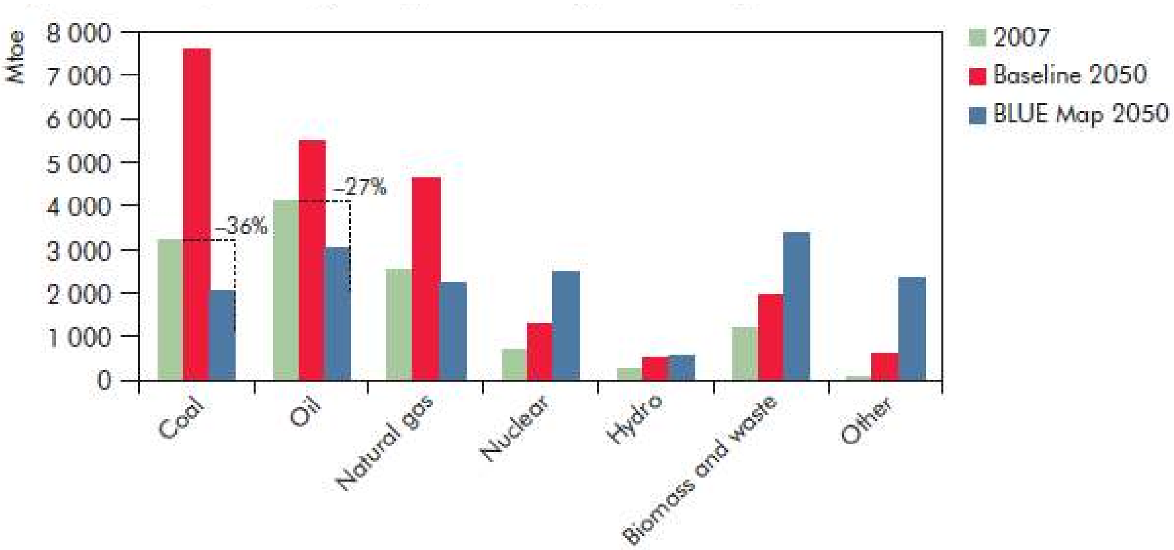

Fig. 1.2 Primary energy demand by fuel and by scenario [6].

concentration in oxidizer, is proposed to save energy.

With some percentage of increase in oxygen concentration, the efficiency of energy utilization will increase [10]. An example using methane as fuel is shown here. To obtain 1 kJ energy, for oxygen-enriched air combustion of 30 ~ 40% oxygen concentration in oxidizer, methane needs to be consumed is about 20 ~ 30 % reduced as that of methane/air. If further considering the contribution of combustor and heat recycling system, energy saving about 50% could be achieved [11]. Under higher oxygen concentration energy efficiency can be improved since some $N_2$ which acts as a diluent is replaced by $O_2$, resulting in less heat loss (carried away by $N_2$).

### 1.2.2 Global warming

#### 1.2.2.1 $CO_2$ emissions

On the other hand, global warming, caused by increasing concentrations of greenhouse gases produced by human activities such as deforestation and the burning of fossil fuels, poses an even more urgent and demanding set of questions. Greenhouse gases are defined as water ($H_2O$), carbon dioxide ($CO_2$), methane ($CH_4$), nitrous oxide ($N_2O$), chlorofluorocarbons (CFCs) and aerosols [2,3]. Among the greenhouse gases, considering the concentration, carbon dioxide has the strongest effect causing global warming, except for that of water. However, water concentration in the atmosphere is least controlled by human activities [2]. Plenty of research works have suggested that both the average global temperature and the atmospheric $CO_2$ concentration have significantly increased since the onset of industrial evolution, and they are well correlated [12].

Concerning the increasing emissions of $CO_2$, repeated warnings have been sent by like IPCC (Intergovernmental Panel on Climate Change) [13], IEA and EIA. It has been proposed that reductions of at least 50% in global $CO_2$ emissions compared to 2007 levels will need to be achieved by 2050 to limit the long-term global average temperature rise to between 2.0 $^{o}$C and 2.4 $^{o}$C [IPCC, IEA]. Though a large degree of consensus on deep cuts in $CO_2$ emissions, difficulties still exist. ETP 2010 highlights innovative policies and actions that warrant thoughtful consideration and broader application, including low-carbon technologies, financing, behavioral change, the transferring of technologies among developed and emerging economies, and discusses the environmental impacts of key energy technologies [1].

Figure 1.3 shows the ETP scenarios results illustrating the global $CO_2$ emissions in 2030 and 2050. It is seen that if the government took no new energy and climate policies (Baseline) the total $CO_2$ emissions will increase dramatically. While if effective solutions were taken (BLUE Map), it is expected that the global $CO_2$ emissions could be cut its own emissions by 50%.

Different sectors contributing $CO_2$ emissions have also been listed and examined the potential to reduce $CO_2$ emissions. Among them, transport, industry and power generation are three main contributors, which are expected to exhaust less $CO_2$ emissions in future, especially in the field of power generation. Nowadays and in near future, transport and power generation will be mainly realized by the form of combustion. Hence the energy utilization efficiency in combustion is a key factor to save energy and hence reduces the $CO_2$ emissions.

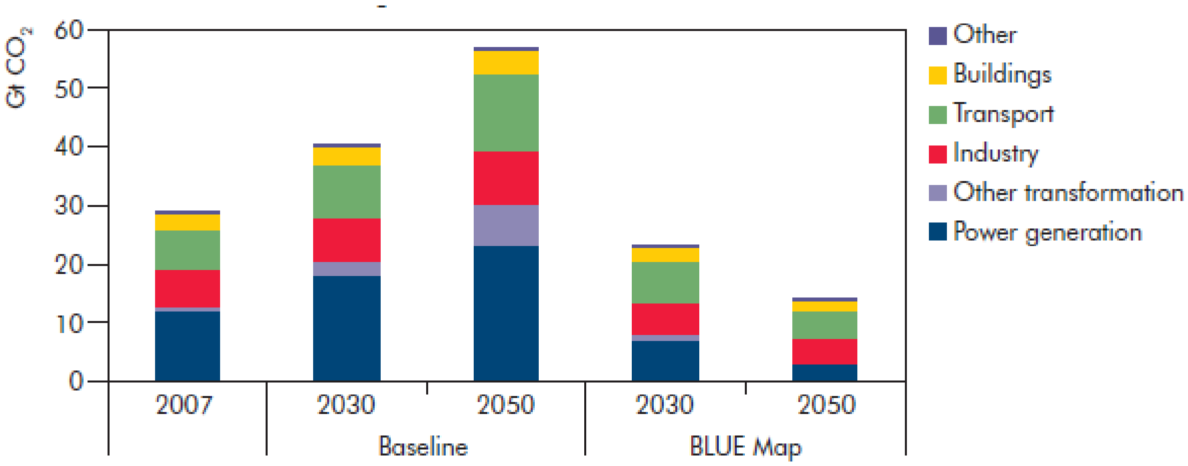

Fig.1.3 Global $CO_2$ emissions in the Baseline and BLUE Map scenarios [1].

#### 1.2.2.2 CCS

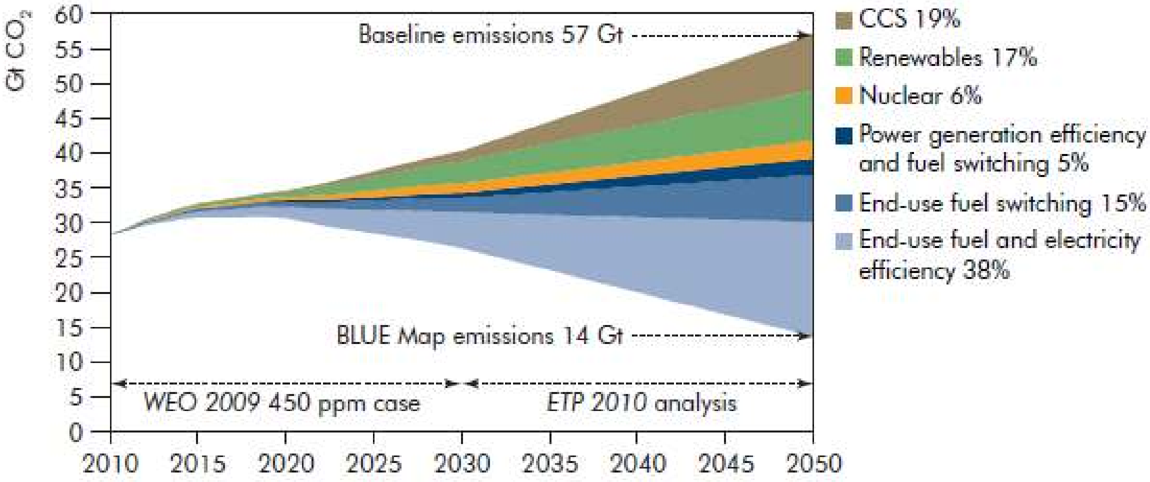

Fig. 1.4 Key technologies for reducing $CO_2$ emissions under the BLUE Map scenario [1].

On the other hand, as shown in Fig. 1.4, IEA has proposed a series of technologies for lowering the $CO_2$ emissions including improvement in energy conversion and utilization efficiencies, carbon dioxide capture and sequestration (CCS) and expanding the use of renewable resources and nuclear energy. It should be noted that the CCS technique will play the second most important role in reducing the $CO_2$ emissions in 2050, which may become one of the most effective methods.

Liquid fuel, coal and natural gas have been and will remain the major energy resources in the long term, which will result in a continuous increase of $CO_2$ emissions. Consequently, many techniques have been proposed to implement CCS which mainly includes pre-combustion capture, post combustion capture and oxy-fuel combustion [3,14]. The number of large-scale integrated CCS projects in operation or under construction is increasing all over the world [12,15]. And specialized research centers like the Global CCS Institute [16], Carbon Capture and Sequestration Technologies

Program at MIT [17] have been established to bring together projects, policy-makers and researchers in an effort to overcome challenges facing CCS.

The technology for pre-combustion capture is widely applied for fuel either gasified or reform to syngas, a mixture of carbon monoxide and hydrogen. The resulting syngas then is shifted into $CO_2$ and $H_2$ by shifting carbon monoxide with steam [3]. In post combustion capture, the $CO_2$ is removed after combustion of the fossil fuel. The technology is well understood and is currently used in fossil-fuel burning power plants and other industrial applications [18-21]. In oxy-fuel combustion, pure oxygen ($O_2$) or a mixture of $O_2$ and recycled flue gas is used as the oxidizer, resulting high $CO_2$ concentration products (usually $CO_2$ and $H_2O$) which greatly promotes $CO_2$ capture.

Many research works concerning oxy-fuel combustion have been made aiming to promote CCS technique. Heil et al. [22] experimentally investigated the chemical effects of high $CO_2$ concentration during oxy-fuel combustion of methane with the flameless combustion furnace. Amato et al. [23] analyzed the CO and $O_2$ emissions in $CH_4/CO_2/O_2$ flames. Coal, as the continuously dominant fuel in terms of power generation has been proposed to be burned in a $CO_2/O_2$ mixture, and a lot of researches have been done on oxy-fuel combustion of pulverized coal concerning the lean flammability, stabilization and reaction kinetics et al. [3, 24]. Oxy-fuel flame characteristics in a gas turbine model combustor have also been well studied by Kutne [25].

While, recently pure oxygen combustion has received keen interest from a viewpoint of atmospheric environment protection. Since products from combustion of hydrocarbon fuels are distinctly identified as a severe source of environmental damage; carbon dioxide is the main source that causes global greenhouse effects, while $NO_x$ is a major contributor of photochemical smog and ozone in the urban air. Consequently, accommodating carbon dioxide capture and sequestration (CCS) and minimizing $NO_x$ emission have become two important topics in combustion. Pure oxygen is one promising approach for low-cost CCS combined with reduction of $NO_x$ emissions [7, 26], since $NO_x$ formation through the air containing nitrogen is completely inhibited, and in addition, carbon dioxide can be easily captured and sequestrated. And in this study, we will also investigate the pure oxygen combustion which accommodates the CCS technique.

## 1.3 Oxygen enhanced combustion

### 1.3.1 Oxygen-enriched air

In a wide variety of industrial heating applications high-purity oxygen has been added to replace part or all of the air, known as oxygen enhanced combustion, which advances the combustion processes [27, 28]. Typical applications include metal heating and melting, glass melting and waste incineration [7]. There are four common methods for oxygen enhanced combustion, including: (1) adding $O_2$ into the airstream, (2) injecting $O_2$ into the air/fuel flame, (3) replacing the combustion air with high-purity $O_2$, and (4) separately providing combustion air and $O_2$ to the burner [7]. In this study, oxygen is gradually added into air stream (type (1), oxygen-enriched air combustion) until high-purity oxygen (type (3), pure oxygen combustion).

The flame characteristics of oxygen enhanced combustion have big changes from that of air/fuel combustion: the flame temperature increases significantly by replacing the $N_2$ which acts as a diluent that reduces the flame temperature; the upper flammability limit increases; the burning velocity increases; the ignition energy reduces; ... etc. And many benefits can be realized, including: increased productivity, energy efficiency, turndown ratio, and flame stability, reduced exhaust gas volume and pollutant emissions [7]. Thus, oxygen enhanced combustion has a great potential to save energy hence consuming less fuel and lowering the carbon oxide emissions. However, under high oxygen concentration, due to intense reaction and high burning velocity, flash back even detonation may frequently occur when the combustion is conducted through a premixed mode.

### 1.3.2 Pure oxygen

During the nineteenth and twentieth centuries, modern pure oxygen combustion techniques have been developed and they have been widely used in industries, including glass and ceramic manufactures as well as in the melting and/or cutting processes in steel-works.

Besides the merits of environmental protection as previously introduced, comparing with conventional air-firing combustion, pure oxygen combustion also offers a number of technical advantages in terms of flame temperature, thermal efficiency, flame stability, heat transfer and pollutant emissions [7].

The aerospace industry has done plenty of research to investigate the high-pressure combustion of liquid oxygen and liquid hydrogen, however, very limited basic research has been done, comparing with air/fuel combustion, to study the fundamental processes in atmospheric flames using pure oxygen. Harris et al. [29] describes some studies

Fig. 1.5 Oxy-methane flame; $\Phi$ =1, 190kW [29].

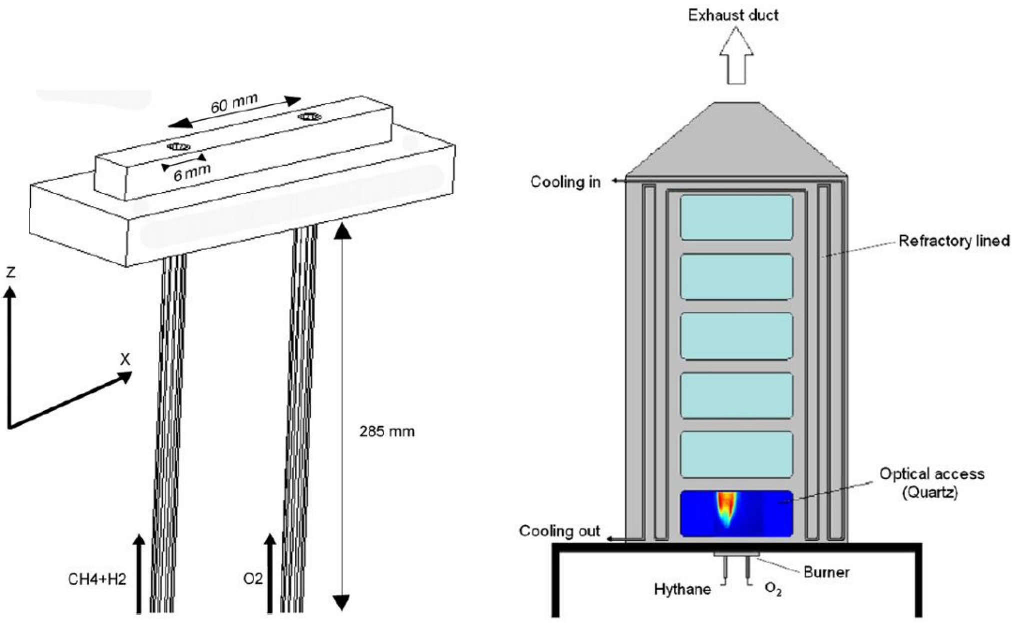

**Fig. 1.** Diagram of burner with 2 separated jets.

**Fig. 2.** Schematic of furnace model.

Fig. 1.6 Burners of two separate jets for hythane in pure oxygen combustion (left: burner diagram, right: furnace model) [30].

concerning the mixing properties and flame characteristics of methane/oxygen combustion in a jet-mixing burner. Figure 1.5 shows the methane/oxygen flame appearance at stoichiometric in Harris' study, and the mixing, flame structure, flame intensity and flame blow off were discussed [29]. With two separated jets, as shown in Fig. 1.6, Yon and Sautet [30] investigated the lame lift-off height, velocity flow and mixing of hythane in pure oxygen combustion. Beltrame et al. [31] provided a useful insight into the structure of counter-flow methane/oxygen diffusion flames. Choi et al. [32] investigated the edge flame structure in a methane/oxygen mixing layer. All these studies are based on non-premixed combustion.

It is very dangerous if pure oxygen combustion is used in premixed mode; flashback and destructive detonation may happen, which is more likely to happen than that in the oxygen-enriched air combustion. If the non-premixed mode is used as above introduced, flash back or detonation cannot occur, however, high temperature flame area is limited and hence comparing with the premixed mode, some limitations are put for the applications like heating and manufacturing. Therefore, a very safe combustion technique is eagerly desired for oxygen enhanced combustion.

In this study, an inherently safe technique is demonstrated, using the rapidly mixed tubular flame combustion. Because fuel and oxidizer are injected separately, flashback cannot occur. Although this approach has been previously demonstrated with air as the oxidizer [33], this paper presents the first application for combustion with high oxygen concentration even pure oxygen.

## 1.4 Safe technique: rapidly mixed tubular flame combustion

Considering importance of the burner system adopted in this study, some characteristics of tubular flame as well as structures of tubular flame burner are also described briefly.

A few decades ago, a tubular flame was found to be established in a rotating and a non-rotating axisymmetric flow fields [34]. The non-rotating tubular flame, usually is established in a counter-flow type tubular flame burner, in which a combustible mixture is injected inward through a porous wall, resulting in a non-rotating axisymmetric flow field inside the burner. While a swirl type tubular flame burner, as shown in Fig. 1.7, a combustible mixture is tangentially injected through a slit, resulting in a rotating axisymmetric flow field inside the burner [34].

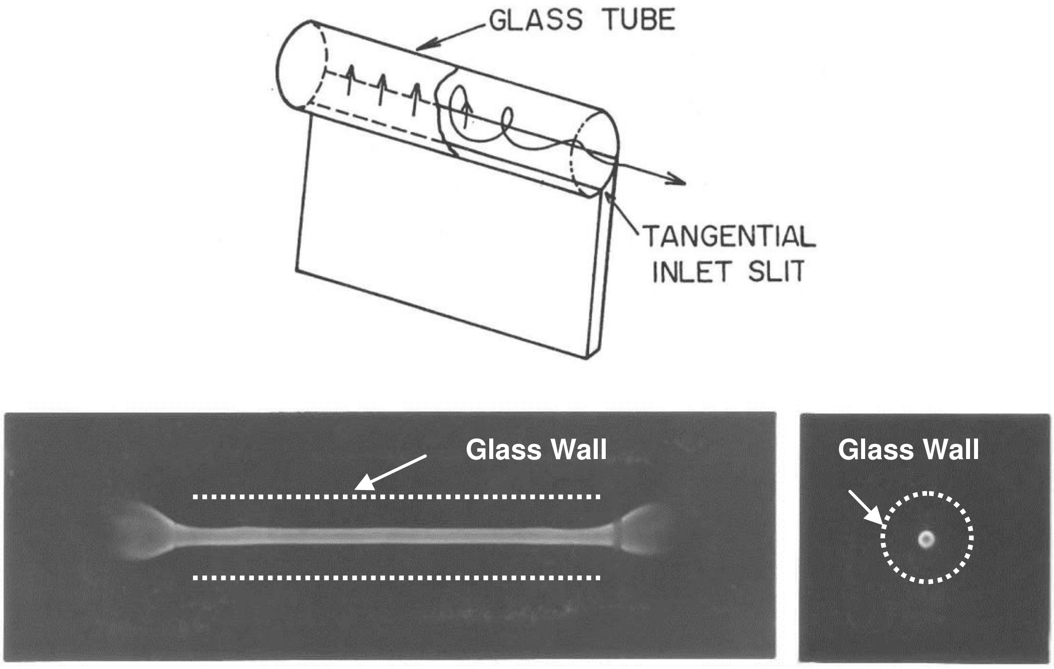

Fig. 1.7 A swirl-type tubular flame burner and the appearance of flame (inner diameter:14.3mm, length: 120mm) [34].

From a fundamental viewpoint, characteristics of tubular flame have been studied experimentally [35-43], theoretically [44-49] as well as numerically [50-54], and their early results are summarized in a review [55]. Among others, merits of tubular flame characteristics for practical use are that the temperature distribution is symmetric and the hot burned gas is surrounded by the cylindrical flame, and hence, heat loss is negligible, and in addition, inside the flame is the burned gas of low density whereas outside the flame is the unburned gas of high density, and hence, the flame is aerodynamically stable if the mixture is rotated.

Recognizing these merits, various applications have been proposed and demonstrated for determining the flammability limits [56,57], stabilizing a flame in a high speed flow [58], and obtaining a uniform and large-area laminar flame to heat iron slab or to reduce steel sheet surface [59,60].

For large heat output in practical use, however, premixed combustion is unsafe because of the occurrence of flame flashback and explosion hazard. Thus, a new concept of rapidly mixed tubular flame combustion has been proposed [33]. In this combustion technique, fuel and oxidizer are separately injected into a burner, as shown in Fig. 1.8. If fuel and oxidizer are rapidly mixed in a strong centrifugal force field in a tube, combustion with a laminar, tubular flame can be established. Since there is no supply line of combustible pre-mixture, flame flashback will never occur.

Although a great amount of study has been made for rapidly-mixed type tubular flame combustion, which is summarized in a recent review [61], the oxidizer used is limited to air or diluted air. This study aims at studying oxygen enhanced combustion operated through a rapidly mixed type tubular flame burner.

Concerns about the safety issues as well as the very high flame temperature, oxygen is gradually added into air until pure oxygen environment. As the oxygen mole fraction in the oxidizer increases, a series of changes occur, for instance, the reaction intensifies, the flame temperature and the burning velocity increase, and the inflammability limits enlarge [7], which show big differences comparing with those of fuel/air. From the fundamental point of view, it is of great interest and also importance to investigate the flame characteristics including the flame appearances, the inflammability limits, as well as the stability for various oxygen mole fractions.

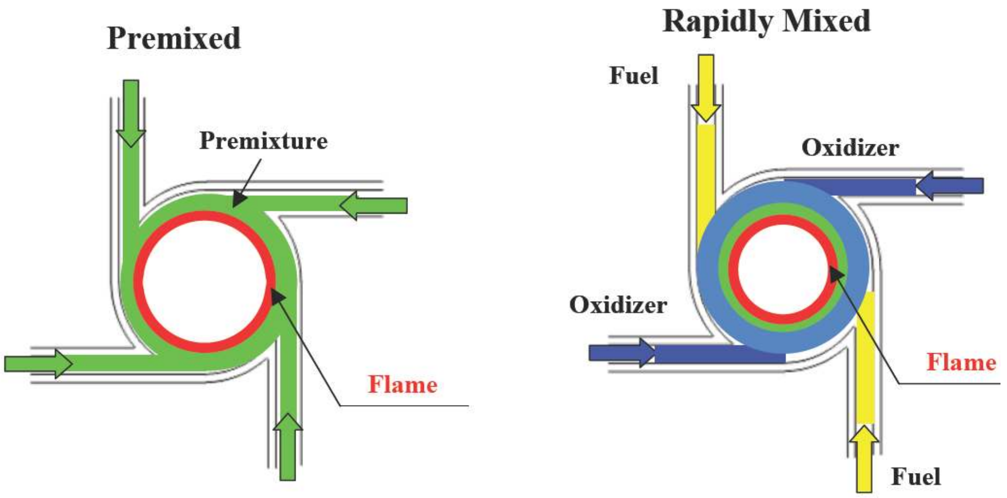

Fig. 1.8 Premixed (left) and rapidly mixed (right) type tubular flame combustion [33].

## 1.5 Objective

To improve the energy efficiency especially in combustion fields, hence reducing energy consumption and promoting environmental protection, oxygen enhanced combustion (oxygen-enriched air and pure oxygen combustion) has been proposed in this study. Due to the dangers of flash back and detonation, the inherently safe rapidly mixed type tubular flame technique has been proposed for oxygen enhanced combustion. From a fundamental viewpoint, experiments have been conducted to investigate the flame characteristics under various oxygen concentrations including pure oxygen. To further investigate the flame behaviors under very high oxygen concentration, on one hand numerical calculation concerning chemical reaction rate has been carried out through the Chemkin-PRO [62] software; on the other hand to quantitatively estimate the mixing layer thickness of fuel and oxidizer, measurements have been done with optically accessible quartz burners and PIV system. Finally the Damkohler number, which is obtained through the ratio of mixing time to reaction time, has been analyzed in detail to quantify the requirement for rapidly mixed tubular flame combustion.

In the doctoral work, the issues mentioned above will be studied in detail. The objectives of this study are as follows:

(1) to investigate the flame appearances, inflammability limits and stable combustion range under various experimental conditions including: premixed and rapidly mixed type methane/air, methane/oxygen-air in two types of rapidly mixed tubular flame burners.

(2) to investigate the flame characteristics of rapidly mixed methane/oxygen tubular flame combustion, including flame appearances, inflammability limits and stable combustion range in burners with different slit widths.

(3) to examine the burning velocity and reaction time of one dimensional laminar methane/oxygen pre-mixture.

(4) to analyze the mixing process of fuel and oxidizer in the rapidly mixed type tubular flame burner and estimate the mixing layer thickness in combustion tests.

(5) to provide the requirement for successful establishment of rapidly mixed tubular flame combustion under high oxygen concentrations.

## 1.6 Summary

In this chapter, two most important topics, energy consumption and global warming, are analyzed. Investigations related to these two problems are overviewed and an effective method, oxygen enhanced combusted in a rapidly mixed type tubular flame burner, has been proposed. For the application of this technique, issues to be studied are described. Based on these analyses, the motivations, necessities and the objectives of the present study are clearly described, which described as following:

(1) Two serious challenges for human society, energy consumption and global warming are addressed.

(2) Oxygen enhanced combustion has been considered as effective in saving energy and lowering the $CO_2$ emissions.

(3) From the viewpoint of safety, inherently safe rapidly mixed tubular flame combustion is proposed; meanwhile the tubular flame combustion has been overviewed.

(4) Flame behaviors under various oxygen mole fractions including pure oxygen are expected to be analyzed.

(5) The burning velocity and reaction rate of oxygen enhanced combustion will be calculated to yield the reaction time.

(6) The mixing process inside the tubular flame burner will be discussed by flow visualization obtained from PIV system.

(7) The requirement for successful establishment of rapidly mixed oxygen enhanced tubular flame combustion will be quantified by Damkohler number.

Furthermore, the contents and corresponding objectives of this study are described as following:

Chap. 2 **Experimental and Numerical Methods;**

Chap.3 **Flame Characeristics of Rapidly Mixed Oxygen Enhanced Tubular Flame Combustion;**

Chap.4 **Numercial Calculation of Burning Velocity and Reaction Time;**

Chap.5 **Mixing Process Analysis in the Rapidly Mixed Type Tubular Flame Burner;**

Chap.6 **Discussions on the Requirement for Rapidly Mixed Oxygen Enhanced Tubular Flame Combustion;**

Chap.7 **Conlcusions.**

# Chapter 2 Experimental and Numerical Methods

## 2.1 Introduction

This chapter gives a brief introduction about the experimental apparatus used in this study: through the tubular flame burners experiments were carried out under various oxygen mole fractions including pure oxygen in combustion tests; in order to quantitatively investigate the requirement for tubular flame establishment, the mixing process of fuel and oxidizer was measured by a PIV system with using optically accessible quartz burners of different slit widths. Hence, the tubular flame burner used in this study as well as the PIV measurement system is firstly introduced in the following.

The fuel used was methane, which was the main component of natural gas and probably the most abundant organic compound on earth. The oxidizer was a mixture of air and pure oxygen. To acquire the chemical characteristics of the methane/oxygen-air mixture, two important parameters, laminar burning velocity and reaction time, were numerically calculated through the Chemkin-PRO [62] software. The software, the calculation model and boundary conditions are also described in this chapter.

## 2.2 Experimental apparatus

A schematic drawing of the tubular flame burners used in this study is shown in Fig. 2.1. The burners, made of stainless steel, are very simple in structure, which consist of four tangential slits and a combustion tube. The fuel is injected from two parallel slits, while the oxidizer is injected from another two slits (left part). To permit viewing and photographing the flame, a round quartz window is installed at the closed end of the burner. To conduct the flame, a quartz tube is used downstream the slits. After injected from the slits, the mixture of fuel and oxidizer exits from the open side of the quartz tube and then it is ignited by a torch at the exit.

In this study, two burners of different rectangular slit widths, W=1 and 2 mm, were used, while the diameter of the burner was 16 mm and the slit length was 8 mm. Two different lengths of quartz tubes, 50 and 100 mm, were used. The inner and outer diameters of the quartz tube were 16 and 20 mm, respectively.

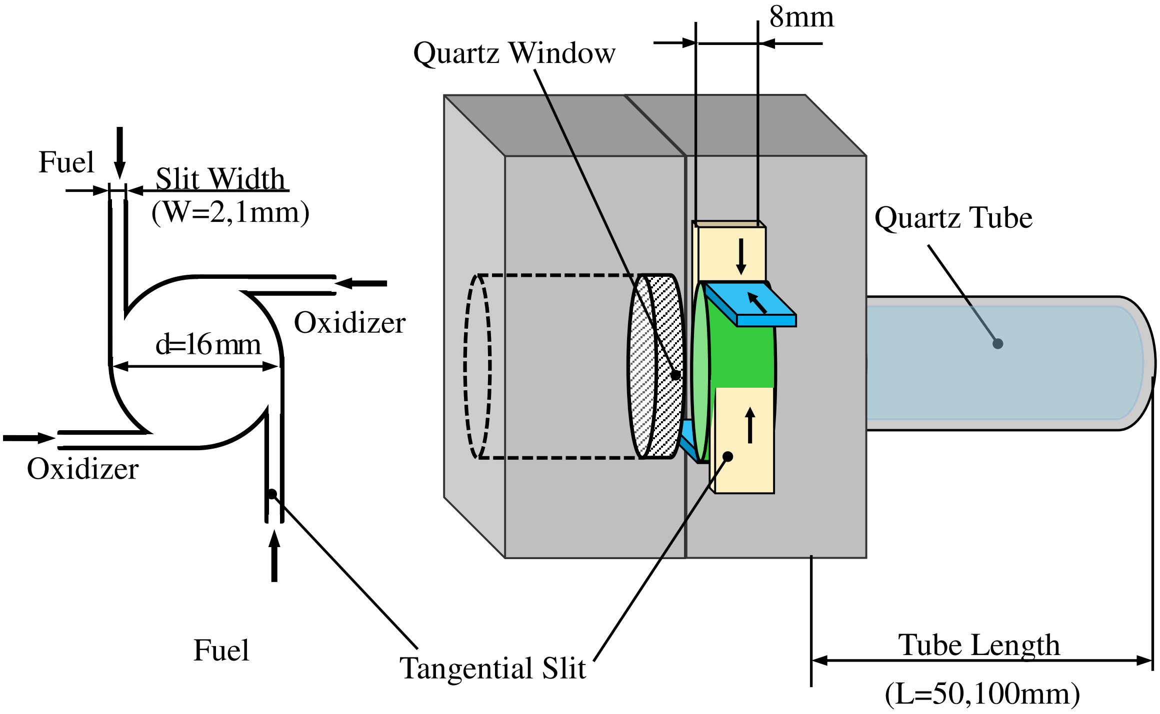

Fig. 2.1 Schematic of the tubular flame burner.

For the rapidly mixed type tubular flame burner, high injection velocities and strong swirl rates are preferable in order to promote mixing and stabilizing combustion [33]. The measurement of swirl strength is commonly accepted by the so-called swirl number ($S_w$), the definition of which was given by Beer and Chigier [62]. According to this definition, the swirl number could be obtained by measured velocity and pressure profile using the following equation:

$$S_w \equiv \frac{G_w}{RG_A} = \frac{2\pi\int_0^R \rho W U r^2 dr}{2\pi R\int_0^R \rho U^2 r dr + 2\pi R\int_0^R p r dr} \tag{2.1}$$

in which $G_w$ and $G_A$ are the angular and axial momenta, and $R$, $\rho$, $W$, $U$ and $p$ are the radius of the burner exit, the fluid density, the tangential and axial components of the velocity, and the static pressure in a cross section of the burner, respectively.

However, it is usually deficient in the detailed experimental data of velocities profiles for a swirl burner or a cyclone combustor, the swirl number has often been defined on the basis of input and exit parameters [34, 64, 65] as follows:

$$S_w \equiv \frac{G_w}{RG_A} \approx \frac{\text{Input Angular Momentum}}{D_e/2 \times \text{Exit Axial Momentum}} = \frac{\pi D_e D_o}{4A_T} \tag{2.2}$$

in which $D_o$ is the diameter of the main section of a swirl burner, $D_e$ is the exit throat diameter, and $A_T$ is the total sectional area of the tangential inlet slits. Accordingly, in this study, the swirl numbers are 6.3 and 12.6 for the burners of slit width of 2 and 1 mm, respectively. Both swirl numbers meet the requirement of larger than 5 for the establishment of tubular flame combustion [33].

Flames were photographed by a conventional video camera (Sony Digital Video Camera Recorder). Figure 2 shows direct images of the rapidly mixed tubular flame burner as well as the flame appearances. In the front view (upper left), the broken lines show the position of the tangential slits, while the dotted circle shows the burner wall and also the inner wall of the quartz tube. In the side view (upper right), the round quartz window and the quartz tube are shown.

For the supply of reactants, air is provided by air compressor; from oxygen cylinder oxygen is supplied and added into the air flow; while from methane cylinder, methane is separately, tangentially injected into the burner, as shown in the lower right. All the flow rates are metered by flow meters. Flame front is observed from the front view through the quartz window, while the downstream flame appearance is photographed from the side view.

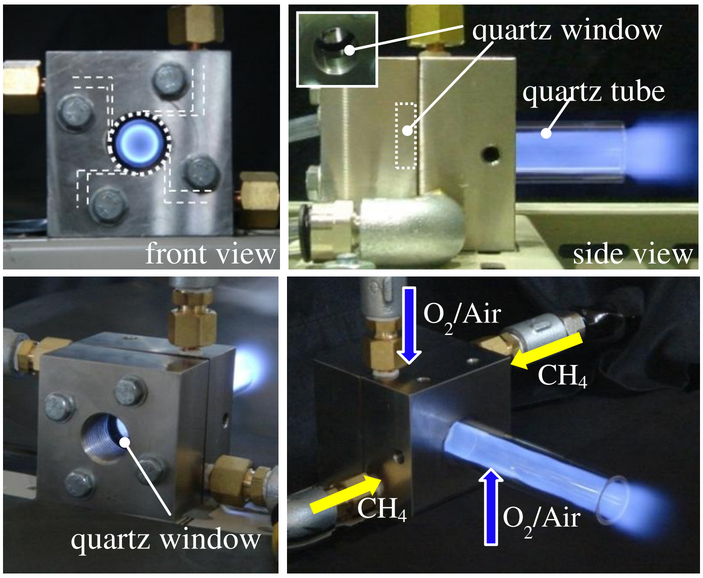

Fig. 2.2 Rapidly mixed type tubular flame burner.

In oxygen enhanced combustion tests, oscillatory combustion frequently occurs when the oxygen mole fraction is large (above 0.4). To obtain detailed information about the oscillation combustion observed in present study, pressure fluctuations were measured by using a pressure sensor (PCB, HM102A06, maximum pressure 68.95MPa, response time 0.1$\mu sec$) and a digital oscilloscope (IWATU, Wave Runner, 64kwards×4 channels). In case of being burned, the pressure sensor was settled in a quartz tube of 8 mm inner diameter which connected with the combustion tube. The pressure fluctuation was measured at a position 15 mm upward the exit of the combustion tube, as shown in Fig. 2.3. Two types of tubes, L=50 and 100 mm were used in both W=2 and 1mm burners.

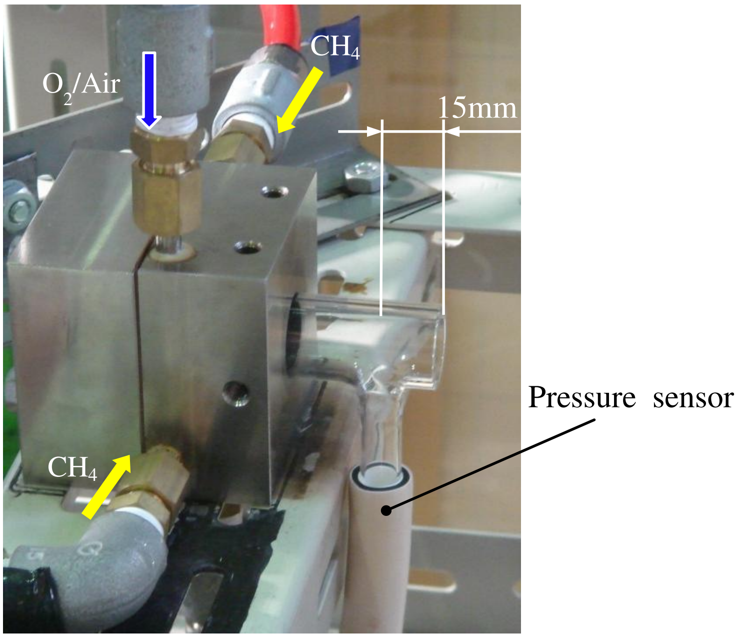

Fig. 2.3 Measurement of the oscillatory combustion.

## 2.3 PIV Measurement

Investigation on the mixing of fuel and oxidizer is very important and indispensable for the rapidly mixed tubular flame technique which demands that fuel and oxidizer should be well mixed before reaction starts. To obtain a general concept of the mixing process, a set of optically accessible quartz burners, with slit widths of 3, 2 and 1 mm, have been made. With the PIV system deep observations were made aiming at getting quantitative data for the mixing layer thickness.

### 2.3.1 Optically accessible burners

In combustion tests, different flames were observed under high oxygen mole fractions. To investigate the formation of various flames, quartz burners with the same size as those in combustion tests have been made, as Fig. 2.4 (b)~(d) shown. The slit widths are 2 and 1 mm, respectively. The inner diameter of the burner is 16 mm. A quartz burner of 3 mm slit width (Fig. 2.4 (a)) has also been made and measured for further discussion concerning mixing process.

Figure 2.4 (d) shows an image of the burner with W= 1 mm. The burner is two sides open with a total length of 120 mm. Non-seeded flow is tangentially injected into the burner through two parallel slits, while seeded flow (with MgO tracer) is injected from another two parallel slits. Here the non-seeded flow represents the fuel flow in the actual combustion tests, while the seeded flow represents the oxidizer flow in the tests. After injected into the burner, the mixing process between non-seeded flow and seeded flow is recorded by a PIV system as discussed in the following section.

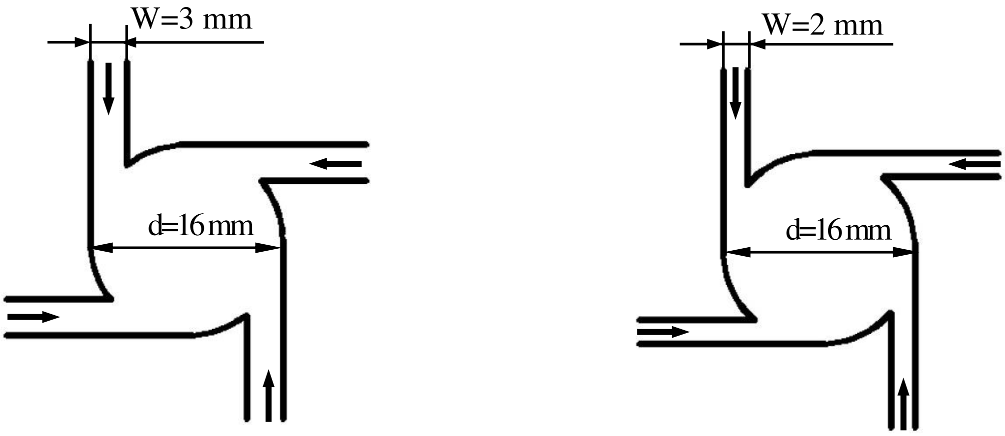

(a) W=3 mm

(b) W= 2 mm

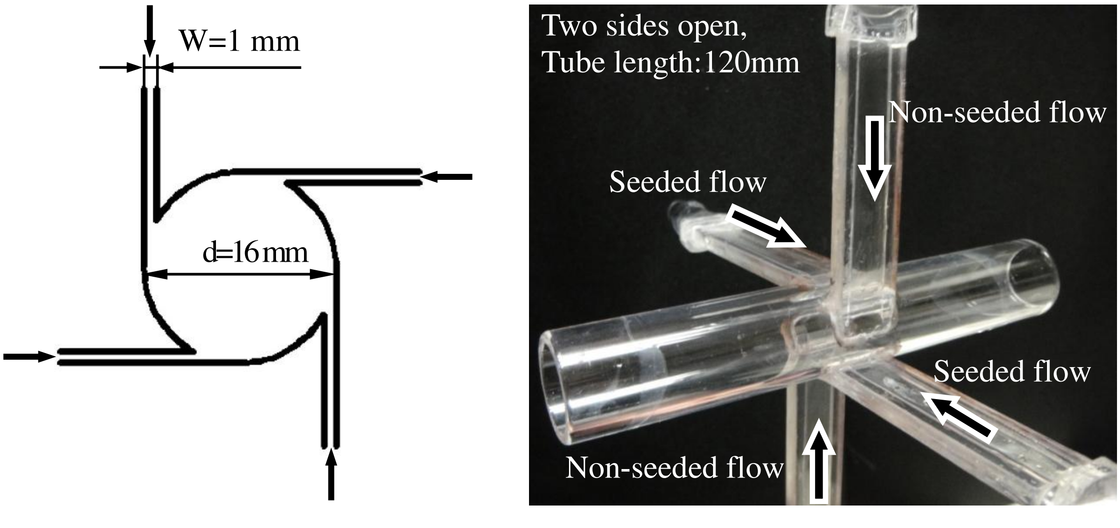

(c) W= 1 mm

(d) Burner configuration W= 1 mm

Fig. 2.4 Optically accessible quartz burners in PIV measurement:
(a) ~ (c) schematics of quartz burners of W= 3, 2 and 1mm,
(d) configuration of the burner W= 1 mm.

### 2.3.2 PIV measurement

Figure 2.5 shows the configuration of the PIV measurement system. In initial measurement, nitrogen and dry air were used; in further investigation, only dry air was used for seeded and non-seeded flows. From nitrogen cylinder and air cylinder, nitrogen and dry air were supplied and then metered by an orifice flow meter. In the orifice flow meter the gauge pressure were 0.08 MPa for both flows. Magnesium oxide (MgO) particles with a few microns in diameter were added into one stream through a particle feeder, while the other stream was the non-seeded flow.

The PIV system consists of a PIV camera (TSI), a double-pulsed Nd:YAG laser (120 mJ/pulse, 15 Hz), a host computer, and a synchronizer. Double-pulsed laser sheets were directed to the quartz burner, perpendicularly with respect to the tube axis. And the observations were made in a plane parallel to the sheet 2 mm offset the center of the slit. Since around the center area, the number of seeded particles to be illuminated by the laser sheet was small. If the laser sheet was offset, the number of particles increased, resulting in higher quality images of the mixing layer. Because a similar solution exists in the present flow field, the mixing layer thickness remains unchanged at offset positions.

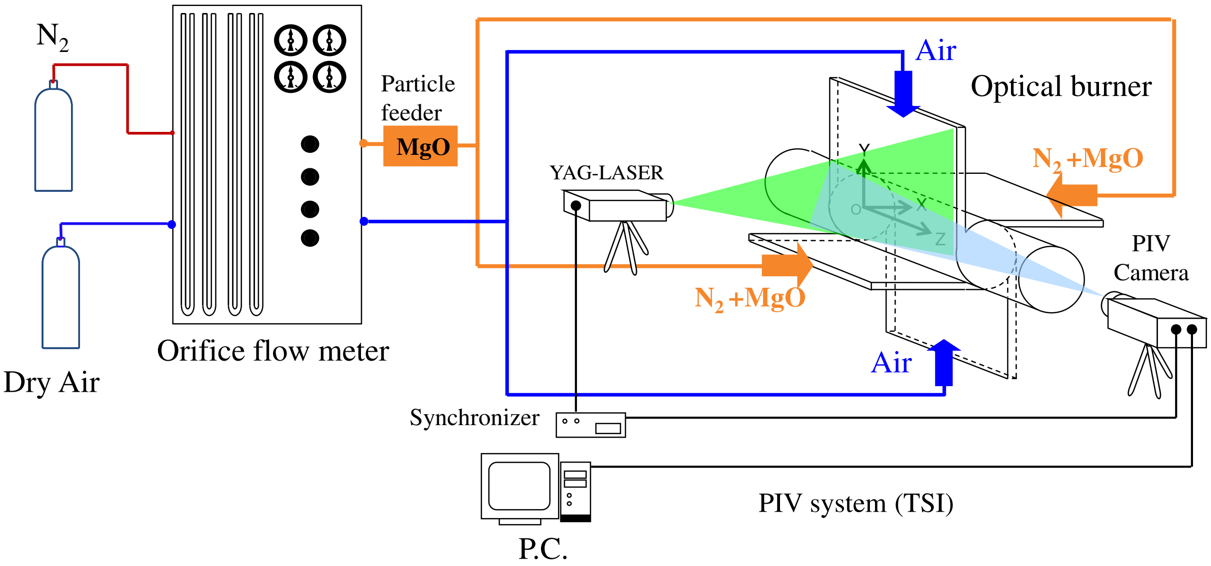

Fig. 2.5 Measurement of mixing process with a PIV system.

## 2.4 Numerical

In this chapter, the numerical calculations concerning laminar burning velocity and reaction time are discussed in detail. The calculation of the laminar burning velocities was performed by mean of simulation of the one-dimensional, planar, adiabatic, steady, unstretched, laminar flame propagation through with the software of Chemkin-PRO using the Chemkin Premix code [66, 67]. The detailed reaction scheme GRI-Mech version 3.0 [68] was used, which considered 53 species and 325 elementary reactions, including $NO_x$ kinetics. Some information about the Chemkin and GRI mechanism are briefly introduced firstly.

### 2.4.1 Modeling description

CHEMKIN software fundamentally enables the simulation of various complex chemical reactions, including ignition, shock tube, premixed flame, opposed diffusion flame and internal combustion engine, etc. Reaction Design has offered multiple products like Chemkin, Chemkin-PRO and Chemkin-CFD to satisfy unique requirements. Among them, Chemkin-PRO is specifically designed for large chemical simulation applications requiring complex mechanisms [62].

Chemkin-PRO includes a large choice of Reactor Models to meet the needs of specific industries. Its advanced solvers and full feature set support the ultimate in speed, accuracy and solution robustness. For complex models with large mechanisms, Chemkin-PRO can be over 50 times faster than previous versions of Chemkin in demanding applications. To gain key insights into kinetics dependencies, Chemkin-PRO includes the Reaction Path Analyzer. Furthermore, this software is designed to explore the uncertainties as well as predict soot and particle formation [62].

In this study we seek to determine the laminar burning velocities through Chemkin Premix code [66, 67] of the Chemkin-PRO package. This code is capable of predicting temperature and species profiles in two laminar premixed flame configurations. The first one is the burner-stabilized flame with a known mass flow rate, which is most often used for analyzing species profiles in flame experiments. The second flame configuration is the freely propagating adiabatic flame, in which there are no heat losses and the flame temperatures are computed from the energy equation.

The program accounts for finite rate chemical kinetics and multicomponent molecular transport. With appropriate governing equations and boundary conditions, the finite difference discretization and the Newton method are used for solving the boundary value problem.

The equations governing the steady, isobaric, quasi-one-dimensional flame propagation can be written as follows:

Mass continuity:

$$\dot{M} = \rho u A \tag{2.3}$$

Energy:

$$\dot{M}\frac{dT}{dx} - \frac{1}{c_p}\frac{d}{dx}(\lambda / A\frac{dT}{dx}) + \frac{A}{c_p}\sum_{k=1}^{K}\rho Y_k V_k c_{pk}\frac{dT}{dx} + \frac{A}{c_p}\sum_{k=1}^{K}\dot{w}_k h_k W_k = 0 \tag{2.4}$$

Species:

$$\dot{M}\frac{dY_k}{dx} + \frac{d}{dx}(\rho A Y_k V_k) - A\dot{w}_k W_k = 0 \qquad (k = 1,\ldots,K_g) \tag{2.5}$$

Equation of state:

$$\rho = \frac{P\bar{W}}{RT}. \tag{2.6}$$

In these equations $x$ denotes the spatial coordinate; $\dot{M}$ the mass flow rate (which is independent of $x$); $T$ the temperature; $Y_k$ the mass fraction of the $k$th species (gas species); $P$ the pressure; $u$ the velocity of the fluid mixture; $\rho$ the mass density; $W_k$ the molecular weight of the $k$th species; $\bar{W}$ the mean molecular weight of the mixture; $R$ the universal gas constant; $\lambda$ the thermal conductivity of the mixture; $c_p$ the constant-pressure heat capacity of the mixture; $c_{pk}$ the constant pressure heat capacity of the $k$th species; $\dot{w}_k$ the molar rate of production by chemical reaction of the $k$th species per unit volume; $h_k$ the specific enthalpy of the $k$th species; $V_k$ the diffusion velocity of the $k$th species; and $A$ the cross-sectional area of the stream tube encompassing the flame (normally increasing due to thermal expansion) normalized by the burner area. In this calculation, by default, the stream tube area is taken to be constant and equal to unity.

The net chemical production rate $\dot{w}_k$ of each species results from a competition between all the chemical reactions involving that species. We presume that each reaction proceeds according to the law of mass action and the forward rate coefficients are in the modified Arrhenius form,

$$k_f = AT^{\beta} Exp\left(\frac{-E_A}{RT}\right),$$

(2.7)

in which $A$ is the pre-exponential factor, $\beta$ is the temperature exponent and $E_A$ is activation energy.

Two options, mixture-averaged formulas and a multicomponent diffusion model are available to evaluate the transport properties. In current calculation, due to the importance of the thermal diffusion effects, the multicomponent diffusion model is considerably more accurate than the mixture-averaged approach. Multicomponent diffusion coefficients, thermal conductivities and thermal diffusion coefficients are computed through the solution of a system of equations involving the binary diffusion coefficients, the species mole fractions, and the thermodynamic and molecular properties of the species.

For the multicomponent formulation, the correction velocity is not required and the diffusion velocity ($V_k$) is defined as,

$$V_k = \upsilon_k + \omega_k \ , \tag{2.8}$$

in which , the ordinary diffusion velocity term ($\upsilon_k$) is given by the following equation,

$$\upsilon_k = \frac{1}{X_k \bar{W}} \sum_{j \neq k}^{K} W_j D_{k,j} \, d_j \ . \tag{2.9}$$

Here, $\bar{W}$ is the mean molar mass, $W_j$ is the molar mass of species $j$, and $d_j$ is defined as,

$$d_j = \nabla X_k + (X_k - Y_k) \frac{1}{P} \nabla P \ . \tag{2.10}$$

The thermal diffusion velocity ($\omega_k$) is given as:

$$\omega_k = \frac{D_k^{\ T}}{\rho Y_k} \frac{1}{T} \nabla T \,, \tag{2.11}$$

in which $D_k^{\ T}$ is the thermal diffusion coefficient for species *k*.

### 2.4.2 Boundary conditions

Initial and boundary conditions are assigned to define the problem environment, as shown in Fig. 2.6. At the inlet boundary, temperature (298 K), pressure (1 atm) and composition of the unburned mixture are set to define the initial condition. At the exit boundary it is specified that all gradients vanish. Because of the importance of the low molecular-weight species (like [H]), the Soret effect is taken into account, in which the species diffusive fluxes includes a thermal diffusion component.

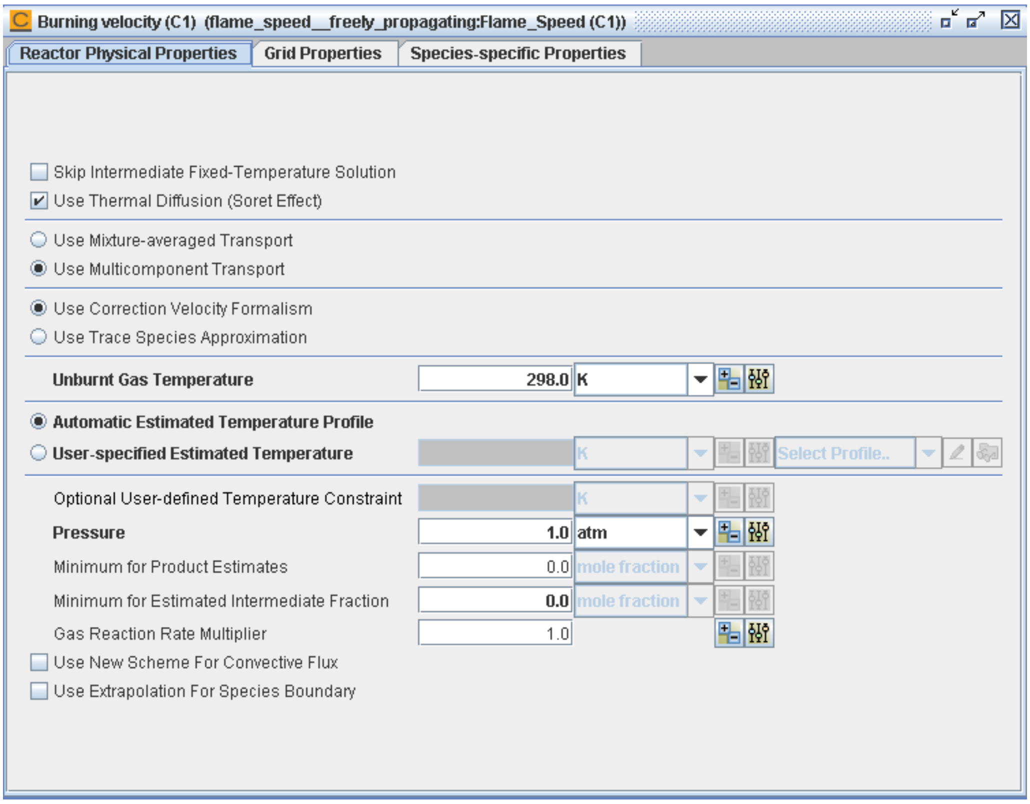

☐ Skip Intermediate Fixed-Temperature Solution
☑ Use Thermal Diffusion (Soret Effect)

○ Use Mixture-averaged Transport
● Use Multicomponent Transport

● Use Correction Velocity Formalism
○ Use Trace Species Approximation

**Unburnt Gas Temperature** 298.0 K

● **Automatic Estimated Temperature Profile**
○ **User-specified Estimated Temperature** K Select Profile..

Optional User-defined Temperature Constraint K
**Pressure** 1.0 atm
Minimum for Product Estimates 0.0 mole fraction
Minimum for Estimated Intermediate Fraction 0.0 mole fraction
Gas Reaction Rate Multiplier 1.0
☐ Use New Scheme For Convective Flux
☐ Use Extrapolation For Species Boundary

Fig. 2.6 Physical properties of the burning velocity reactor.

For freely propagating flames the total mass flow rate ( $\dot{M}$ ) is an eigenvalue and must be determined as part of the solution [69]. Therefore, an additional constraint is required, or alternatively one degree of freedom must be removed from the problem. In Chenkin-PRO it is set to fix the location of the flame by specifying and fixing the temperature at one point [62]. The distance of the point is calculated from the initial temperature profile estimation of the code, which insures that the temperature and species gradients nearly vanish at the cold boundary.

The Burning-Velocity Calculator simulates a freely propagating flame, in which the point of reference is a fixed position on the flame. In this coordinate system, the burning velocity is defined as the inlet velocity (velocity of unburned gas moving towards the flame) that allows the flame to stay in a fixed location, which is an eigenvalue of the solution method.

To compute an accurate burning velocity, it is important to have the boundaries sufficiently far from the flame itself so that there is negligible diffusion of heat and mass through the boundary. In present simulation, calculations start with an initial run on a very coarse grid that contains only 12 grid points and a computational domain of 3 cm, which was wide enough to encompass the flame. After obtaining an initial solution on this coarse grid, expanded the domain while reducing/tightening the parameters that control the degree to which the solution gradient and curvature were resolved. Repeat this process again until the temperature and species slopes at the boundaries were close to zero and both gradient and curvature controls were at least 0.1 or less. The parameters varied during continuations runs were defined in the Continuations panel of the Chemkin-PRO Interface. The continuation runs started from the solution of the previous run and so rapidly converged to the refined solution.

During current calculations, usually two continuations were used two extended the domain to 33 cm (-3 ~ 30 cm) and set the gradient and curvature solutions no more than 0.1. The gradients of gas temperature and major species were checked to make sure those values were nearly zero at both boundaries.

## 2.5 Summary

In this chapter, the sizes and structures of the tubular flame burners in combustion tests and PIV measurements are introduced in detail. The measurements of pressure fluctuations for oscillatory combustion, measurements of mixing layer thickness by PIV system are also stated. Numerical calculation model concerning burning velocity and reaction time are described.

# Chapter 3 Flame Characeristics of Rapidly Mixed Oxygen Enhanced Tubular Flame Combustion

## 3.1 Introduction

The flame shape, flame diameter, inflammability as well as the stable region of methane/air pre-mixture has been studied using various tubular flame burners [34, 35, 43, 55]. With different sizes of burners the flame characteristics of rapidly mixed tubular flame combustions have also been well examined [33, 61, 70, 71]. The oxidizers for theses researches are air or diluted air. Study concerning oxidizer of higher oxygen mole fractions (above 21%) has not yet been carried out in the rapidly mixed tubular flame combustion.

In this chapter, an inherently safe technique, rapidly mixed oxygen enhanced tubular flame combustion has been systematically investigated to promote energy saving and lower $CO_2$ emissions. Oxygen-enriched air combustion, where oxygen is gradually added into air flow to increase oxygen mole fraction in the oxidizer is firstly discussed. During this process the flame characteristics including flame appearances, inflammability limits and stability are investigated in detail. Oscillatory combustion appeared at high oxygen mole fraction has been measured and discussed by the measurement of pressure fluctuations. The results maybe support the application of the oxygen-enriched air combustion. Furthermore, the flame characteristics of methane/oxygen-air provide a good reference for the oxy-fuel combustion of methane

($CH_4/O_2$-$CO_2$), which has been proposed to promote CCS technique [23, 24].

Then rapidly mixed methane/oxygen tubular flame combustion has been conducted to investigate the flame characteristics. Diffusion flames in the burner of W= 2 mm, tubular flame in the burner of W= 1 mm, and oscillatory combustions in both burners have been analyzed in detail. And the Damkohler number is proposed to hopefully quantify the establishment of rapidly mixed oxygen enhanced tubular flame combustion.

## 3.2 Oxygen-enriched air

Oxygen-enriched air combustion has been widely applied in practice [7, 11]. Here, with the rapidly mixed type tubular flame technique, flame characteristics under various oxygen mole fractions have been examined. To begin with, the flame appearances and inflammability limits of methane/air in both premixed and rapidly mixed type tubular flame combustion will be analyzed, which provide a valuable reference for rapidly mixed oxygen enhanced tubular flame combustion.

### 3.2.1 Methane/Air

#### 3.2.1.1 Flame appearances of PM and RM

At first, the actual effect of “rapidly mixing” of fuel and air in rapidly mixed combustion tests is examined through comparison with the premixed type. To make the rotational velocity almost equal to that of rapidly mixed combustion, for the premixed type the pre-mixture is injected from two parallel slits.

The experiments were conducted with different width slit burners, and hence, influence of different swirl intensity was investigated. Figure 3.1 shows the appearances of flame under representative rich, stoichiometric and lean conditions. Here we use the equivalence ratio ($\Phi$), which is defined as the ratio of the fuel-to-oxidizer ratio to the stoichiometric fuel-to-oxidizer ratio, to represent the rich and lean condition. The equivalence ratio for rapidly mixed combustion is the overall value assuming complete mixing. The left column shows the flame front of the premixed type (denoted as PM) which were taken from the quartz window installed at

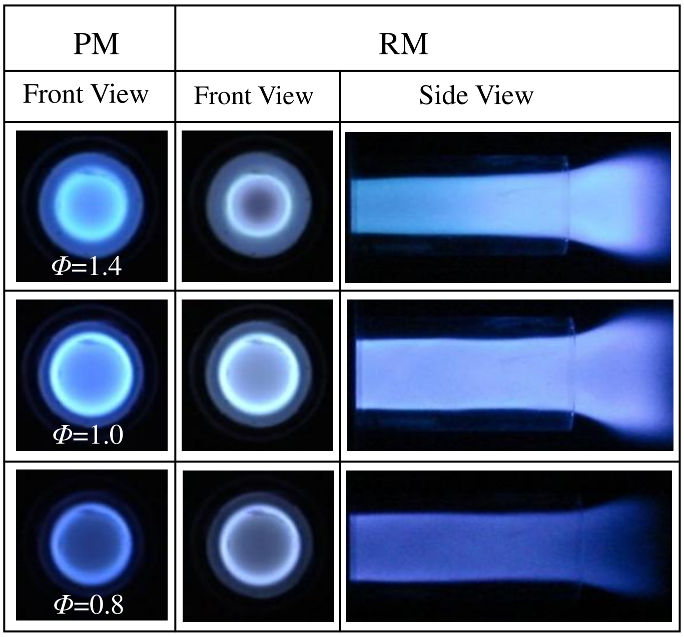

(a) W= 2 mm

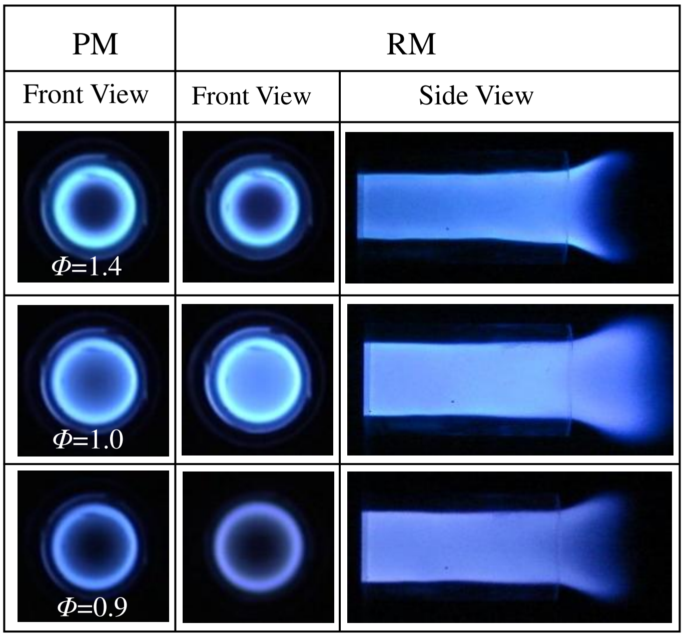

(b) W= 1 mm

Fig. 3.1 Appearances of flame in the rapidly mixed type tubular flame burner (PM: premixed, RM: rapidly mixed, (a) W= 2 mm, (b) W= 1 mm, $Q_{\mathrm{Air}} = 10\ \mathrm{m^3{}_N/h}$ ).

the closed end of the burner. The middle shows the flame front of the rapidly mixed tubular flame, denoted as RM. The right column shows the flame appearances downstream the burner, which were taken from the side view. Two types of burner, W=2 and 1 mm, were used. Accordingly the swirl number was 6.3 and 12.6, respectively. The combustion tube was 50 mm in length. And the air flow rate was fixed at a constant value of 10 $m^3_N$/h.

For the burner W=2 mm, when the fuel was rich in the pre-mixture ($\Phi$=1.4), a uniform flame with strictly tube-like shape is formed, as shown in Fig. 3.1(a). When the fuel flow rate was reduced, hence reducing the equivalence ratio, the flame diameter increased, and the flame diameter reached its maximum value around $\Phi$ =1. With a further decrease of equivalence ratio ($\Phi$ =0.8), the flame diameter reduced. The tubular flame front is always stabilized at a position inside the burner where the burning velocity balances the radial velocity of the mixture [34, 55]. For methane/air pre-mixture its maximum burning velocity is around the stoichiometric [72]. With an/a increase or decrease of $\Phi$, the burning velocity will reduce, consequently the flame front will move inside to balance the radial velocity. Therefore the flame diameter around $\Phi$ =1 is the largest and it reduces when increase $\Phi$ at $\Phi$ >1 and during reducing $\Phi$ at $\Phi$ < 1.

For the rapidly mixed combustion, from the flame fronts and downstream flames (middle and left in (a)) the flames were also very uniform. The flame fronts of the rapidly mixed combustion (RM, middle) seemed somewhat different from those of the premixed, especially for the rich condition of $\Phi$ =1.4. The flame diameter becomes smaller than that of the premixed type. And from the side view, the rich flame with green-color gradually weakened when the flame flowed toward the exit. At the exit, excess fuel was burned with entrained air illustrating a white appearance. While for the lean condition, $\Phi$ =0.8, fuel was insufficient, thus only air entrainment area could be seen at the exit of the combustion tube.

While for the burner W= 1 mm, uniform flame fronts were observed in the premixed combustion (PM, Fig. 3.1(b)) and the flame diameter varied with $\Phi$ just like that of the W= 2 mm. The flame fronts of the rapidly mixed combustion seemed almost the same as those of the premixed. The difference of flame diameters between premixed and rapidly-mixed at $\Phi$= 1.4 also became smaller. This implies that with higher swirl number (12.6), fuel mixes better with oxidizer in the rapidly mixed tubular flame combustion.

To sum up, for current burners of W= 2 and 1 mm, the rapidly mixed air/fuel could reach nearly the same combustion condition as that of premixed type. The swirl numbers (6.3 and 12.6) were larger than 5 which was the requirement for same flame appearance of premixed and rapidly mixed combustion.

#### 3.2.1.2 Inflammability

Next, stable tubular flame regions were measured for both premixed and rapidly mixed type combustion with use of the 2 and 1 mm slit width burners, respectively. In the measurements, two combustion tubes of different lengths, L= 50 and 100 mm, were used. Figure 3.2 shows the results of W=2 mm, in which equivalence ratios ($\Phi$) at extinction were plotted against the air flow rate ($Q_{Air}$).

As is well known, the standard lean and rich flammability limits for methane/air mixtures are 0.5 and 1.68 in equivalence ratio [73], respectively. It is seen in Fig. 3.2

that in the case of premixed combustion with the 100 mm length combustion tube, the equivalence ratios at lean and rich extinction limits are about 0.5 and 1.5, respectively. The lean limit (0.5) is close to the standard lean limit (0.5), while the rich limit (1.50) becomes slightly smaller than the standard rich limit (1.68) due to the so-called Lewis number effect [34, 55]. When the combustion tube is short in length (50 mm), the equivalence ratio at the lean limit increases with an increase in the air flow rate, which seems to be caused by the strong swirl that entrains cold air. While for the rich condition, the entrained gas plays little effects on the rich limit. Since entrained gas is hot burned gas resulting from excess fuel burned in ambient air. The entrained cold air seems ineffective to influence the lean limit when the tube length is increased to 100 mm, since the entrained cold air may not be able to reach the burner root where the flame is stabilized. Even assuming it could be, during such a long distance (100 mm), the cold air would have been heated by surrounding flame. Consequently, the lean limit obtained at L=100 mm does not change with an increase of air flow rate.

In the case of rapidly mixed combustion with the 100 mm combustion tube, the equivalence ratios at the lean limit are slightly less than those of premixed combustion, while the equivalence ratios at the rich limit almost coincide with those of premixed combustion. When the combustion tube is shortened (50 mm), the equivalence ratio at the lean limit increases with an increase in the air flow rate, as observed in the premixed case.

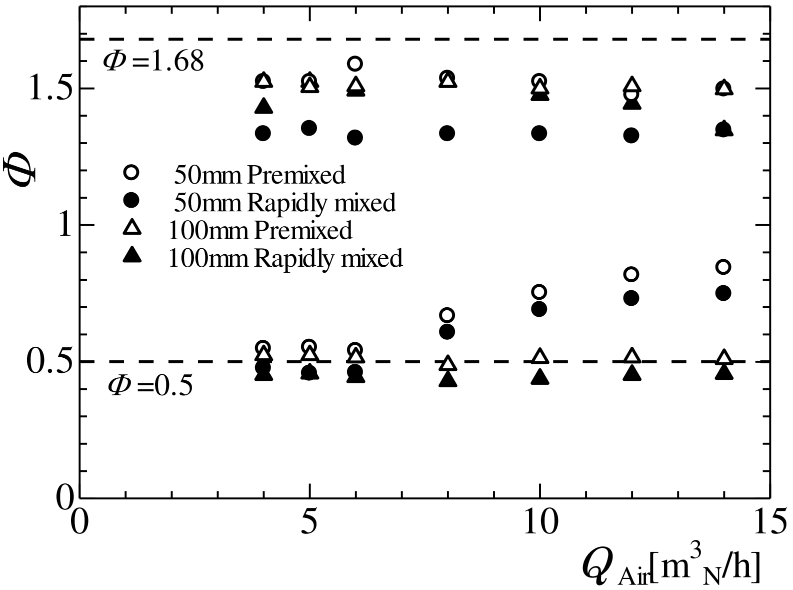

Fig. 3.2 Extinction limits of methane/air flame (W=2mm).

Stable tubular flame regions for the 1 mm slit burner are also mapped for both premixed and rapidly-mixed type combustion, as shown in Fig. 3.3. The upper air flow rate is 11 $m^3_N$/h, which is limited by the burner size (small injection slits). It can be seen that the rich limits for premixed and rapidly-mixed combustion obtained at L=50 and 100 mm are almost the same, around $\Phi$ = 1.5. The lean limits for L=100 mm remain constant ($\Phi$ =0.5), while those for L= 50 mm increase sharply from the initial air flow rate (4 $m^3_N$/h), which is caused by the much high swirl rate ($S_w$= 12.6).

It may be important to note that the rapidly mixed combustion can be achieved for standard flammable mixtures in the present burners, although an entrainment of cold air due to strong swirl sometimes narrows the flammable range.

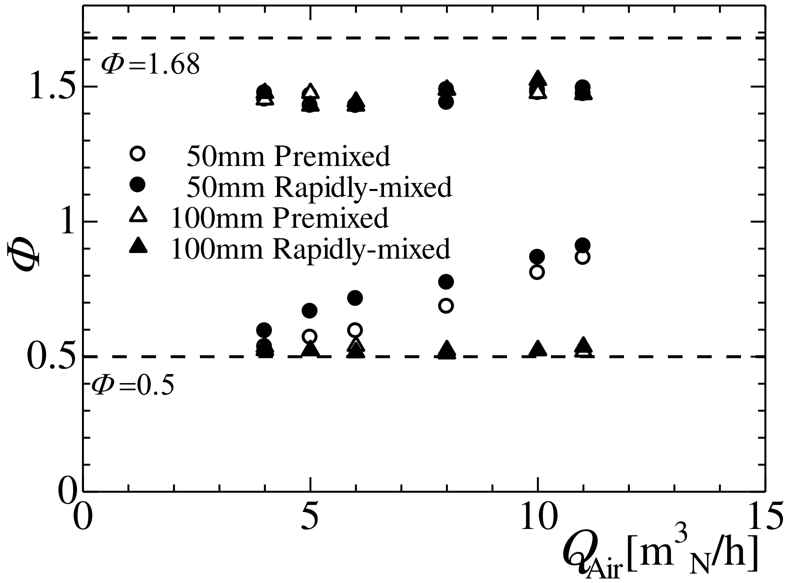

Fig. 3.3　Extinction limits of methane/air flame (W=1mm).

### 3.2.2 Methane/oxygen-air

#### 3.2.2.1 Flame appearances

Next, we have investigated the flame characteristics of oxygen enriched air combustion, using a mixture of air and oxygen as oxidizer. Observations were made using the burner of 2 mm width slit and 50 mm length tube. Oxygen was gradually added into the air. Figure 3.4 shows the variations of flame appearances with the oxygen mole fraction less than 50% in the oxidizer ($\beta < 0.5$). The air flow rate was kept constant (10 $m^3_N$/h) during this procedure, while oxygen flow rates are 0, 2 and 4 $m^3_N$/h, respectively. The methane flow rate was initially set to 1 $m^3_N$/h and then it was gradually reduced. The oxygen mole concentration in the oxygen/air mixture is given as $\beta = (0.21Q_{Air} + Q_{O2})/(Q_{Air} + Q_{O2})$ .

For the case of $\beta = 0.21$ (upper in Fig. 3.4), as has been introduced previously, very uniform flame fronts were observed and with a decrease of methane flow rate (from left to right), hence a decrease of overall equivalence ratio, the flame diameter decreases. An oxygen stream with flow rate of 2 $m^3_N$/h was then added into the air stream ($\beta$ = 0.342, middle), and initially a uniform tubular flame with very thin front was obtained. With decreasing the methane flow rate, the flame diameter and luminosity gradually decrease. When the methane flow rate was further reduced to 0.8 $m^3_N$/h, the flame front became thick and hence the flame luminosity increased. When the oxygen mole fraction was further increased to 0.436 (lower), a uniform flame with thin front was obtained. Owing to low equivalence ratio, flame luminosity seemed weaker comparing with the other two at the same methane flow rate. The flame diameter and the luminosity reduced with a decrease of methane flow rate and finally extinguished.

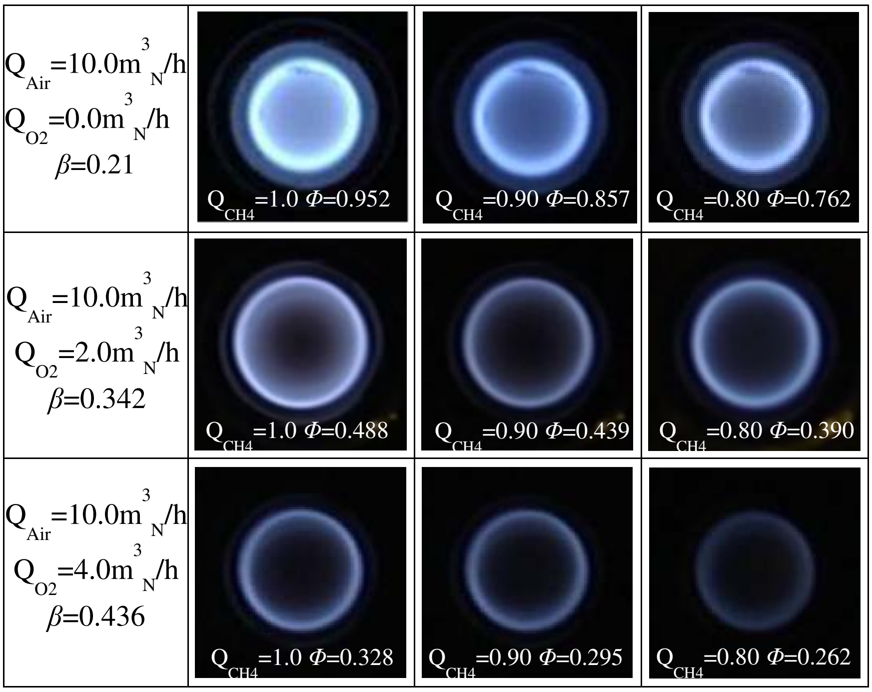

Fig. 3.4 Flame appearances of methane/oxygen-air mixtures for $\beta < 0.5$ in the rapidly mixed combustion (W=2 mm, L=50 mm).

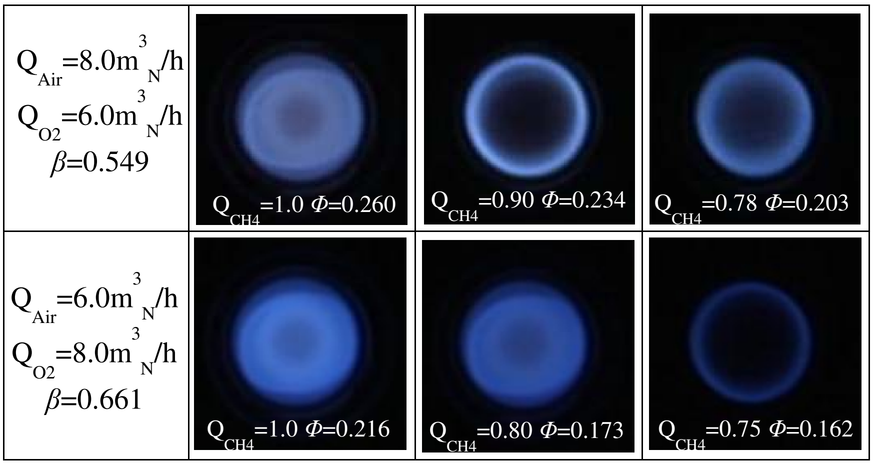

Fig. 3.5 Flame appearances of methane/oxygen-air mixtures for $0.5 < \beta < 0.7$ in the rapidly mixed combustion (W=2 mm, L=50 mm).

With a further increase of the oxygen mole fraction, the flame front became deformed at large methane flow rate, as shown in Fig. 3.5. The oxidizer flow rate was kept constant (14 $m^3_N$/h) and the methane flow rate was gradually reduced from 1 $m^3_N$/h. When the value of $\beta$ was 0.55 (upper), initially the flame was deformed as elliptic rather than circular ($\Phi$= 0.260). Inside the deformed blue flame, a circular flame front appeared. However, with decreasing the methane flow rate to 0.9 $m^3_N$/h ($\Phi$=0.234), the flame became circular-shaped and uniform, and extinguished if further decreased. For $\beta$ = 0.661, even the methane flow rate was reduced to 0.8 $m^3_N$/h ($\Phi$=0.173), deformed and non-uniform flame was observed. And a uniform tubular flame was obtained at the equivalence ratio of $\Phi$=0.162. It should be noted that accompanying these deformed flames, a vibratory combustion occurred which resulted in a strong noise. The pressure fluctuations of the vibratory combustion will be discussed in later section.

With a further increase of $\beta$ to 0.774, as shown in Fig. 3.6 (upper), a luminous zone appeared around the center of the burner, which was accompanied by intense vibratory combustion. Detailed observations show that two diffusion flames, denoted by two arrows, were anchored at the exits of the fuel slits. With a decrease of equivalence ratio, however, a steady, quiet tubular flame was established and was maintained until extinction. While for $\beta$ = 0.868 (middle), the anchored diffusion flames were observed even at low equivalence ratio ($\Phi$=0.125).

For the case of pure oxygen oxidizer ($\beta$=1.0, lower), however, intense turbulent combustion was observed within the present experimental conditions. The anchored diffusion flames which were observed previously ($\beta$=0.77 and 0.868), became much more distinct. It is significant to note that a uniform tubular flame was established just before extinction, and that the equivalence ratio at extinction is 0.09, which is even below the methane/oxygen lean limit of $\Phi$=0.109 obtained by Coward et al [73] using a

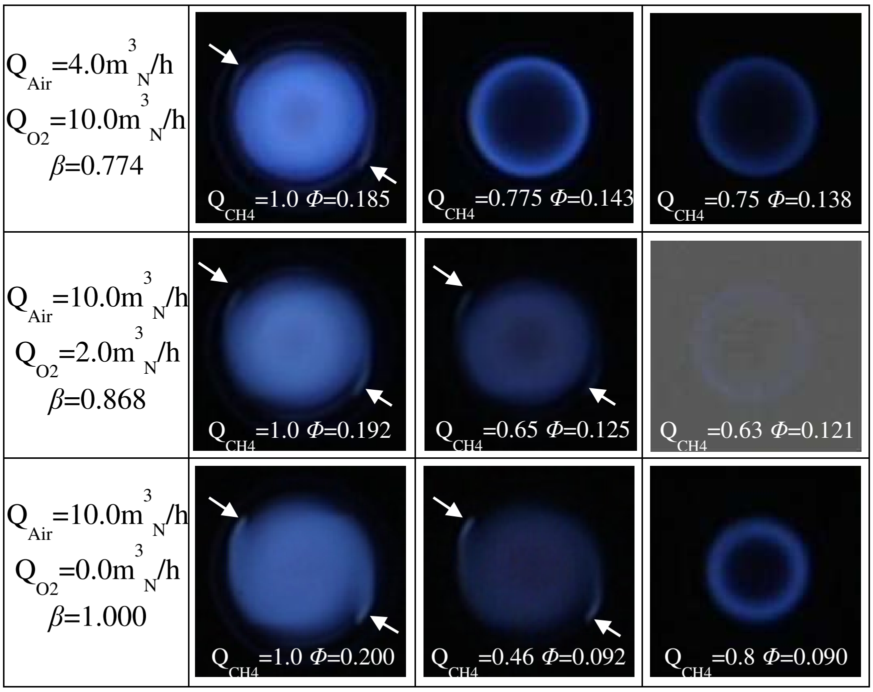

Fig. 3.6 Flame appearances of methane/oxygen-air mixtures for $\beta$ > 0.7 in the rapidly mixed combustion (W=2 mm, L=50 mm).

2 inch diameter tube.

### 3.2.2.2 Inflammability

Figure 3.7 shows the mapping of the uniform tubular flame region in the $\Phi$-$\beta$ plane, which is obtained by decreasing the methane flow rate from 1 m$^3_N$/h while keeping the oxidizer flow rate at a constant of 14 m$^3_N$/h (except for 10 m$^3_N$/h of pure oxygen, which is limited by the apparatus). As seen in Fig.3.7, with an increase of oxygen mole fraction the extinction limit in equivalence ratio decreased. When the oxygen mole fraction is larger than 0.55, oscillatory combustion occurs at higher equivalence ratio and occupies most area in equivalence ratio. While the tubular flame region is quite limited close to the extinction limit; the range in equivalence ratio becomes narrower and narrower with increasing $\beta$.

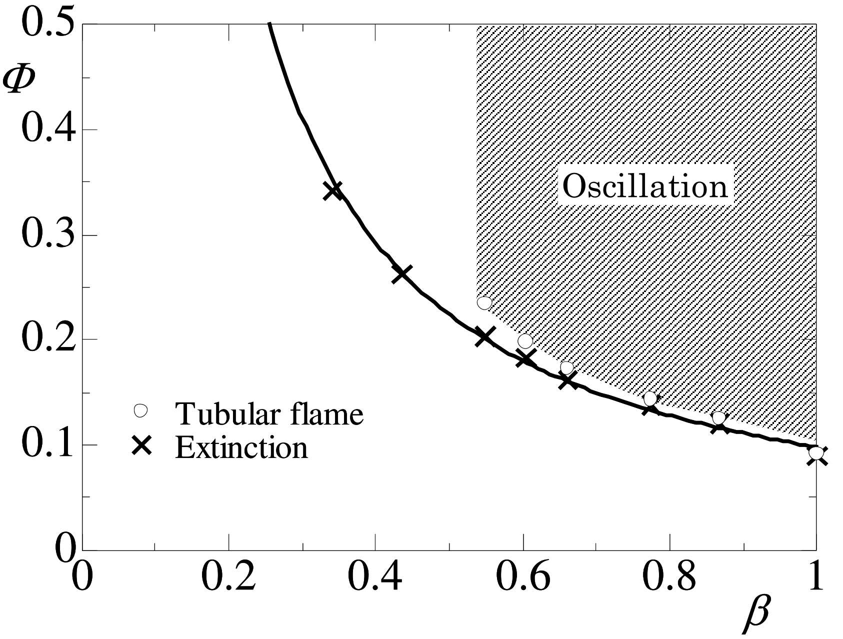

Fig. 3.7 Mapping of various flame regions (W= 2 mm, L= 50 mm).

As previously discussed, the lean limit of methane/air tubular flame combustion is influenced by the entrained air when the combustion tube is short (50 mm). Thus, a 100 mm tube is used to reduce the influence of the entrainment of ambient gases. Using the burners with slit widths of 2 and 1mm, observations were made. Considering the upper flow limit in pure oxygen condition, the flow rate of oxidizer was kept at a constant value of 10 $m^3_N$/h. When reduced the methane flow rate, hence reducing the equivalence ratio, oscillatory combustion, tubular flame, and extinction were observed in turn. Various regions were mapped and the results were shown in Fig. 3.8.

When the oxidizer mole fraction is less than about 0.4, for both burners of W= 2 and 1 mm, stable tubular flame has been obtained in large equivalence ratio range. For $\beta$ above 0.4, oscillatory combustion appears at large equivalence ratio and this oscillatory combustion region enlarges with an increment of $\beta$. With a decrease of equivalence ratio, tubular flame is obtained and maintained until extinction. Though the tubular flame ranges become narrower and narrower with increasing the oxygen mole fraction, the tubular flame range measured in the burner of W= 1 mm is larger than that of W= 2 mm when is $\beta$ larger than 0.44.

The lean limits are almost the same for both burners. With an increment of oxygen mole fraction, the lean limit reduces. For methane/air ( $\beta$= 0.21), the lean limit is 0.475 in equivalence ratio; for methane/oxygen ($\beta$= 1.0) the lean limit reaches 0.10. Comparing with Fig. 3.7, if the 100 mm tube is used, the tubular flame region is enlarged a lot than that of 50 mm tube.

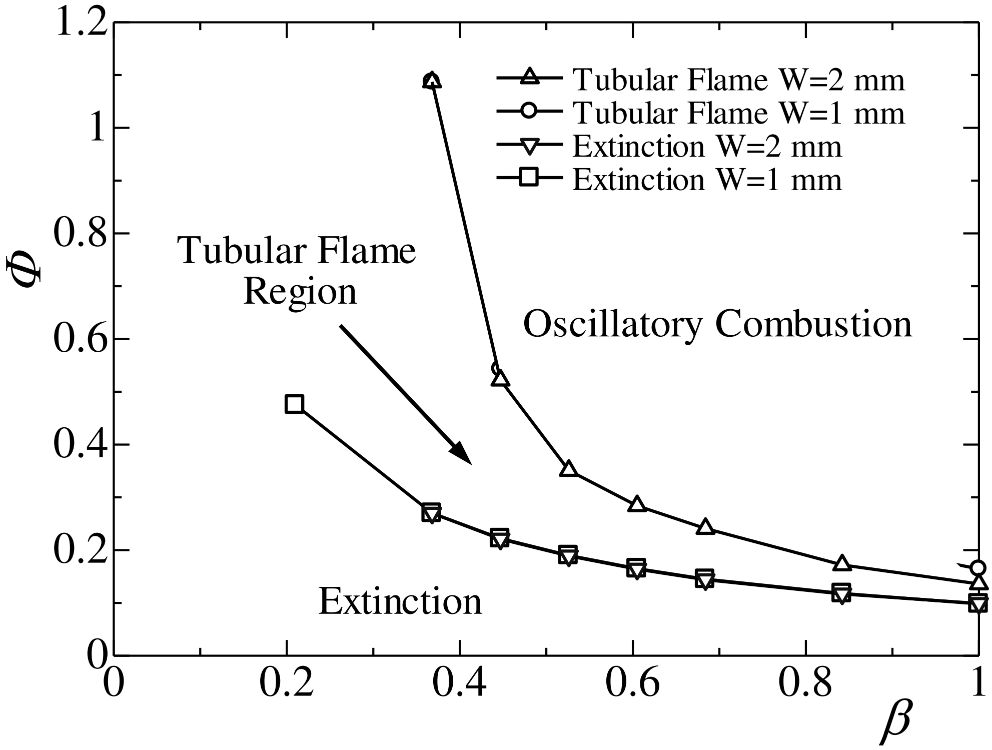

Fig. 3.8 Mappings of various combustion regions in the rapidly mixed type combustion (L= 100 mm).

It is very interesting to note that for methane/oxygen combustion, just before extinction the methane concentration in fresh gas is about 4.75%, which is very close to the extinction limit for methane burned in nitrogen-diluted-air [73]. Since at lean condition, the excess gas, which is mainly nitrogen/oxygen, or oxygen, just plays a role of dilution. The heat specific for nitrogen and oxygen is almost the same thus heat loss is also nearly the same, resulting in the same lean limit in fuel concentration. As shown in Fig. 3.9, when oxygen mole fraction is less than 0.21, Cowards and Johns [73] provided the lean limit with 5.15% methane concentration in the methane/air-nitrogen mixture. While in the study, the extinction limit for methane/oxygen-air mixture where oxygen mole fraction is larger than 0.21, has been measured in both burners using the 100 mm combustion tube. The methane concentration in methane/oxygen-air mixture is almost constant, about 4.75%.

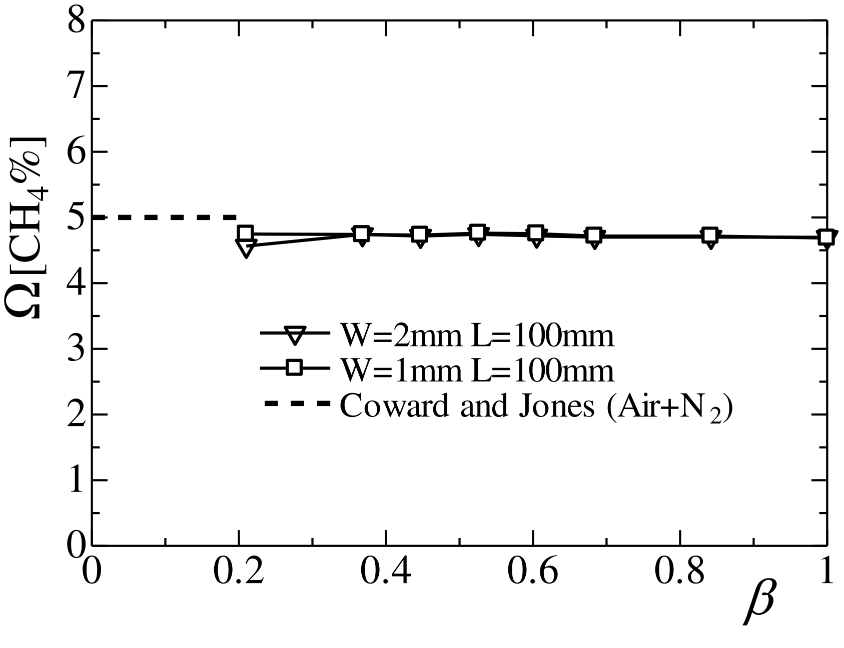

Fig. 3.9 Variations of fuel concentration at lean limit with the oxygen mole fraction $\beta$.

### 3.2.2.3 Oscillation combustion

In oxygen enriched combustion tests, oscillatory combustion frequently occurred when the oxygen mole fraction was large (above 0.4). To obtain detailed information about the oscillation combustion observed in present study, pressure fluctuations were measured by using a pressure sensor and a digital oscilloscope. FFT frequency analysis corresponding to the pressure fluctuations was performed using a computer. In the FFT frequency analysis the reference value of the sound pressure level was $P_0 = 2.0\times10^{-5}$ Pa.

Typical oscillation combustion in combustor mainly includes the Helmholtz type and acoustic resonance type [74-77]. A brief introduction on the oscillation combustion modes is given in the following.

The first type is the Helmholtz resonance. For the tubular flame combustor, the vacant space formed between the burner itself and the combustion tube could be considered as a Helmholtz resonator. The exits of the tangential slits where the fuel and oxidizer are injected are considered as the throat. Thus, the resonance oscillation frequency of Helmholtz type is given by the following equation,

$$f_0 = \frac{C}{2\pi}\sqrt{\frac{A_S}{V_C L_S}} \tag{3.1}$$

$f_0$: frequency of Helmholtz resonance

$C$: sound speed (m/s)

$A_S$: section area of the throat

$V_C$: volume of the Helmholtz resonator

$L_S$: length of the throat

Corresponding to current tubular flame burner size, relevant parameters are calculated as follows: $A_S$ = 6.4×$10^{-5}$ $m^2$, $V_C$ = 1.31×$10^{-5}$ $m^3$, $L_S$ =0.02 m. Sound speed (C) is based on the equilibrium composition calculated from chemical equilibrium [78] and corrected by the measured gas temperature. The temperature in this study has not been measured, and the calculated adiabatic flame temperature is used to calculate the sound speed. For the case of $\beta$ = 0.661, $\Phi$ = 0.216 the adiabatic flame temperature is 1772 K, and $C$ = 792 m/s; for $\beta$ = 0.868, $\Phi$ = 0.192, the adiabatic flame temperature is 1939 K, and $C$ = 817m/s. Thus for the cases of $\beta$ = 0.661 and 0.868 in the burner of W=2 mm and tube length of 50 mm, the oscillation frequency is 1972 and 2034 Hz, respectively.

On the other hand, there exists the oscillation caused by the acoustic resonance, which includes three modes: axial mode, circumferential mode and radial mode. The axial mode has been common recognized in burners under practical use [76,77]. It's nature oscillation frequency for the one side close while one side open model could be determined in a form that,

$$f = \frac{C(2n_z - 1)}{4(l + \Delta l)} \tag{3.2}$$

$f$ : frequency of acoustic resonance

$n_z$ : order of axial mode (=1,2, …)

$l$ : length of the combustor

$\Delta l$ : correction value for open exit

The length of the combustor in current analysis is 65 mm, while the correction value (0.3×burner diameter) is used which is based on the geometry of the open exit [77]. With the burner size and combustion condition, the frequency could be obtained through Eq (3.2).

For the circumferential and radial mode, meanwhile considering the axial mode simultaneously, and assuming zero velocities of all the particles at the burner wall, the oscillation pressure frequency for acoustic resonance could be determined by the following equation [74,76].

$$f = \frac{C}{2\pi}\sqrt{\left(\frac{\alpha_{nm}}{r}\right)^2 + \left(\frac{(2n_z - 1)\pi}{2(l + \Delta l)}\right)^2} \tag{3.2}$$

$f$ : frequency of acoustic resonance

$\alpha_{nm}$: the m-th solution for $dJ/dx = 0$

$J_n$ : Bessel function of order n

$n$ : order of circumferential mode (=0,1,2, …)

$m$ : order of radial mode (=0,1,2, …)

$r$ : burner radius

$n_z$ : order of axial mode (=1,2, …)

The detailed vale of $\alpha_{nm}$ could be found in the literatures of Refs. [79] and [80]. Introducing the detailed parameters in current analysis, the nature frequency of the acoustic resonance could be obtained.

The oscillatory combustion observed at $\beta$ = 0.661, $\Phi$ = 0.216 in the 2 mm slit burner with 50 mm length tube were measured. The pressure fluctuations were shown in Fig.3.10. Within the measured time period, pressure fluctuations were above ±5 kPa and some were even close to ±10 kPa. Fig. 3.11 shows the corresponding FFT results. The sound levels were above 110dB which were close to that of the aircraft engine.

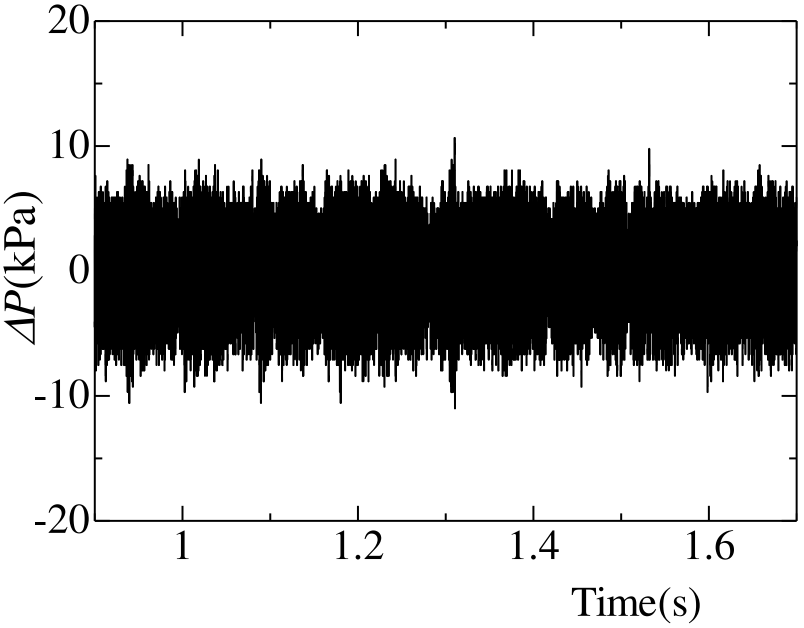

Fig. 3.10 Pressure fluctuations for $\beta = 0.661$ (W=2 mm, L= 50 mm, $Q_{O_2} = 8.0\ \mathrm{m^3_N/h}$ $Q_{Air} = 6.0\ \mathrm{m^3_N/h}$, $Q_{CH_4} = 1.0\ \mathrm{m^3_N/h}$, $\Phi = 0.216$).

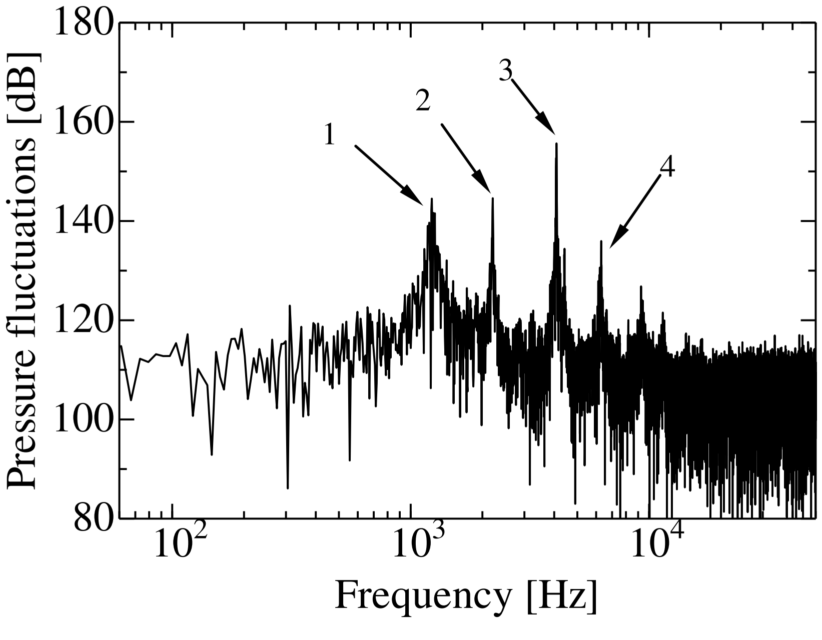

Fig. 3.11 Pressure fluctuations spectra for $\beta = 0.661$ (W= 2 mm, L= 50 mm, $Q_{O_2} = 8.0\ \mathrm{m^3_N/h}$, $Q_{Air} = 6.0\ \mathrm{m^3_N/h}$, $Q_{CH_4} = 1.0\ \mathrm{m^3_N/h}$, $\Phi = 0.216$).

The frequencies for the appearances of peak-sound-level were 1220, 2210, 4090, 6300…Hz, which were listed in Table 3.1. The measured frequencies were different from those of Helmholtz resonance calculated through Eq.(3.1). The frequencies for the axial mode and circumferential/radial mode were calculated through Eqs. (3.2) and (3.3), where the sound speed was given from chemical equilibrium ($C$ = 792 m/s). The results were also listed in Table 3.1. For the circumferential/ radial mode, the frequencies were much larger, above 20000Hz, which were beyond the frequency that human being could hear. Thus current oscillatory combustion may not belong to the circumferential or radial mode.

The frequencies of axial mode with different orders of $n_z$ were also different from experimental measurements. In the experiment due to high flame temperature, the pressure sensor was kept in some distance from the combustion area. It was possible that the sound speed in the vicinity of the pressure sensor was much smaller than the calculated value. Here $C$=340 m/s was assumed to calculate the axial mode. The

Table 3.1 Frequency analysis (left: experimental, middle: axial mode, right: circumferential and radial mode).

| Experimental | |
|---|---|
| Peak | Frequency (Hz) |
| 1st | 1220 |
| 2nd | 2210 |
| 3rd | 4090 |
| 4th | 6300 |

| Axial mode | |
|---|---|
| $n_z$ | Frequency (Hz) |
| 0 | 2918 |
| 1 | 8754 |
| 2 | 14589 |
| 3 | 20425 |

| | | Radial mode | | |
|---|---|---|---|---|
| | $m$ / $n$ | 1 | 2 | 3 |
| Circumferential mode | 0 | 60260 | 110190 | 159970 |
| | 1 | 28820 | 83880 | 134330 |
| | 2 | 47850 | 105470 | 156830 |

calculated frequencies were 1214, 3643, 6071, 8500…Hz, which seemed close to the first, third and fourth measured frequencies. This means that the oscillatory combustion seemed to belong to acoustic resonance of axial mode. The measured result is different from the oscillatory combustion in premixed tubular flame combustion measured by Shimokuri et al. [81], which was circumferential mode. Anyhow, further experiments are expected to measure the pressure fluctuations.

With the same apparatus, oscillatory combustion occurred at $\beta$ = 0.868, $\Phi$ = 0.192 was also measured. Since it was just before the onset of tubular flame combustion, the pressure fluctuations became smaller, which were around ±5 kPa, as shown in Fig. 3.12. Figure 3.13 shows the FFT results. The sound level was also above 110 dB. And the measured frequencies for peak pressure fluctuations also seemed to close to the axial mode.

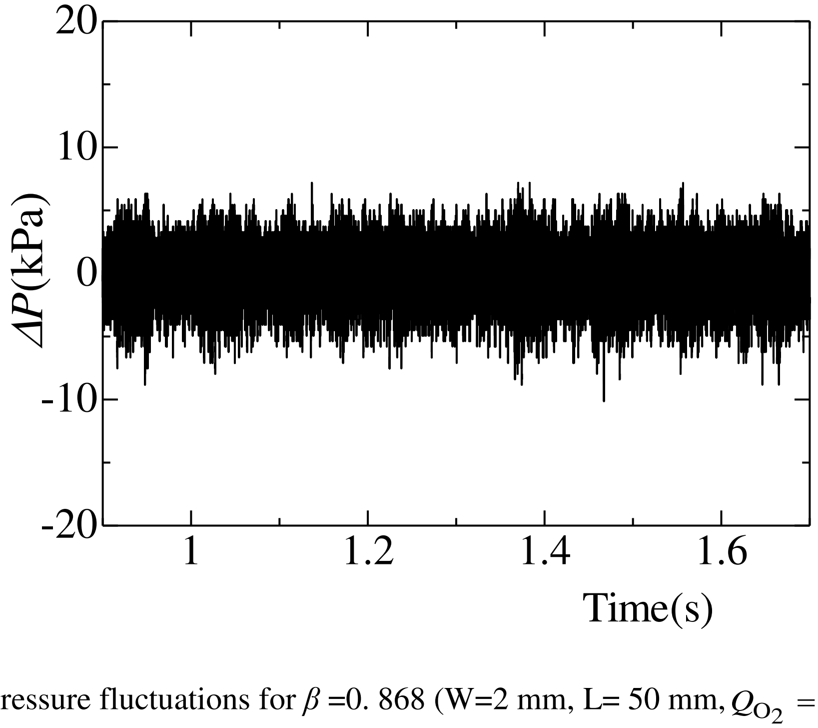

Fig. 3.12 Pressure fluctuations for $\beta$ =0. 868 (W=2 mm, L= 50 mm, $Q_{O_2}$ = 10.0 $m^3_N/h$, $Q_{Air}$ = 2.0 $m^3_N/h$, $Q_{CH_4}$ = 1.0 $m^3_N/h$, $\Phi$ = 0.192).

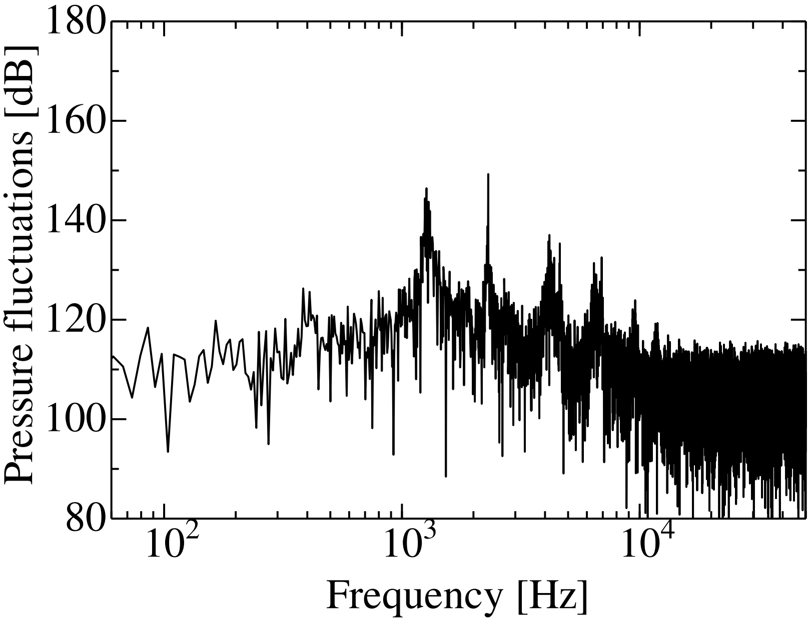

Fig. 3.13 Pressure fluctuations spectra for $\beta$ =0. 868 (W= 2 mm, L= 50 mm, $Q_{O_2} = 10.0$ m$^3$N/h , $Q_{Air} = 2.0$ m$^3$N/h , $Q_{CH_4} = 1.0$ m$^3$N/h , $\Phi = 0.192$ ).

### 3.2.3 Summary

In this section flame characteristics of rapidly mixed methane/oxygen-air tubular flame combustion have been investigated. The following are concrete conclusions:

(1) For methane/air, premixed and rapidly mixed combustion were tested. The flame appearances of rapidly mixed type combustion were almost the same as those of premixed type, however, those in W= 1 mm perform better than W= 2 mm due to higher swirling rate. And it is important to note that the rapidly mixed combustion can be achieved for standard flammable mixtures in the present burners.

(2) When the oxygen mole fraction is less than 40%, rapidly mixed tubular flame combustion of methane/oxygen-air could be achieved within flammable range, which has almost the same flame appearances as that of methane/air.

(3) When the oxygen mole fractions are increased above 50%, the circular tubular flame deformed as elliptical shape accompanied by intense vibration. With a decrease of equivalence ratio, stable circular tubular flame is obtained.

(4) When the oxygen mole fractions are increased to 77%, diffusion flames are anchored at the exits of the fuel slits, resulting in intense oscillatory combustion. Steady tubular flame is obtained under very lean condition.

(5) The tubular flame ranges under various oxygen mole fractions are investigated with constant oxidizer flow rates in both burners of W=2 and 1mm. With an increase of oxygen mole fraction, the tubular flame range in equivalence ratio becomes narrow and limited at the lean side.

(6) The pressure fluctuations of oscillatory combustion at $\beta$ = 0.661 and 0.868 are measured and analyzed. The oscillatory combustion seems belong to the acoustic resonance of axial mode.

## 3.3 Pure oxygen

Pure oxygen combustion is proposed to improve efficiency and accommodate CCS technique. In case of dangers of flash back and detonation, in this study, the safe technique of rapidly mixed type tubular flame combustion has been proposed for pure oxygen combustion. In previous section, the methane flame characteristics of various oxygen mole fractions in oxidizer have been investigated. Diffusion flames were observed at high oxygen mole fractions, which resulted in oscillatory combustion and limited the tubular flame range in a narrow equivalence ratio range closing to the extinction. To make deep a study on pure oxygen combustion in rapidly mixed type tubular flame burner, the combustion tests were carried out in two types of burner. For the burner of W= 2 mm, the equivalence ratio, the methane flow rate and the oxygen flow rate were kept constant to investigate the flame characteristics, respectively. The oscillatory combustion was also analyzed with pressure fluctuation and FFT analysis. For the tests in the burner of W= 1 mm, quartz tube of 50 and 100 mm were used, and tubular flame were obtained at low equivalence ratios. Stable tubular flame ranges were plotted under various oxygen flow rates.

With almost the same experimental conditions (same oxygen flow rate and nearly the same methane flow rates), diffusion flames and tubular flames were obtained for the burners of W= 2 and 1 mm, respectively. When the methane flow rate was large, hence large equivalence ratio, oscillatory combustion occurred. To quantitatively analyze the requirement for rapidly mixed type pure oxygen tubular flame combustion, the Damkohler number is proposed.

### 3.3.1 Flame appearances

In this part, the appearances of pure oxygen flames are examined in detail. Diffusion flame, tubular flame and turbulent flame are well depicted under various conditions.

#### 3.3.1.1 W=2 mm

As mentioned before, for the 2 mm slit width burner, diffusion flames were anchored at the exits of the fuel slits. The existence of diffusion flame interrupts the mixing between methane and oxygen, resulting in a non-premix flame and sometimes oscillatory combustion. To well understand the diffusion flame, the tests are conducted from three aspects.

At first, keep the equivalence ratio constant ($\Phi = 0.20$) while increasing both fuel and oxygen flow rates. Results were shown in Fig. 3.14.

The broken lines show the positions of the tangential slits, while the broken circles show the position of the burner wall. When the flow rate was small (left, $Q_{O_2} = 2\ \mathrm{m^3{}_N/h}$), two clear diffusion flames were anchored at the exits of the fuel slits. Since at low equivalence ratio $(\Phi = 0.2)$, the mean tangential velocity of methane was one tenth that of the oxygen. Owing to the relatively lower inlet velocity of fuel, the diffusion flames were anchored at the exits of the fuel slits. With doubling the flow rate $(Q_{O_2} = 4\ \mathrm{m^3{}_N/h})$, due to increased injection velocity, flame tips were extended downstream the slits, resulting in an appearance of weak luminous zone in the center, which was accompanied by vibration. When the oxygen flow rate was further increased to 5 times $(Q_{O_2} = 10\ \mathrm{m^3{}_N/h})$, the diffusion flames became weaker while the luminous flame zone around the center was expanded and intensified. An intense turbulent combustion was prevailed downstream the slits. Since the diffusion flame is limited by mass diffusion, when increasing the flow rate, hence increasing convection velocity, diffusion velocity became much smaller comparing with the convection velocity. Consequently most of the fuel flew downstream the fuel slits and then burned in the swirling flow. Thus, an increase in the injection velocity can weaken the diffusion flame, however, at large flow rate turbulent combustion appears.

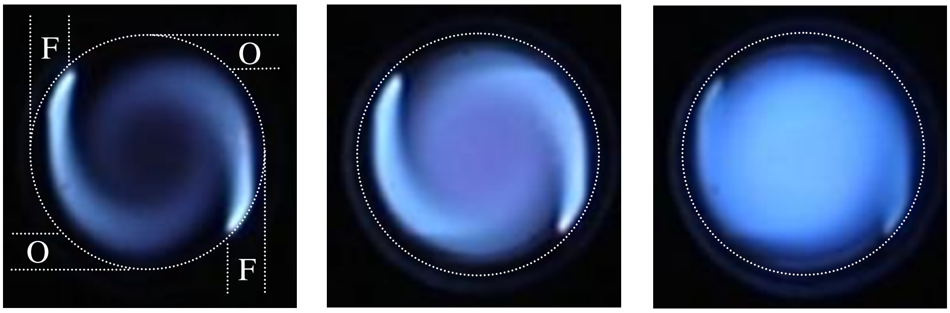

Fig. 3.14 Flame fronts of methane/oxygen in the burner of W= 2 mm and $\Phi = 0.20$ ($Q_{O_2} = 2\,\text{(left)}, 4\,\text{(middle) and}\,10\,\text{(right)}\ \text{m}^3{}_\text{N}/\text{h}$).

Next, oxygen flow rate was fixed at a constant value. In case of strong turbulent flame at large injection velocity, the oxygen flow rate was set as $Q_{O_2} = 2\ \text{m}^3{}_\text{N}/\text{h}$, while the methane flow rate was gradually increased. Results were shown in Fig. 3.15.

When the methane flow rate was small (left, $Q_{CH_4} = 0.2\ \text{m}^3{}_\text{N}/\text{h}$), two clear diffusion flames were anchored at the exits of the fuel slits. With doubling the methane flow rate (middle, $Q_{CH_4} = 0.4\ \text{m}^3{}_\text{N}/\text{h}$), the total equivalence ratio increased and the injection velocity of methane also increased. Thus, while the flame tips extending, excess fuel not consumed by the diffusion flame was burned downstream the slits, resulting in a luminous flame zone in the center, which was accompanied by vibration. When the methane flow rate was further increased to 1 $m^3_N$/h (right), where the total equivalence ratio was 1.0, the intensity of the vibration increased. In detailed observation, the diffusion flame anchored at the fuel exit became weak, however, another two weak diffusion flames were anchored at the exits of the oxygen slits (denoted by the two arrows). Due to very high flame temperature, the quartz tube was heated, and a reddish area appeared around the burner wall.

Fig. 3.15 Appearances of methane/oxygen flames (W= 2 mm, L= 50 mm, $Q_{O_2} = 2.0\,m^3{}_N/h$, $Q_{CH_4} = 0.2\,(\text{left}), 0.4\,(\text{center}), 1.0\,(\text{right})\ m^3{}_N/h$).

Finally, under constant methane flow rate ($Q_{CH_4} = 1\,m^3{}_N$/h) while increasing the oxygen flow rate, flame appearances were discussed, as shown in Fig. 3.16. When the oxygen flow rate was 5 $m^3_N$/h (left), $\Phi = 0.4$, two weak diffusion flames were anchored at the exits of the fuel slits. A luminous flame zone occupied most area inside the burner. When increased the oxygen flow rate to 6 $m^3_N$/h (middle), $\Phi = 0.33$, due to reduced equivalence ratio the luminosity of the center zone became weaker. Two weak diffusion flames still anchored at the exits of fuel slits. When oxygen flow rate was further increased (right), the luminous zone as well as the diffusion flames became weaker due to reduced equivalence ratio, meanwhile the luminous zone shrank owing to increased oxygen injection velocity. For these three cases, strong vibration was observed during the tests.

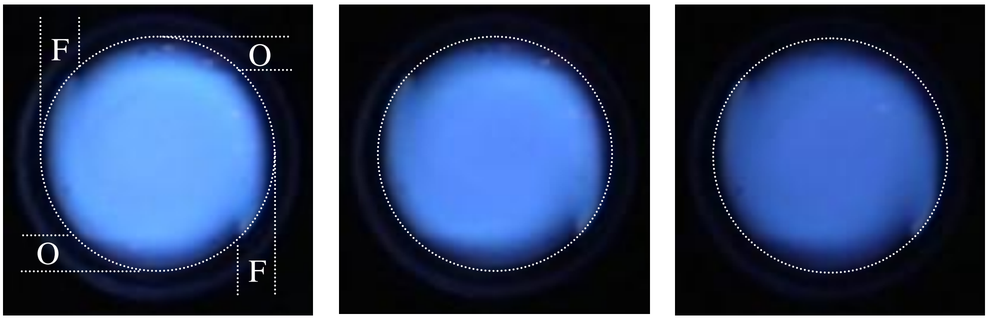

Fig. 3.16 Appearances of methane/oxygen flames (W= 2 mm, L= 50 mm, $Q_{\mathrm{CH_4}} = 1.0\,\mathrm{m^3{}_N}/h$, $Q_{\mathrm{O_2}} = 5.0\,(\mathrm{left}), 6.0\,(\mathrm{center}), 8.0\,(\mathrm{right})\,\mathrm{m^3{}_N/h}$).

Above all, diffusion flames played a dominant role in the burner of W=2 mm. The diffusion flames may be weakened through an increase in injection velocity, however, it is not enough to achieve tubular flame combustion by simply increasing the injection velocity.

### 3.3.1.2 W=1 mm

However, with the 1 mm slit width burner and under lean conditions, tubular flame was successfully achieved. Figure 3.17 shows the flame front under different methane flow rates but the same oxygen flow rate ( $Q_{\mathrm{O_2}} = 8\,\mathrm{m^3{}_N/h}$ ). The length of the quartz tube was 50 mm. When the methane flow rate was large (left,

Fig. 3.17 Appearances of methane/oxygen flames (W= 1 mm, L= 50 mm, $Q_{O_2} = 8.0\,\mathrm{m^3}_\mathrm{N}/h$, $Q_{CH_4} = 1.0\,\text{(left)}, 0.65\,\text{(center)}, 0.45\,\text{(right)}\ \mathrm{m^3}_\mathrm{N}/\mathrm{h}$).

$Q_{CH_4} = 1\ \mathrm{m^3}_\mathrm{N}/\mathrm{h}$), comparing with the same case as the right figure in Fig. 3.16 shown, the diffusion flames disappeared. Instead, close to the burner wall a blue flame ring appeared while a luminous zone occupied the center area. With a decrease of methane flow rate to 0.65$\mathrm{m^3}_\mathrm{N}$/h (middle), a steady tubular flame with uniform front was obtained. The flame front was almost the same as the methane/air flame. Further decreasing the methane flow rate to 0.45 $\mathrm{m^3}_\mathrm{N}$/h (right), the luminosity as well as the flame diameter of the tubular flame reduced due to the decrease of equivalence ratio. The tubular flame was maintained until extinction if further decreasing the methane flow rate.

Figure 3.18 shows the front (left) and side (right) views of the flames. Oxygen flow rate was $10\,\mathrm{m^3}_\mathrm{N}/\mathrm{h}$. When the fuel flow rate was large $(0.9\,\mathrm{m^3}_\mathrm{N}/\mathrm{h})$, turbulent flame with intense vibration was observed (upper). It is seen in the front view that an intense luminous zone occupied the whole burner. Due to incomplete combustion around the slits, combustion continued downstream the tube. However, with reducing the fuel flow rate to $0.85\,\mathrm{m^3}_\mathrm{N}/\mathrm{h}$, a steady tubular flame was suddenly established, although the flame front was slightly wrinkled as shown by the side view. With a further decrease of fuel flow rate, the tubular flame was maintained until extinction.

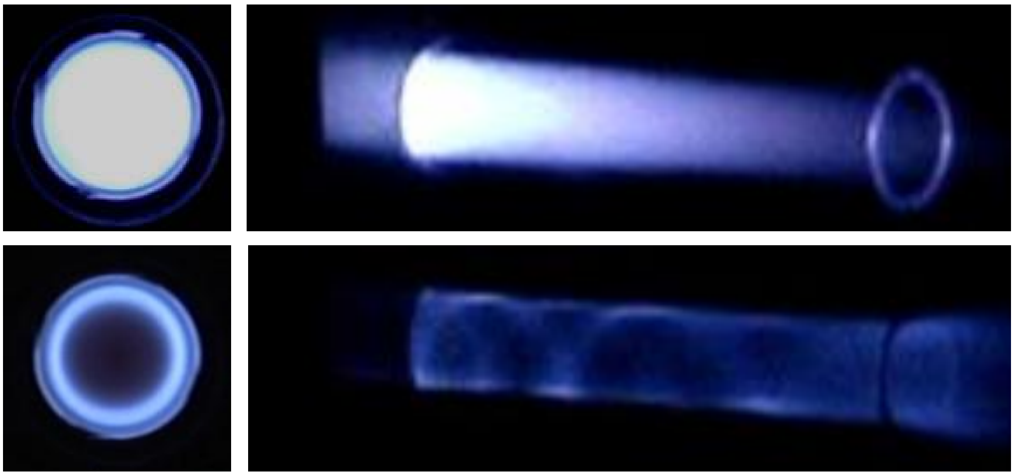

Fig. 3.18 Appearances of methane/oxygen flames with burner of W=1 mm, L=100 mm ($Q_{O_2} = 10.0\,\mathrm{m^3/h}$, upper: $Q_{CH_4} = 0.90\,\mathrm{m^3/h}$, lower: $Q_{CH_4} = 0.85\,\mathrm{m^3/h}$).

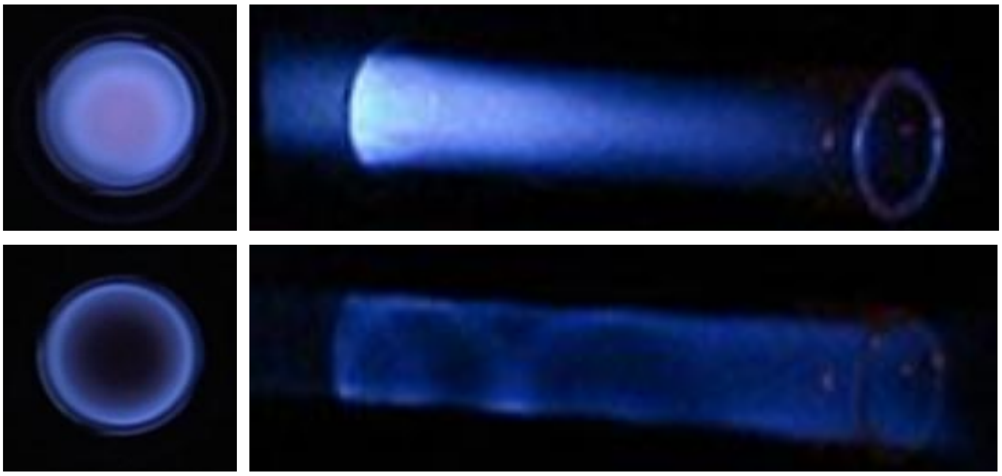

Fig. 3.19 Appearances of methane/oxygen flames with burner of W=1 mm, L=100 mm ($Q_{O_2} = 6.0\,\mathrm{m^3{}_N/h}$ ,upper: $Q_{CH_4} = 0.55\,\mathrm{m^3{}_{\mathit{N}}/h}$ , lower: $Q_{CH_4} = 0.5\,\mathrm{m^3{}_N/h}$ ).

With oxygen flow rate of $6\,\mathrm{m^3{}_N/h}$, Fig. 3.19 shows the front (left) and side (right) views of the flames. The same phenomenon as that of Fig. 3.18 was obtained.

### 3.3.2 Inflammability (W=1mm)

In the 1 mm slit width burner, tubular flame was obtained at lean condition. At large equivalence ratio oscillatory combustion occurred. With the 50 and 100 mm length tube, the stable tubular flame range was measured under various oxygen flow rate. As shown in Fig. 3.20, various flame ranges including oscillatory combustion, tubular flame and extinction are plot against the oxygen flow rate. The oxygen flow rate was increased from 4 to 10 $m^3_N/h$. The results obtained from the 50 and 100 mm length tubes are almost the same. When the equivalence ratio is larger than about 0.18, oscillatory combustion occurs. When reduce the equivalence ratio, from 0.11 to 0.18 stable tubular flame could be obtained. And the extinction occurs around the equivalence ratio of 0.11.

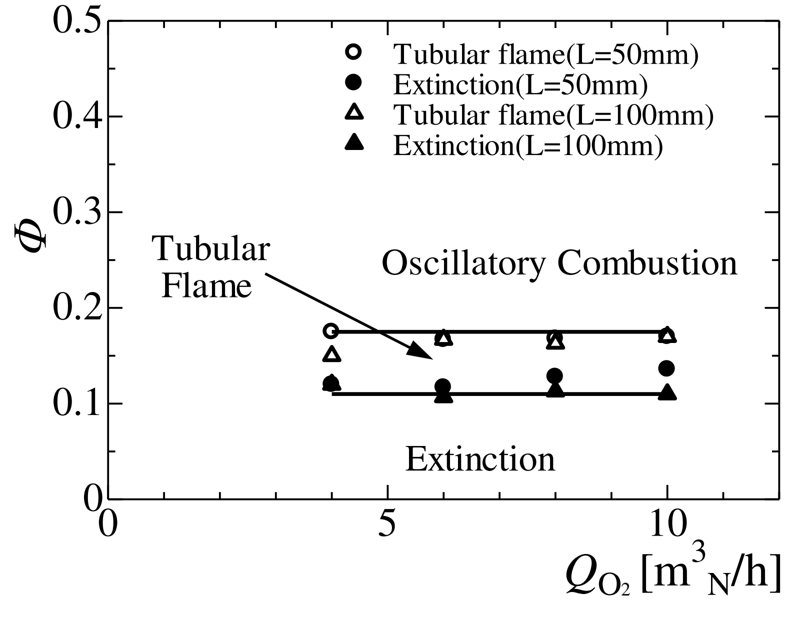

Fig. 3.20 Methane/oxygen tubular flame regions (W=1 mm, L=50, 100 mm).

### 3.3.3 Oscillatory combustion

In combustion tests, though pure oxygen tubular flame has been obtained, oscillatory combustion frequently occurred for both W= 2 and 1 mm burners. To give detailed information, the pressure fluctuation as well as the FFT frequency analysis of different conditions, including oscillatory combustion in W= 2 mm with L= 50 mm, tubular flame in W=1 mm with L= 50 mm, and oscillatory combustion in W= 1 mm with L= 100 mm were measured and compared, respectively. The reference value of sound pressure level was also $P_0=2.0\times10^{-5}$ Pa.

As previously has been introduced, the oscillatory combustion occurred at high oxygen mole fractions seems belong to the axil mode acoustic oscillation. Here to obtain detailed data concerning pure oxygen combustion, the pressure fluctuations and corresponding spectra were investigated, as Figs. 3.21 ~ 3.26 shown.

Using the 2 mm slit width burner with 50 mm length tube, with oxygen flow rate of 4 $m^3{}_N$/h and methane flow rate of 0.3 $m^3{}_N$/h, diffusion flame accompanied by intense oscillation was observed (as shown in Fig. 3.27). The measured pressure fluctuations were shown in Fig. 3.21. Within the measured time period, pressure fluctuations were above ± 5kPa. And high pressure fluctuations above ± 10kPa even close to ± 20kPa were frequently measured. Figure 3.22 shows the corresponding FFT results. The sound levels were above 120dB which were much closed to the aircraft engine. The peak values were even above 140dB which occurred at the frequencies of 1420, 2390, 4490, 7320，…Hz.

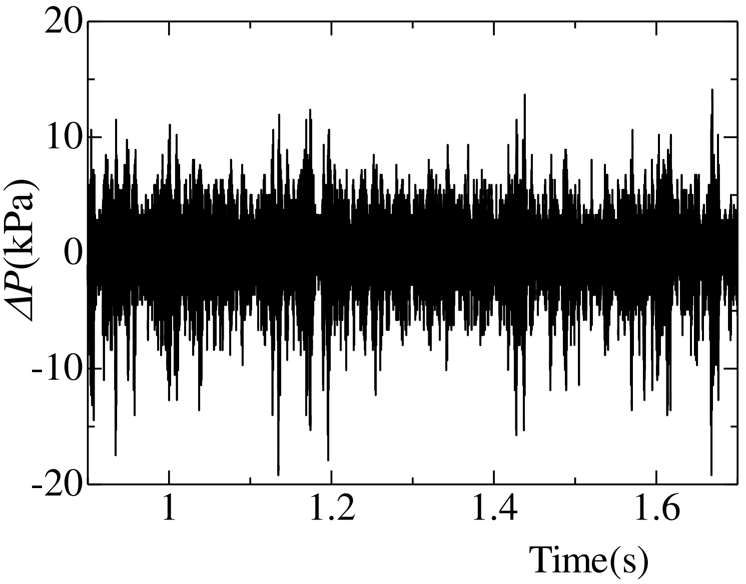

Fig. 3.21 Pressure fluctuations (W= 2 mm, L= 50 mm, $Q_{O_2} = 4.0$ m$^3$$_N$/h, $Q_{CH_4} = 0.3$ m$^3$$_N$/h, $\Phi = 0.15$).

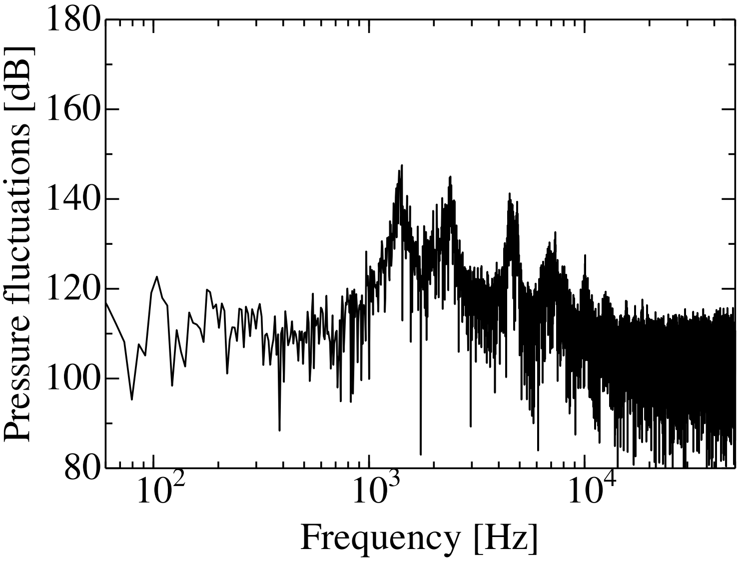

Fig. 3.22 Pressure fluctuations spectra (W=2 mm, L= 50 mm, $Q_{O_2} = 4.0$ m$^3$$_N$/h, $Q_{CH_4} = 0.3$ m$^3$$_N$/h, $\Phi = 0.15$).

With the same flow rates and tube length, tubular flame was obtained with the 1 mm slit width burner, and the pressure fluctuations were measured as shown in Fig. 3.23. Comparing with the case in W=2 mm, the pressure fluctuations were much smaller, most of which were less than ±3 kPa. Figure 3.24 shows the FFT results. The pressure fluctuation spectra was also lower than that shown in Fig. 3.22.

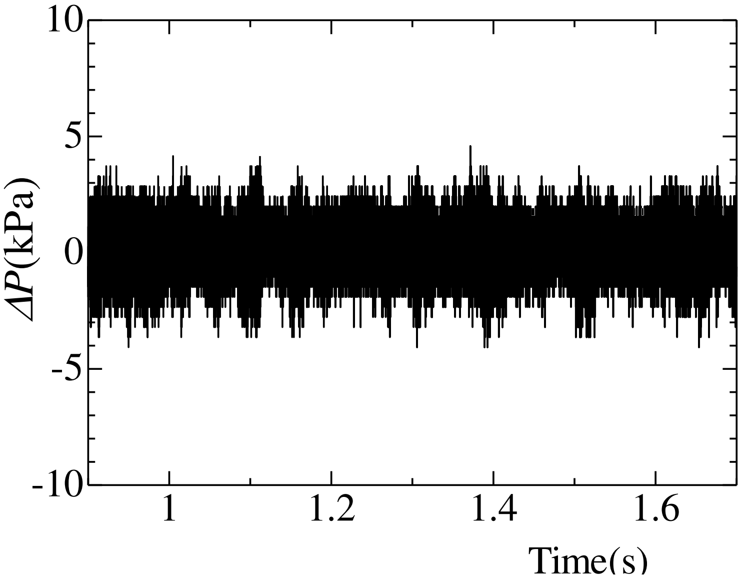

Fig. 3.23 Pressure fluctuations (W=1 mm, L=50mm, $Q_{O_2} = 4.0$ m$^3$N/h, $Q_{CH_4} = 0.3$ m$^3$N/h, $\Phi = 0.15$).

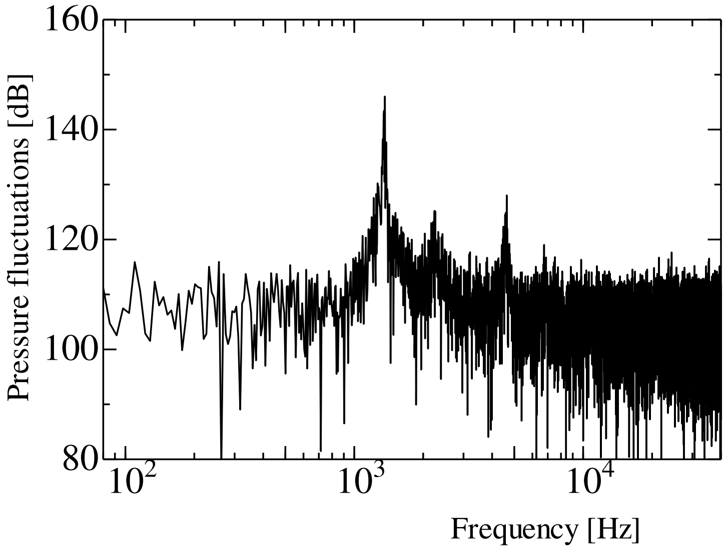

Fig. 3.24 Pressure fluctuations spectra(W=1 mm, L=50mm, $Q_{O_2} = 4.0\ \mathrm{m^3{}_N/h}$, $Q_{CH_4} = 0.3\ \mathrm{m^3{}_N/h}$, $\Phi = 0.15$).

Under the same condition except for the 100 mm tube, tubular flame with almost the same pressure fluctuations was measured. However, at large equivalence ratios, oscillatory combustion occurred. With oxygen flow rate of 4 $\mathrm{m^3{}_N/h}$ and methane flow rate of 0.4 $\mathrm{m^3{}_N/h}$, the pressure fluctuations and FFT analysis were carried out. Comparing with the case of methane flow rate 0.3 $\mathrm{m^3{}_N/h}$ in the burner of W=2 mm, the pressure fluctuations increased much, which were above ±20 kPa, as shown in Fig. 3.25. Figure 3.26 shows the FFT results. The sound level even reached 170 dB. The intensity of the oscillation may be caused by the increase of equivalence ratio.

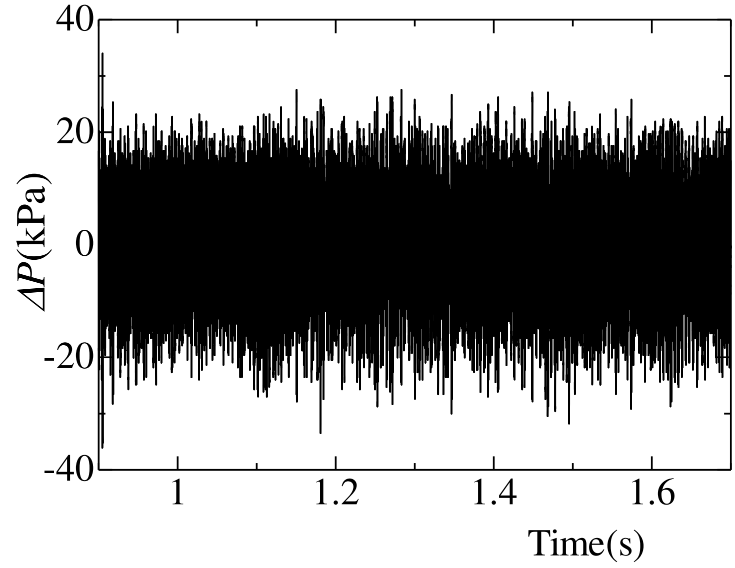

Fig. 3.25 Pressure fluctuations (W=1 mm, L= 100 mm, $Q_{O_2} = 4.0$ m$^3$N/h , $Q_{CH_4} = 0.4$ m$^3$N/h , $\Phi = 0.20$).

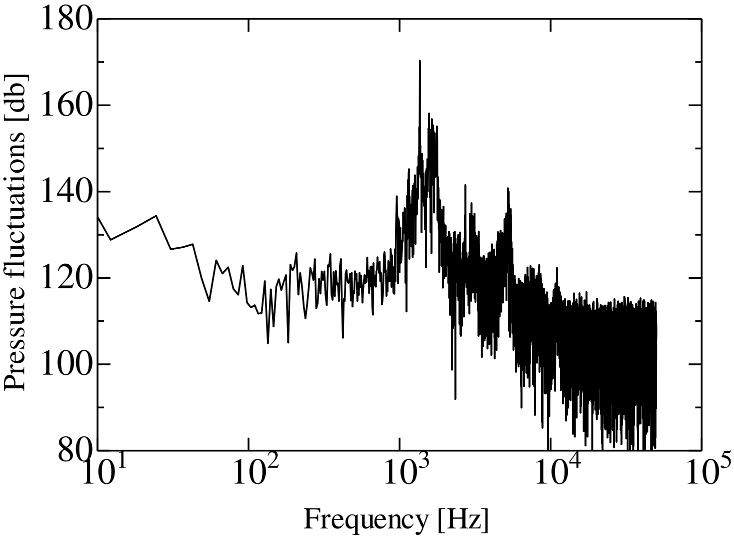

Fig. 3.26 Pressure fluctuations spectra (W= 1 mm, L= 100 mm, $Q_{O_2} = 4.0$ m$^3$N/h , $Q_{CH_4} = 0.4$ m$^3$N/h , $\Phi = 0.20$).

### 3.3.4 Analysis concerning tubular flame combustion establishment

For pure oxygen combustion, various flames including turbulent flame, diffusion flame and tubular flame were obtained. In present experiments, turbulent flames and diffusion flames were accompanied by intense oscillation, which restricted the practical applications. From the viewpoints of both practical application and fundamental research, it is very important to analyze the requirement for establishment of oxygen enhanced tubular flame combustion. To quantitatively investigate the requirement, some combustion tests are examined and analyzed in detail.

At the same oxygen flow rate $(4\ \mathrm{m^3_N/h})$, detailed observations were made with varying equivalence ratio for both burners, which were shown in Fig. 3.27. In the case of W=2 mm (column a), diffusion flames were anchored for all the cases. When the methane flow rate was low, hence, the overall equivalence ratio was small $(\Phi = 0.10)$, diffusion flames consumed most of the fuel injected. As the methane flow rate was increased such as to $\Phi = 0.15$, the diffusion flames became more bigger. As the methane flow rate was further increased to $\Phi = 0.20$, the diffusion flame tips were extended and the flame luminosity around the center increased. This suggested that unconsumed methane in the diffusion flame zone flew downstream and reacted with the oxygen in a turbulent mode. When the methane flow rate was further increased to $\Phi = 0.50$, a highly intensified luminous zone occupied the inside of the burner, while two diffusion flame bridges of weak luminosity can be still seen around the fuel slits. A very strong, vibratory combustion occurred.

In the case of W=1 mm, however, tubular flame combustion could be achieved when the methane flow rate was small. As seen in column (b), uniform tubular flames

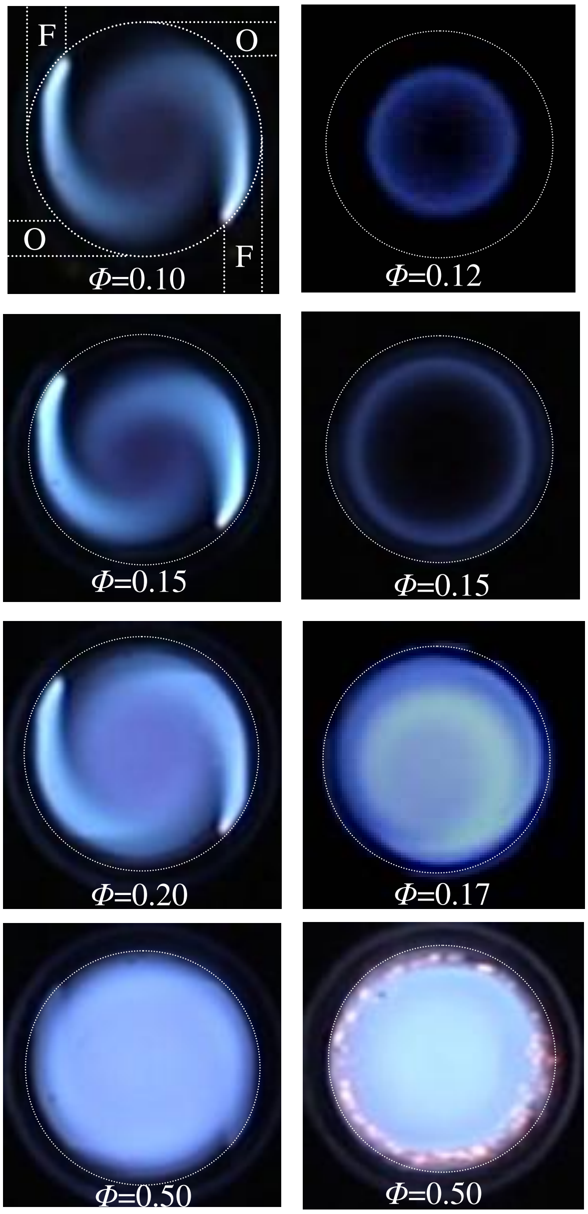

(a) (b)

Fig. 3.27 Appearances of methane/oxygen flames ($Q_{O_2} = 4\,\mathrm{m^3{}_N/h}$, column a: W=2 mm; column b: W= 1 mm).

were established at the methane flow rate of $0.24$ and $0.30\ \mathrm{m^3/h}$ $(\Phi = 0.12$ and $0.15)$. As the burning velocity increased with increasing equivalence ratio, the flame diameter increased. With a further increase in the methane flow rate, where $\Phi$ reached 0.17, the tubular flame still existed but was disturbed and deformed. Instead, a turbulent combustion occurred downstream, resulting in an appearance of a luminous zone around the center of the burner. With further increasing the methane flow rate $(\Phi = 0.50)$, the turbulent combustion was greatly strengthened, leading to an expanded and intensified luminous zone with strong vibration.

In current tubular flame burner, when fuel is injected from the fuel slit, starting from the fuel slit the fuel will meet and mix with upstream oxidizer flow. Once ignited, a flame could be established. In the burner of W=2 mm, after injected into the burner, methane started to mix with oxygen, however, before complete mixing of methane and oxygen, a diffusion flame was established and anchored at the exits of fuel slits (see column (a) in Fig. 3.27). The existence of diffusion flame interrupted the mixing process of methane and oxygen, resulting in the incomplete mixing, hence a failure of establishment of tubular flame.

In contrast, in the burner of W=1 mm, when the equivalence ratio is small ($\Phi$=0.12 and 0.15), before reaction starts methane has mixed with oxygen and tubular flame could achieve. With an increase of equivalence ratio, the reaction rate increases. At the same time, due to the increase of methane flow rate, the mixing of methane and oxygen also increases. Both the mixing and reaction rate increase, however, instead of stable tubular flame oscillatory combustion has been observed ($\Phi$ = 0.17 and 0.5). This becomes a great barrier to safe tubular flame combustion, in which the mixing should be completed before the onset of reaction. Thus, it is indispensable to carefully investigate the competition between the mixing and reaction. Here the Damkohler number, which is defined as the ratio of mixing time to reaction time, is used to express the competition. In the following two chapters, numerical calculations and measurements were carried out to obtain the reaction time and mixing time, individually.

### 3.3.5 Summary

In this section pure oxygen combustion in burners of W=2 and 1 mm are investigated. For the burner of W=2 mm, the equivalence ratio, the methane flow rate and the oxygen flow rate were kept constant to investigate the flame characteristics, respectively. The oscillatory combustion has also been analyzed with pressure fluctuation and FFT analysis. For the tests in the burner of W=1 mm, quartz tube of 50 and 100 mm were used, and tubular flame were obtained at low equivalence ratios.

(1) In the burner of W= 2 mm, diffusion flames were anchored at the exits of fuel slits. For the same equivalence ratio, increasing the flow rate, hence increasing injection velocity, the diffusion flame was extended and became weaker, however, oscillatory combustion intensifies at high injection velocity.

(2) Keeping the oxygen flow rate constant, with increasing the methane flow rate, the diffusion flame became weak and the intensity of oscillatory combustion increased due to an increase of equivalence ratio.

(3) Keeping the methane flow rate constant while increasing the oxygen flow rate, the diffusion flame became weak and the luminosity decreased due to decrease of equivalence ratio;

(4) For W= 1 mm, when equivalence ratio was large, turbulent combustion dominated

the combustion; with a decrease of equivalence ratio, stable tubular flame combustion was obtained and remained until extinction. Under various oxygen flow rates with both 50 and 100 combustion tubes, the tubular flame ranges were examined, which was about 0.11 ~ 0.18 in equivalence ratio;

(5) The oscillatory combustions in W= 2 and 1 mm burners were tested, in which the pressure fluctuations were over ± 10 kPa and ± 20 kPa, respectively. For the case of tubular flame combustion in W=1 mm and L=50 mm, the pressure fluctuations was about ± 3 kPa;

(6) Damkohler number, which was the ratio of mixing time to reaction time, has been proposed to quantify the establishment of tubular flame combustion.

## 3.4 Summary

In this chapter the rapidly mixed oxygen enhanced tubular flame combustion has been investigated in two types of burners, W= 2 and 1mm. The flame characteristics for oxygen-enriched air and pure oxygen combustion are summarized as follows:

(1) When the oxygen mole fraction is less than 40%, rapidly mixed tubular flame combustion of methane/oxygen-air could be achieved within flammable range, which has almost the same flame appearances as that of methane/air.

(2) When the oxygen mole fractions are increased to high value, say, 77%，diffusion flames are anchored at the exits of the fuel slits, which inhibit the mixing of fuel and oxidizer, resulting in intense oscillatory combustion. With a decrease of equivalence ratio, stable tubular flame is obtained, whose range is limited at the vicinity of lean limit.

(3) With an increase of oxygen mole fraction, stable tubular flame range in equivalence ratio becomes narrower while the oscillatory combustion range enlarges; the upper limit of stable tubular flame in W = 1 mm is larger than that of W = 2 mm, while the lean limit is almost the same.

(4) As for pure oxygen combustion, in the burner of W=2 mm, diffusion flames are anchored at the exits of fuel slits interrupting the mixing of fuel and oxygen. By increasing the flow rate, hence increasing injection velocity, the diffusion flame cannot be totally inhibited and intense oscillatory combustion occurs.

(5) For W=1 mm, when equivalence ratio is large, turbulent combustion dominates the combustion; with a decrease of equivalence ratio, stable tubular flame combustion is obtained and remained until extinction. Under various oxygen flow rates, stable tubular flame ranges are examined, which is about 0.11 ~ 0.18 in equivalence ratio.

(6) The oscillatory combustions for oxygen-enriched air ($\beta = 0.661$ and 0.868) and pure oxygen are tested, respectively. The pressure fluctuations are almost over ± 10 kPa. And the oscillatory combustion seems belong to the acoustic resonance of axial mode.

(7) Damkohler number, defined as the ratio of mixing time to reaction time, is expected to quantify the establishment of tubular flame combustion.

# Chapter 4 Numerical Calculation of Burning Velocities and Reaction Time

## 4.1 Introduction

The laminar burning velocity ($S_u$) is an important overall characteristic of the reactivity of combustible mixture. In tubular flame burner, usually a uniform tubular flame is established at a position where the inward radial velocity of the unburned gas equals the burning velocity [34, 55]. When fuel is burned under different oxidizer and equivalence ratio, the burning velocity varies great, say, the burning velocities of both stoichiometric methane [82] and propane [83] in oxygen are nearly ten times as large as that in air. For deep investigation of the flame stabilization under various oxygen mole fractions, it is necessary to obtain reliable data of the burning velocity.

As has been discussed in previous chapter, for the rapidly mixed tubular flame combustion, the mixing should be completed before the onset of reaction. Therefore it is important to analyze the chemical reaction rate, i.e., reaction time $(\tau_\mathrm{r})$ for the combustible mixture. In this study the reaction time was calculated by the relation,

$$\tau_\mathrm{r} = \frac{\delta_\mathrm{L}}{S_u}, \tag{4.1}$$

in which $\delta_\mathrm{L}$ is laminar flame thickness and $S_u$ is laminar burning velocity.

The numerical calculation was performed through the Chemkin-PRO software.

The calculation model and the boundary conditions concerning the laminar burning velocity ($S_u$) calculation have been introduced in Chap. 2. While the laminar flame thickness ($\delta_{\mathrm{L}}$) is calculated from temperature profile, which has been simultaneously obtained with $S_u$ calculation.

For further discussion, the laminar burning velocities of methane/oxygen-air mixtures are numerically calculated as a function of the equivalence ratio ($\Phi$) using the oxygen concentration ($\beta$) in the oxidizer as a parameter. Based on valid data analysis of burning velocity, the reaction time is further calculated. To promote the wide application of oxygen enhanced combustion, the laminar burning velocities of $CH_4/O_2$-$CO_2$, $H_2/O_2$, and $C_3H_8/O_2$ are also summarized, respectively.

## 4.2 Laminar burning velocities

As an example, the laminar burning velocity of stoichiometric methane/air is firstly discussed. Then the burning velocities of methane/oxygen-air under various oxygen mole fractions and equivalence ratios are calculated and compared with experimental data. The flame temperatures are obtained along with burning velocities. Furthermore, the laminar burning velocities and adiabatic flame temperatures of $CH_4/O_2$-$CO_2$, $H_2/O_2$ and $C_3H_8/O_2$ are also summarized, respectively.

### 4.2.1 Burning velocities of $CH_4/O_2$-Air

In the computations the total length of the calculation domain, starting 3 cm upstream of the reaction zone, was chosen equal to 33 cm, as shown in Fig. 4.1. The calculations started with a computational domain of 3cm (from 0 to 3 cm) and both the solution gradient and curvature value of 0.5. With two Continuation runs, the domain was expand to 33 cm and reduced the solution gradient and curvature to 0.08. Further increases in mesh resolution and domain-size resulted in less than 0.01 cm/s difference in the calculated burning velocities. And automatic estimated temperature profile is chosen, which is computed from equilibrium (see Fig. 2.6).

In Fig. 4.1 the axial velocity is plot against the calculation domain. The axial velocity of pre-mixture at inlet and axial velocity of products at outlet are denoted as $V_i$ and $V_o$, respectively. As previously analyzed, the burning velocity ($S_u$) equals to the inlet velocity ($V_i$), hence for stoichiometric methane/air $S_u = V_i = 38.04$ cm/s. The calculated burning velocity is much close to the experimental result of 39.00 cm/s given by Yamaoka and Tsuji [72]. Due to reaction, the axial velocity sharply increases during the reaction zone and reaches 286.47 cm/s at the outlet. Not far downstream the reaction zone, the axial velocity of the products nearly keeps constant.

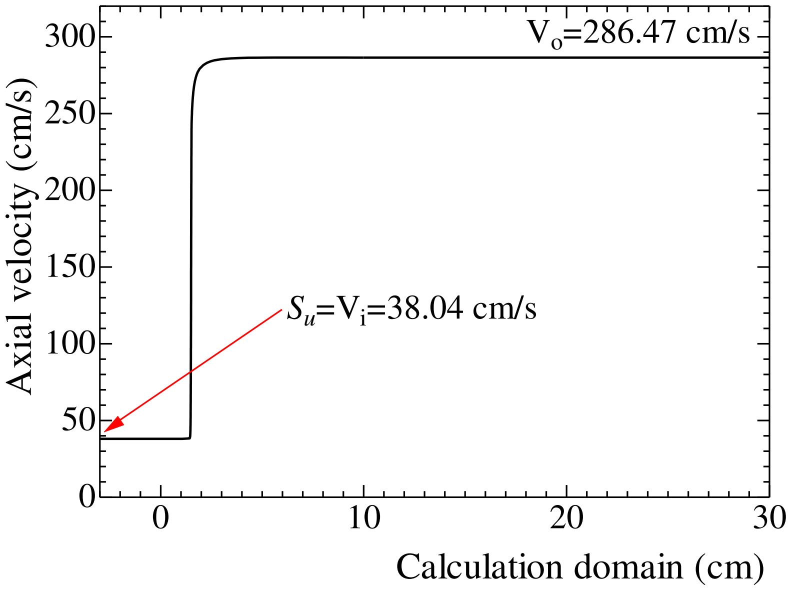

Fig.4.1 Axial velocity distribution along the calculation domain (-3 ~ 30 cm).

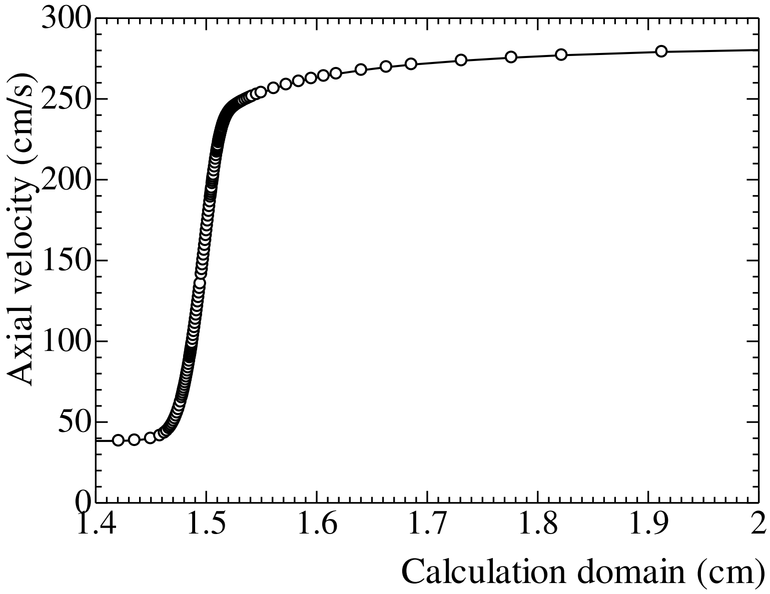

Fig.4.2 Axial velocity distribution close to the reaction zone (1.4 ~ 2.0cm).

Figure 4.2 shows local axial velocity as well as the grids distribution around the reaction zone where the axial velocity increases sharply. The position of the reaction zone is determined by the initial computation domain (0 ~ 3 cm), which by default lies at the middle ($x$ =1.5 cm) of the domain. The reaction zone is very thin, with the thickness less than 1 mm. Since the Chemkin-PRO software could self-adaptively adjust the grids distribution based the gradients of species or temperature et al, within the very thin reaction zone where large gradients exit, grids number over 150 are distributed. It means fine grid distribution with more than 150 grids-per-centimeter, has been achieved. Outside this zone, where the gradient is much small, coarse grid distribution of a few numbers is needed. The self-adaptive grids distribution is a remarkable advantage which not only assures enough accurate but also saves much computation costs. The concrete value of the reaction zone thickness will be discussed in section 4.3.

Figure 4.3 shows the temperature distribution within the total domain. The initial temperature ($T_{\mathrm{i}}$) at the inlet is 298K, while the flame temperature ($T_{\mathrm{o}}$) at the outlet reaches 2228 K.

In Fig. 4.4 the grids and temperature distribution around the reaction zone are shown. The temperature also increases sharply within the very thin reaction zone, which is around $x$ =1.5 cm.

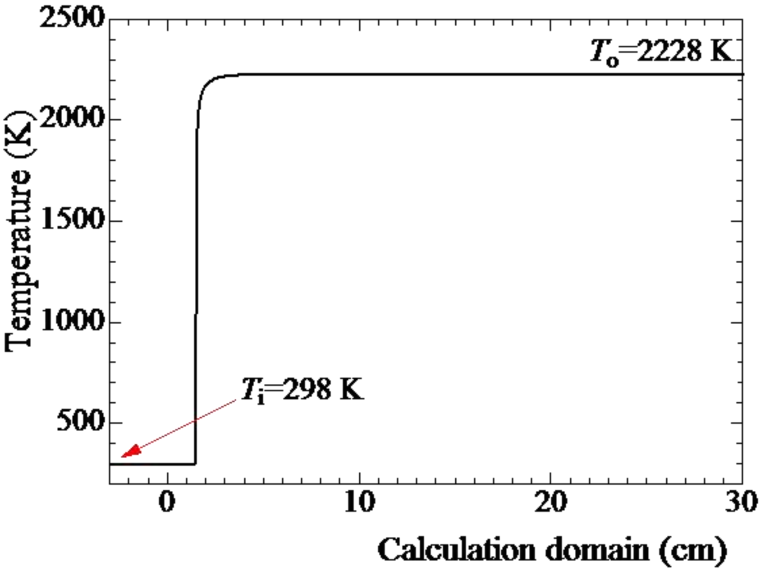

Fig. 4.3 Temperature distribution along the calculation domain (-3 ~ 30cm).

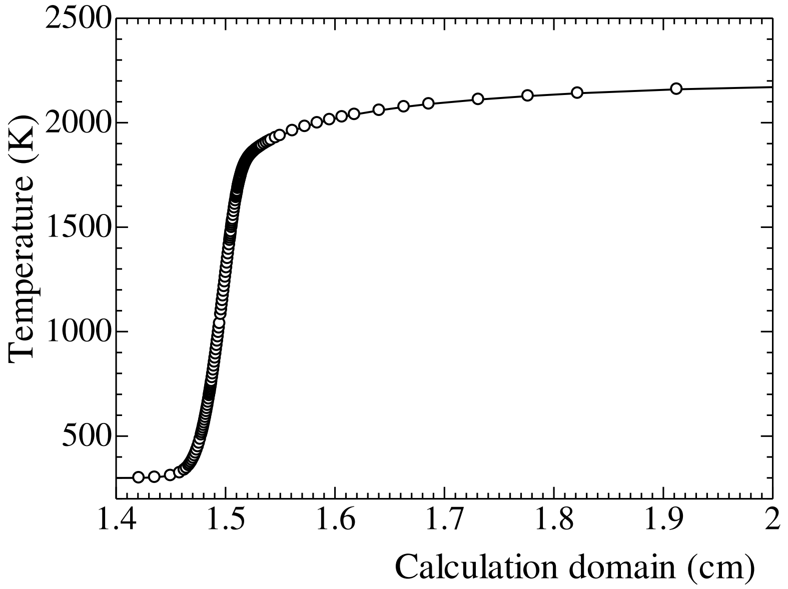

Fig. 4.4 Temperature distribution close to the reaction zone (1.4 ~ 2.0 cm).

In Fig. 4.5, the main reactants and products are plot against the distance ($x$) around the reaction zone. Before reaction, the mole fraction of methane is about a half of the oxygen mole fraction and both of them are almost unchanged, however, quickly they decrease in the reaction zone. The methane mole fraction becomes almost zero, while the oxygen mole fraction reduces slowly. The products $H_2O$, $CO_2$ and CO increase where the reactants reduce. During the process of $H_2O$ increasing, the CO firstly increases and reduces. The increase of $CO_2$ lies downstream that of the $H_2O$ due to the appearance of CO. Downstream the flame zone, the mole fractions of these products increase very slowly; further downstream the flame zone, these values keep almost constant.

Figure 4.6 show the mole fractions of some important species around the reaction zone. These species are only in small mole fraction comparing with the main reactants and products. The domain where these species sharply increase is downstream the domain where the axial velocity and temperature sharply increase.

Mentioned above introduces the calculation of laminar burning velocity at given equivalence ratio. With the same method the burning velocities of methane/air at various equivalence ratios could be calculated. Furthermore, by changing the composition of oxidizer in the unburned pre-mixture, the burning velocities under various oxygen mole fractions and equivalence ratios could also be obtained. In chapters 3 and 4, combustion tests were conducted under different conditions. For further discussion, the laminar burning velocities of methane/oxygen-air mixtures are calculated as a function of the equivalence ratio ($\Phi$) using the oxygen concentration ($\beta$) in the oxidizer as a parameter. The results are shown in Fig. 4.7.

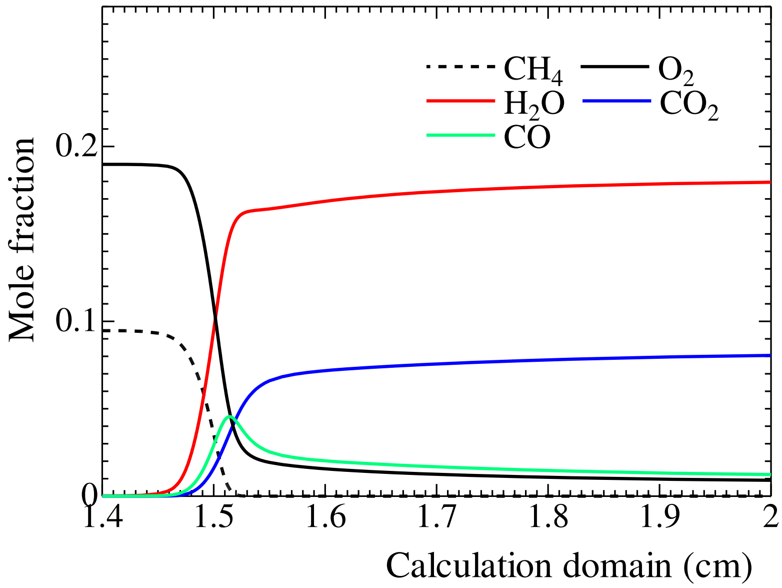

Fig. 4.5 Reactants products profile close to the reaction zone (1.4 ~ 2.0 cm).

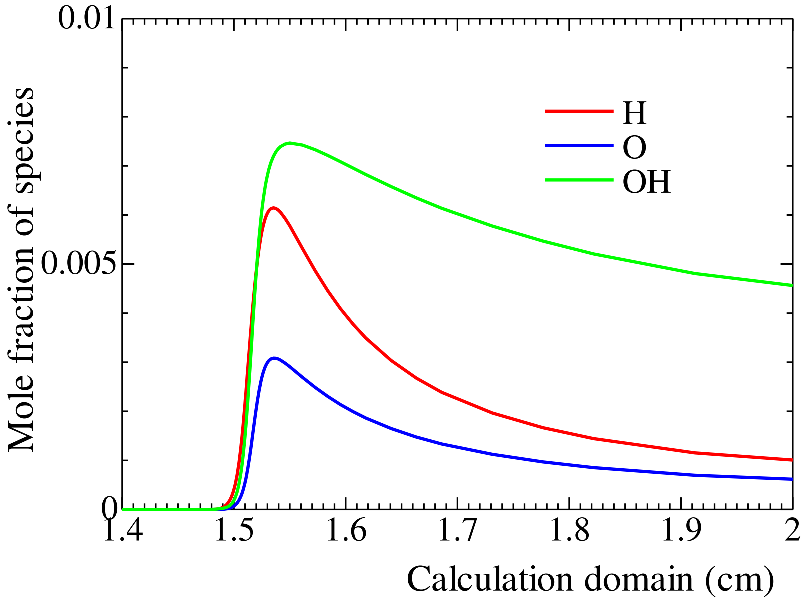

Fig. 4.6 Species profile close to the reaction zone (1.4 ~ 2.0 cm).

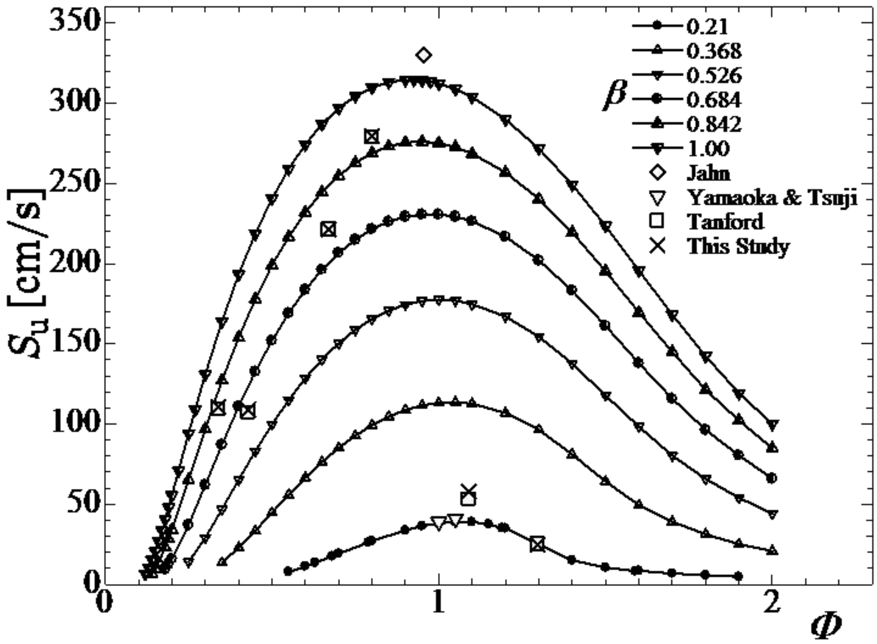

Fig. 4.7 Variations of burning velocity $S_u$ with the equivalence ratio $\Phi$ using the oxygen molar fraction $\beta$ as a parameter.

The upper equivalence ratio is set as 2.0, while the oxygen mole fractions are settled corresponding to the experimental condition in Fig.3.8 in chapter 3. It is seen in Fig. 4.7 that, at the same equivalence ratio, with an increase of oxygen mole fraction in the oxidizer, the burning velocity increase a lot. The stoichiometric burning velocity of methane/oxygen is almost eight times larger than that of methane/air. And with an increase of oxygen mole fraction, the calculated lean limits in equivalence ratio decrease. From lean limit to stoichiometric condition, the increase of burning velocity becomes more remarkable with the increment of oxygen mole fraction.

To substantiate the accuracy of the present calculation, experimental values that are available in literatures are compared with the calculations. They are shown in Fig.4.7.

In the case of air as an oxidizer, the burning velocity for the stoichiometric mixture in our calculation is 38.04 cm/s while Yamaoka and Tsuji (denoted by ▿) [72] obtained the value of 39.00 cm/s. As for the maximum burning velocity, the value in our calculation is 39.06 cm/s at the equivalence ratio of 1.064, while in experiments Yamaoka and Tsuji (▿) obtained the value of 41.00 cm/s at the equivalence ratio of 1.05 [72]; Scholte and Vaags [84] obtained the value of 40.00 cm/s at the equivalence ratio of 1.064. Thus, our calculations are very close to the experimental values.

In the case of pure oxygen as an oxidizer, the maximum burning velocity in our calculation is 314.0 cm/s at the equivalence ratio of 0.955, which is very close to the Jahn's experimental result (denoted by ◇) of 330 cm/s [82].

For various oxygen mole fractions and equivalence ratios, the calculated burning velocities in this study (×) are compared with the experimental data (□) obtained by Tanford [85]. The results show good agreements. Furthermore, it is very interesting to note that with increasing $\beta$, the equivalence ratio at which the burning velocity reaches its maximum shifts from rich to lean side of stoichiometric, which is qualitatively in accordance with the experimental results and consideration by Golovina and Fyodorov [86]. Based on the comparisons above, it may be concluded that the present calculations give the proper burning velocities for methane/oxygen-air mixture.

When the oxygen mole fraction is 0.368, as has been shown in Fig. 3.8 in chapter 3, the tubular flame could achieve around the stoichiometric condition. Based on the simulation results in Fig. 4.8, when $\beta$ =0.368, the maximum burning velocity is 113.61 cm/s at the equivalence ratio of 1.05. This means under this oxygen mole fraction tubular flame combustion could be established even at the maximum burning velocity of 113.61 cm/s. However, at the same injection flow rate of oxidizer, for pure oxygen combustion, when the equivalence ratio is larger than 0.18 where the burning velocity is over 40 cm/s, oscillation combustion occurs resulting in a failure of tubular flame establishment.

To further investigate this phenomenon, the ranges of burning velocities where tubular flame has been established under various oxygen mole fractions in the burners of W=2 and 1 mm, have been plot against the equivalence ratio, as shown in Fig. 4.8.

With oxygen mole fraction of 0.368, for tubular flame combustion in the burner of W= 1mm, the burning velocities vary from 13.46 to 113.61 cm/s. For $\beta$ =0.447, $Su$ = 10 ~ 85 cm/s; $\beta$ =0.526, $Su$ = 10 ~ 60 cm/s... It is seen that with an increase of oxygen mole fraction, the upper limit of burning velocities in tubular flame combustion decreases. For the cases of W=2 mm, the upper burning velocities also decreases and the value is smaller than that in W=1mm at the same oxygen mole fraction.

As previously introduced in chapters 3 and 4, at high oxygen mole fraction, the diffusion flames are easily anchored at the exits of the fuel slits. This diffusion flame interrupts the mixing of fuel and oxidizer, and causes intense oscillatory combustion in the swirling flow downstream the slit. Thus tubular flame combustion is established at low equivalence ratio with low burning velocity.

Therefore, when the oxygen mole fraction is high, the flow requirement for stable tubular flame establishment, that the burning velocity should balance the radial velocity, is not enough. The diffusion flames established between the fuel and oxidizer streams are necessarily to be inhibited.

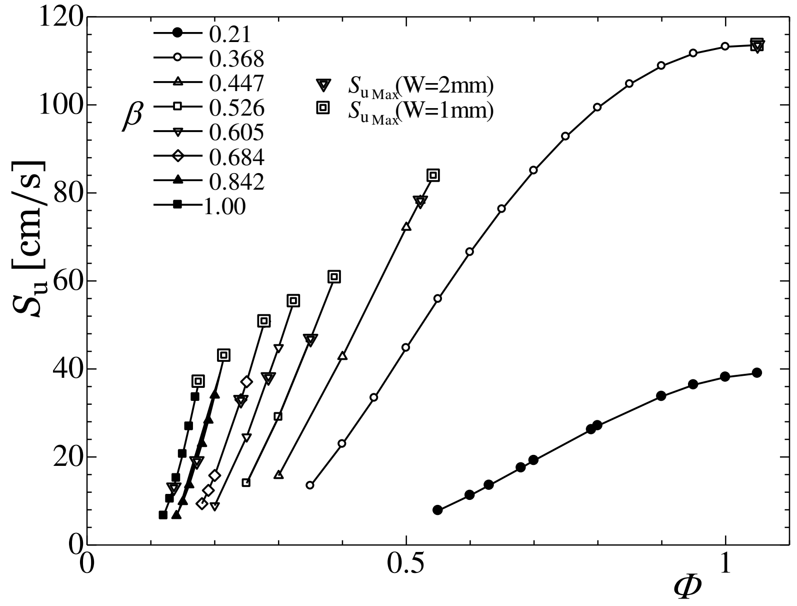

Fig. 4.8 Burning velocities of the mixtures which sustain tubular flame in the rapidly mixed type combustion.

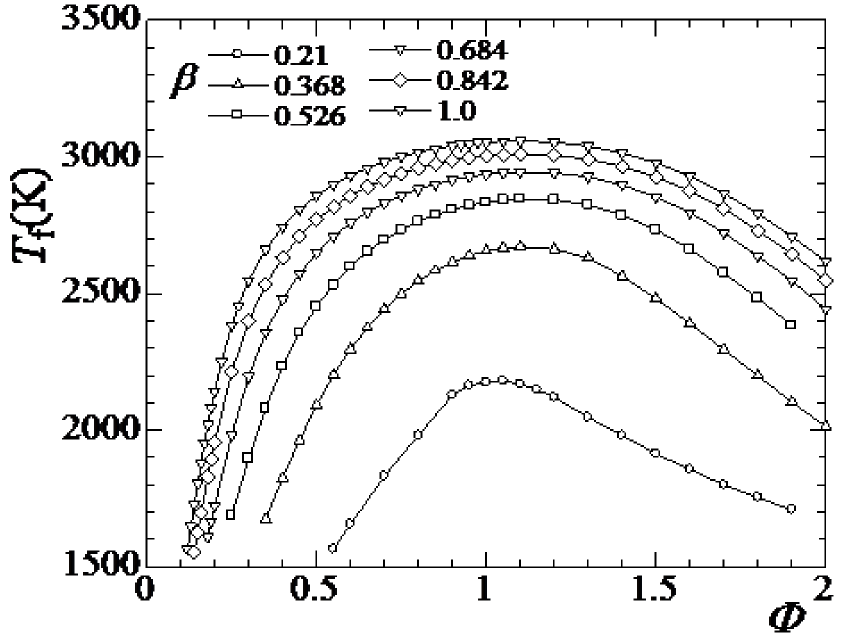

Fig. 4.9 Adiabatic flame temperatures $T_f$ as a function of equivalence ratio $\Phi$ using the oxygen molar fraction $\beta$ as a parameter.

The adiabatic flame temperature is obtained along with the burning velocity calculation. According to the oxygen mole fractions in Fig. 3.8 in chapter 3, the adiabatic flame temperatures are computed with various equivalence ratios. The results are shown in Fig. 4.9.

For current burners, when oxygen mole fraction is less than about 0.4, stable tubular flame could be established within the whole inflammable range. Under these conditions, stable and uniform distributed tubular flame with adiabatic temperature as high as 2700 K could be obtained. However, to seek higher adiabatic flame temperature at high oxygen mole fractions, the diffusion flames and oscillatory combustion should be effectively controlled.

This study addressed the pure oxygen combustion of methane. For deep investigation, the simulation results of methane/oxygen are discussed in the following.

In Figs. 4.10 and 4.11, the axial velocity is plot against the plane of equivalence ratio ($\Phi$) and computation distance ($x$). As long as the equivalence ratio and distance are given, the axial velocity could be obtained from Fig.4.10. The total computation distance is 55 cm (-5 ~ 50 cm), while the equivalence ratio increase from 0 to 2. For a given distance, for instance, at the inlet ($x$ = -5 cm), the initial velocity also known as the burning velocity, increases when the equivalence ratio increases from 0 to around 1 and then decreases with a further increase of equivalence ratio. Downstream the inlet ($x$ > -5 cm), at a fixed distance, the axial velocity becomes larger than that at the inlet, however, it also follows the same increase-reduce trend, whose section view at constant $x$ is a parabolic shape. The maximum axial velocity reaches almost 4000 cm/s at the equivalence ratio of 0.95 in the domain downstream the reaction zone.

At any given equivalence ratio, the axial velocity increases slowly from the inlet to the reaction zone. And sharp increase occurs in the reaction zone (around $x$ =1.5 cm), as shown in Fig. 4.11. Downstream the reaction zone, the axial velocity increases much slowly and finally becomes a constant.

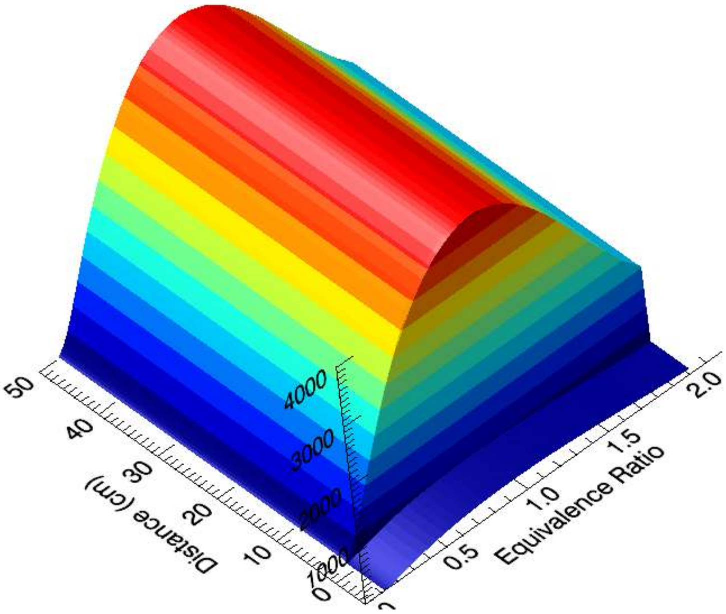

Fig. 4.10 Three dimensional axial velocity distribution in the plane of equivalence ratio $\Phi$ and computation distance ($x$).

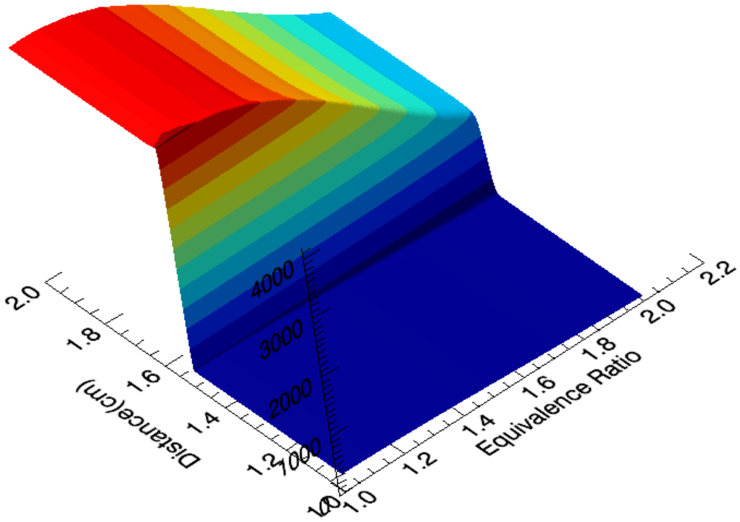

Fig. 4.11 Three dimensional axial velocity distribution near the reaction zone (around $x$ =1.5 cm) and $\Phi = 1.0 \sim 2.0$.

In Figs. 4.12 and 4.13, the gas temperature is plot against the plane of equivalence ratio ($\Phi$) and computation distance ($x$). Downstream the reaction zone, for given distance, the flame temperature increase fast from equivalence ratio of 0.1 to 0.55 then

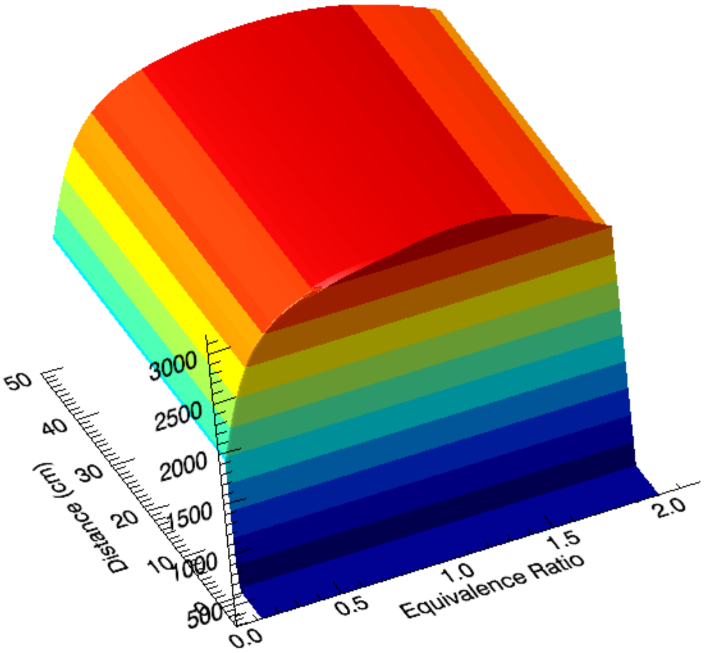

Fig. 4.12 Three dimensional temperature distribution in the plane of equivalence ratio $\Phi$ and computation distance ($x$).

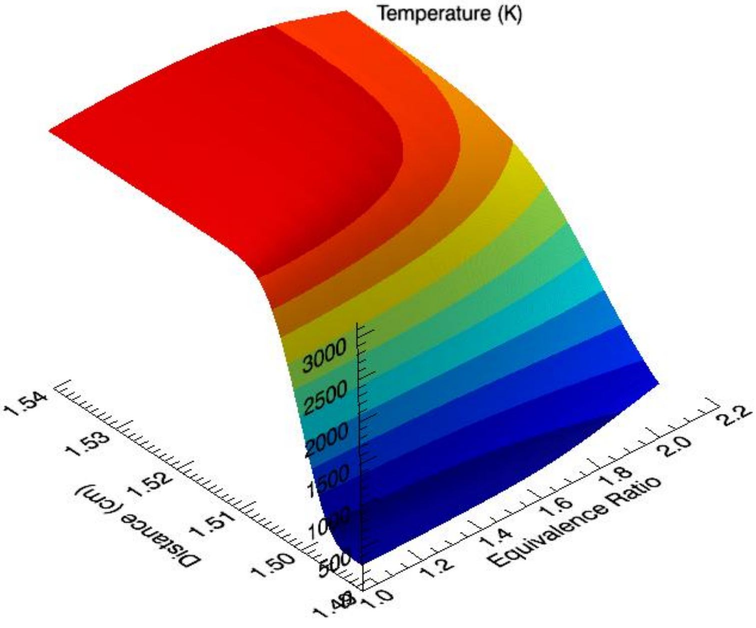

Fig. 4.13 Three dimensional axial velocity distribution near the reaction zone ($x$ =1.49 ~1.54 cm) and $\Phi = 1.0 \sim 2.0$.

the increasing trend slows down from $\Phi = 0.55$ to $\Phi = 1.1$. Above $\Phi = 1.1$, where the flame temperature is 3058 K, the flame temperature decreases.

### 4.2.2 Summary of burning velocities

The laminar burning velocities of methane/oxygen-air mixtures have been calculated and examined reliable. These data as well as the adiabatic flame temperature provide important references for burner design and phenomenon analysis. Based on these computations, the burning velocities as well as the adiabatic flame temperature of $CH_4/O_2$-$CO_2$ are calculated for oxy-fuel combustion; those of $H_2/O_2$ and $C_3H_8/O_2$ are also calculated for pure oxygen combustion.

In Fig. 4.14, under various equivalence ratios and oxygen mole fractions, the burning velocities of $CH_4/O_2$-$CO_2$ mixtures are computed and compared with that of $CH_4/O_2$-$N_2$ ($CH_4/O_2$-Air) at the same conditions. Open signs with color lines show the burning velocities of $CH_4/O_2$-$CO_2$ while the enclosed signs with black lines show those of $CH_4/O_2$-$N_2$. It is seen that, the burning velocity of is $CH_4/O_2$-$CO_2$ is much smaller comparing with that of $CH_4/O_2$-$N_2$ at the same oxygen mole fraction and equivalence ratio. For example, at the oxygen mole fraction of 0.5, the burning velocity of $CH_4/O_2$-$CO_2$ is almost half of the $CH_4/O_2$-$N_2$ mixture for nearly all the equivalence ratios. At high oxygen mole fractions, the difference of burning velocities between the two cases becomes smaller.

Figure 4.15 shows the adiabatic flame temperatures of $CH_4/O_2$-$CO_2$ compared with that of $CH_4/O_2$-$N_2$ mixtures. Just like the burning velocity, the flame temperature of $CH_4/O_2$-$CO_2$ mixture is smaller than of $CH_4/O_2$-$N_2$. For instance, at the oxygen mole fraction of 0.4, the maximum flame temperature is $CH_4/O_2$-$CO_2$ about 2500 K while that of $CH_4/O_2$-$N_2$ is about 2700 K.

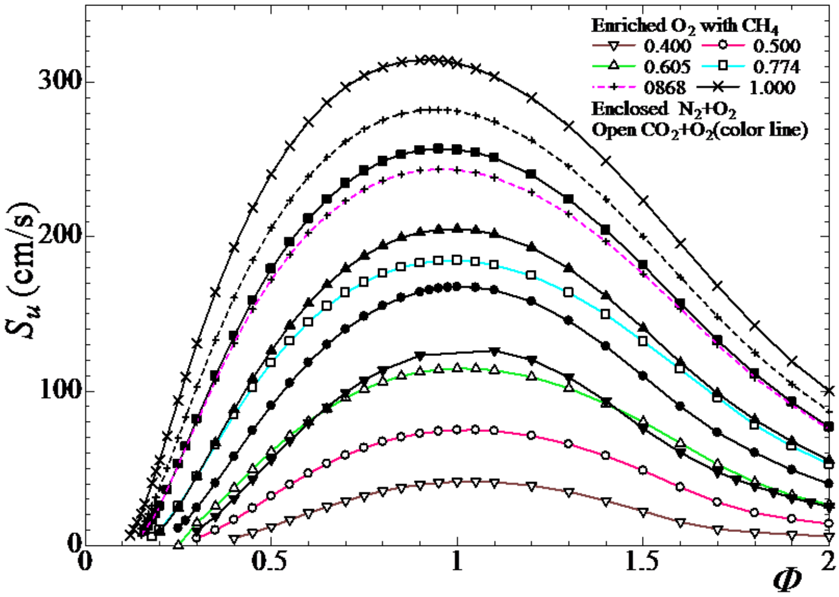

Fig. 4.14 Burning velocities comparisons between $CH_4/O_2$-$N_2$ and $CH_4/O_2$-$CO_2$ under various $\Phi$ and $\beta$ .

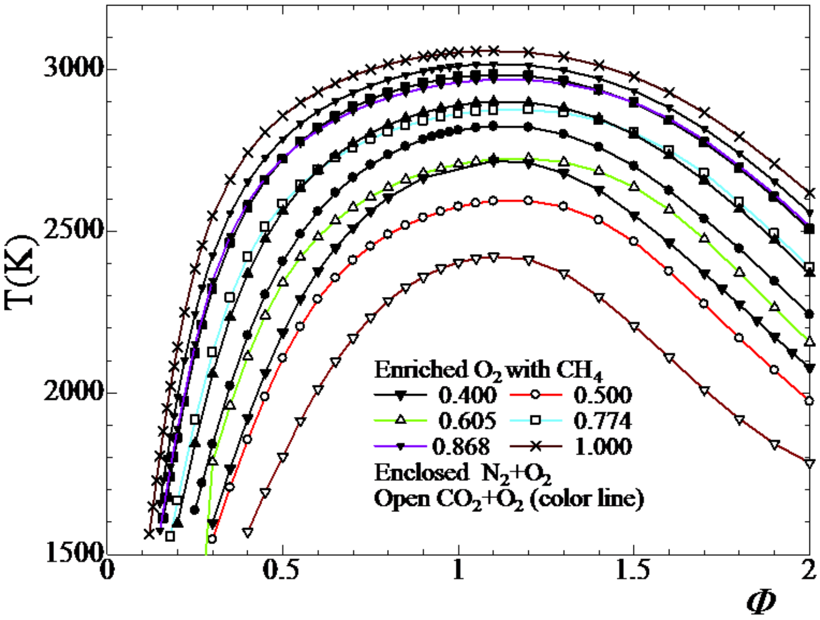

Fig. 4.15 Adiabatic flame temperature comparisons between $CH_4/O_2$-$N_2$ and $CH_4/O_2$-$CO_2$ under various $\Phi$ and $\beta$ .

With the reaction scheme GRI-Mech version 3.0 the laminar burning velocities of $H_2$/Air and $H_2/O_2$ are calculated. As shown in Fig.4.16, the broken line and solid line show the calculated burning velocities in the equivalence ratio of 0 ~ 8.0. For $H_2$/Air, the maximum burning velocity of is around 291 cm/s at the equivalence ratio of 1.78. With various equivalence ratios, the experimental data of Tse et al. [87] and Kwon and Faeth [88] are plotted to compare with present calculations. The results show very good agreement. While the experimental results of Guntherr and Janisch [89] are slightly larger than the calculated results.

For $H_2/O_2$, the burning velocity increases remarkably from very lean to stoichiometric condition. The maximum burning velocity is 950.6 cm/s in this calculation at the equivalence ratio of 1.15. In numerical calculation Dixon-Lewis [90] obtained the burning velocity of 941 at stoichiometric condition, which is very close to the value of 942.3 cm/s in this study. The experimental data of Jahn [72] and Zitoun and Deshaies [91] in Fig. 4.16 are very close to present calculation. Based on the comparisons above, it may be concluded that the present calculations give the proper burning velocities for $H_2$/air and $H_2/O_2$ mixtures.

In Fig. 4.17, the adiabatic flame temperature of $H_2$/air and $H_2/O_2$ mixtures are plotted against the equivalence ratios, respectively. The maximum temperatures are 2400 and 3076 K, respectively, both of which are at the equivalence ratio of 1.05. For both mixtures, the flame temperature increases rapidly from lean to stoichiometric condition.

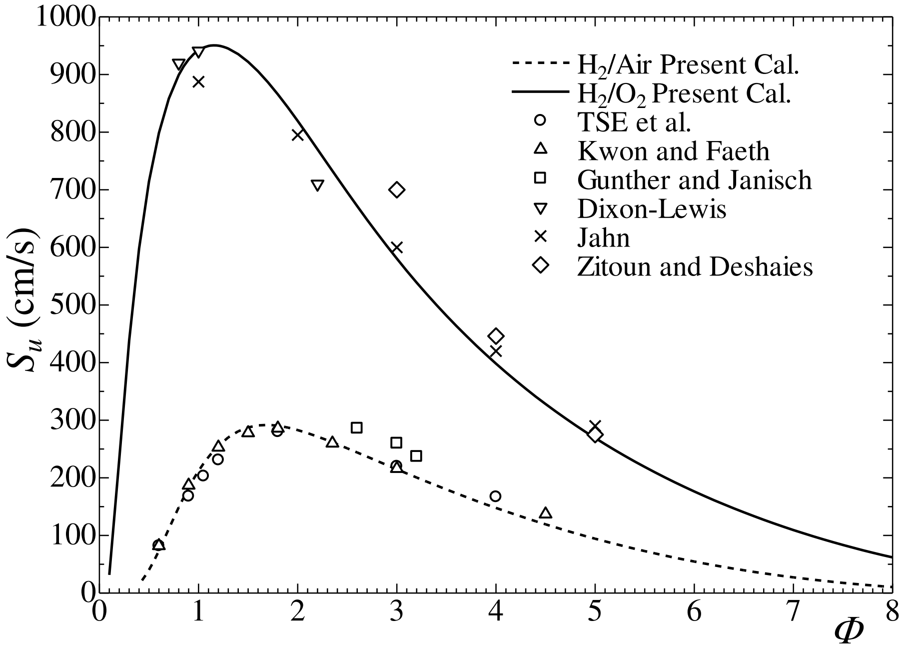

Fig. 4.16 Burning velocities of $H_2/O_2$ and $H_2$/Air mixtures under various $\Phi$.

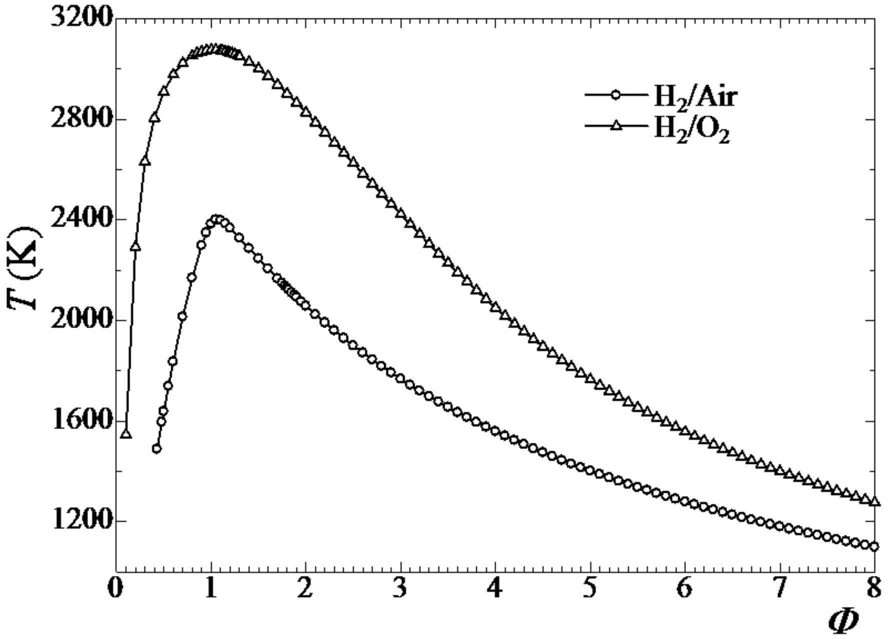

Fig. 4.17 Adiabatic flame temperature of $H_2/O_2$ and $H_2$/Air mixtures under various $\Phi$.

The laminar burning velocities of $C_3H_8/O_2$ mixtures under various equivalence ratios are also summarized. Two reaction schemes from University of California at Sandi Ego [92] and Princeton University [93] are used to calculate the burning velocities, respectively. The results are shown in Fig. 4.18. It is seen that from lean to equivalence ratio of 0.8, the calculated results are much close. Above 0.8, the calculated results based on Sandi Ego mechanism are slightly bigger than those of Princeton. The maximum burning velocities are 310 and 305 cm/s for Sandi Ego and Princeton mechanism, respectively, both of which are obtained around the equivalence ratio of 0.9.

Figure 4.19 shows the adiabatic flame temperature. It is seen that the adiabatic flame temperatures are almost the same for both types of mechanisms. The flame temperature rapidly increases to about 2900 K at the equivalence ratio of 0.5, which may be an important application in energy saving in high temperature industrial fields. The maximum temperature is 3099 K at the equivalence ratio of 1.1.

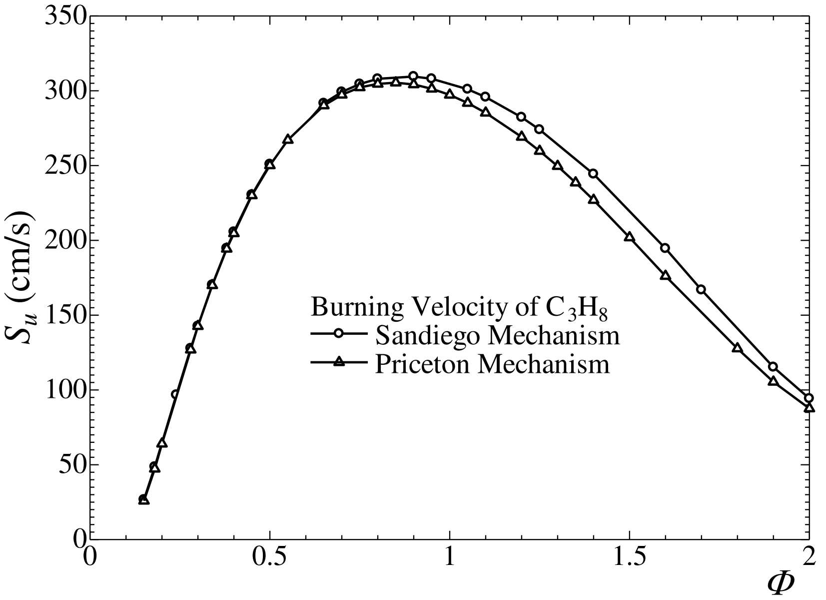

Fig. 4.18 Burning velocities of $C_3H_8/O_2$ calculated with different mechanisms under various $\Phi$.

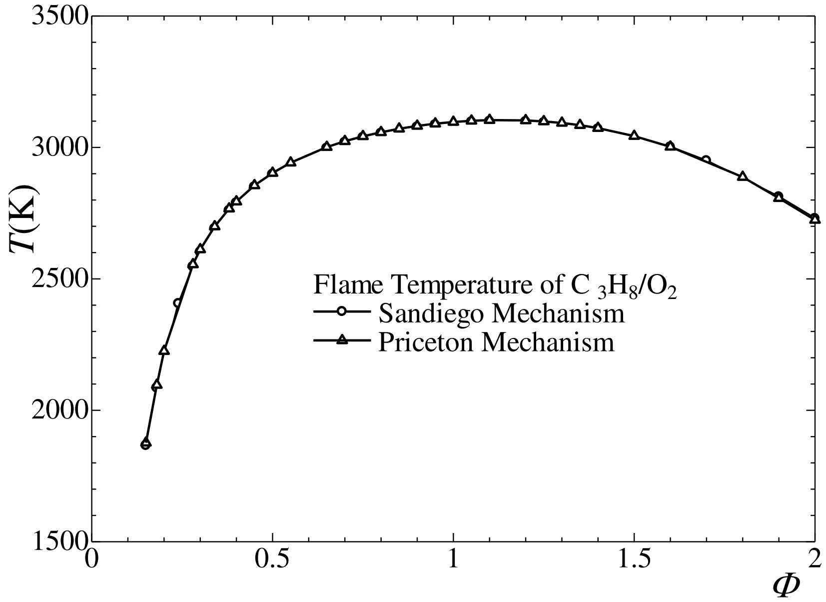

Fig. 4.19 Flame temperatures of $C_3H_8/O_2$ calculated with different mechanisms under various $\Phi$.

## 4.3 Reaction time

### 4.3.1 Flame thickness

There are different ways to define the flame thickness either from the knowledge of burning velocity and fresh gas properties or from the temperature profiles [94]. In this study, we choose the best definition as proposed in a text book [94], that the laminar flame thickness $\delta_L$ is determined by computing the temperature profile and using the following equation:

$$\delta_L = \frac{T_b - T_u}{\max(|\partial T / \partial x|)}, \tag{4.2}$$

in which $T_u$ and $T_b$ are unburned and burned gas temperatures respectively (just equal to the $T_i$ and $T_o$ defined previously), and $\partial T / \partial x$ is temperature gradient.

We have obtained reliable burning velocities of methane/oxygen-air mixture through numerical calculation. The temperature profiles are given along with the burning velocity calculation. Thus, the flame thickness can be conveniently calculated through Eq. (4.2). Two cases of methane/oxygen mixture at different equivalence ratios are discussed, as shown in Figs. 4.20 and 4.21.

For $\Phi = 0.15$ as shown in Fig. 4.20, the unburned and burned gas temperatures are $T_u = 298$ K and $T_b = 1806$ K obtained with $S_u = 20.77$ cm/s , respectively. Based on the temperature profile, the temperature gradient along the distance ($x$) is calculated and we obtain $\max(|\partial T/\partial x|) = 3.5\times10^{6}$ K/m at the distance of $x$ = 1.5091 cm.

Through Eq. (4.2), the laminar flame thickness $\delta_L = 430.9\ \mu\text{m}$ is obtained as shown in Fig. 4.20, which lies in the domain $x$ = 1.48756 ~ 1.53064 cm.

However, with an increase of equivalence ratio, say double equivalence ratio ($\Phi = 0.30$), as shown in Fig. 4.21, the flame thickness reduces to almost 1/3 that of the $\Phi = 0.15$. The calculated burning velocity and flame temperature are 131.0 cm/s and 2547 K, respectively, both of which are remarkably increase than those of $\Phi = 0.15$. The temperature increases sharply in the reaction zone, and we obtained that $\max(|\partial T/\partial x|) = 1.9\times10^{7}$ K/m, which is one order larger. Consequently the flame thickness is given as $\delta_L = 118.4\ \mu\text{m}$. The flame thickness of methane/oxygen mixture

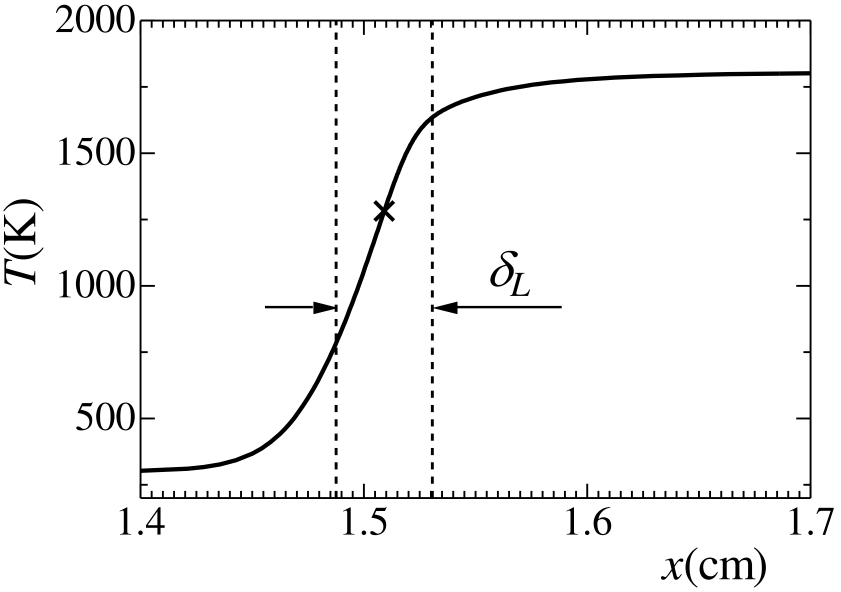

Fig. 4.20 Laminar flame thickness ($\delta_L$) of $CH_4/O_2$ mixture at $\Phi = 0.15$.

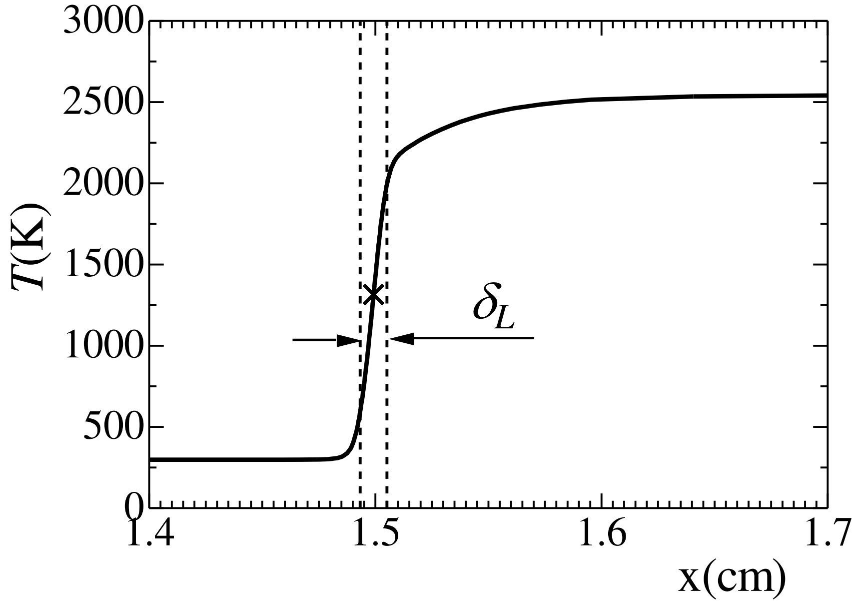

Fig. 4.21 Laminar flame thickness ($\delta_L$) of $CH_4/O_2$ mixture at $\Phi = 0.30$.

for various equivalence ratios are calculated and listed in Table 1. It is seen that from $\Phi = 0.12$ to $\Phi = 0.3$, the flame thickness decreases rapidly with an increase of equivalence ratio. With further increasing of $\Phi$, the thickness also decreases but slows down.

### 4.3.2 Reaction time

Until now, the laminar flame thickness ($\delta_L$) and burning velocity ($S_u$) have been successfully calculated, thus the reaction time ( $\tau_r = \delta_L / S_u$ ) can be easily calculated. Here the reaction times of some combustion tests discussed in Chapter 3 are calculated and listed in Table 4.1.

As seen in Table 4.1, with an increment of equivalence ratio ($\Phi$), the burning velocity as well as the flame temperature and maximum temperature gradients increases rapidly, while the laminar flame thickness decreases fast. Thus, the reaction time decreases remarkably. For $\Phi$ = 0.12, the reaction time is about 19400 μs, while it reduces to 32 μs at the equivalence ratio of 0.5.

Table 4.1
Reaction time $\tau_r$

| $\Phi$ | $T$[K] | $(\partial T/\partial x)_{max}$ [K/m] | $S_L$[cm/s] | $\delta_L$[μm] | $\tau_r$[μs] |
|---|---|---|---|---|---|
| 0.12 | 1561 | 1.00E+6 | 6.645 | 1263.0 | 1.90E+4 |
| 0.15 | 1804 | 2.60E+6 | 20.77 | 430.9 | 2.07E+3 |
| 0.17 | 1950 | 5.00E+6 | 33.7 | 330 | 981 |
| 0.3 | 2547 | 1.90E+7 | 131.0 | 118.4 | 90 |
| 0.5 | 2858 | 3.30E+7 | 240.9 | 77.6 | 32 |
| 1.0 | 3054 | 8.00E+7 | 312.8 | 34.45 | 11 |

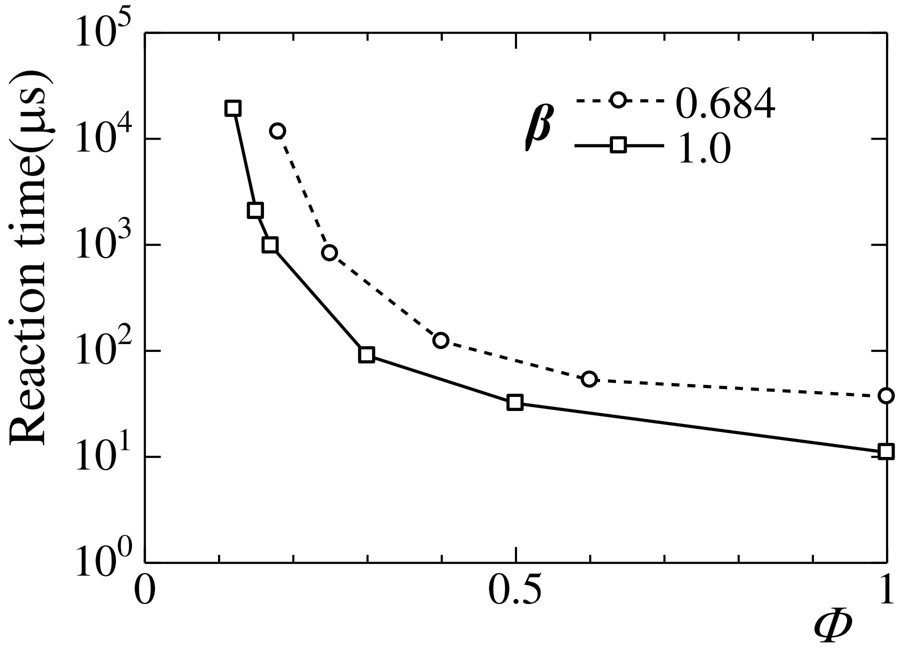

Fig. 4.22 Variation of reaction time with equivalence ratio.

In Fig. 4.22, the reaction time for $\beta$ = 0.684 and 1.0 are plotted against the equivalence ratio. For both cases, the reaction time reduces remarkably form very lean condition to around $\Phi$ = 0.5. Above $\Phi$ = 0.5, the reaction time slowly decreases with an increase of equivalence ratio. And at the same equivalence ratio, the reaction time of $\beta$ = 0.684 is larger than that of $\beta$ = 1.0.

## 4.4 Summary

In this chapter, the burning velocity and reaction time are computed with the Chemkin Premix code. With appropriate initial and boundary conditions, the burning velocity of stoichiometric methane/air mixture is discussed as an example. Then the burning velocities of methane/oxygen-air mixtures under various oxygen mole fractions and equivalence ratios are computed and compared with experimental data. The flame thickness is computed through the temperature profile obtained along with the burning velocity calculation. Based on these analyses, the reaction time is calculated. The following are concrete conclusions.

(1) The burning velocities of methane/oxygen-air mixtures under various oxygen mole fractions and equivalence ratios are computed and the results show good agreement with experimental data.

(2) The burning velocities and flame temperature of $CH_4/O_2$-$CO_2$, $H_2/O_2$ and $C_3H_8/O_2$ are summarized for oxy-fuel combustion.

(3) Laminar flame thickness is computed through the temperature profile obtained along with the burning velocity calculation.

(4) The reaction time is calculated. For methane/oxygen mixture, with an increase of equivalence ratio, the reaction time reduces rapidly.

# Chapter 5 Mixing Process Analysis in the Rapidly Mixed Type Tubular Flame Burner

## 5.1 Introduction

One of the fundamental aspects of the rapidly mixed tubular flame combustion is the mixing of fuel and oxidizer, which should be complete before the onset of reaction. A sound understanding of the mixing process is of considerable importance for the advancement of improved physical concepts and predictive models in such type of burner.

### 5.1.2 Overview of previous researches for mixing

Mixing of fuel and oxidizer has a great influence on the overall performance of combustion in various kinds of combustors, say, air breathing engine [95, 96], fluidized bed combustor [97, 98] and jet burner [29, 99, 100]. Extensive research has been carried out on the mixing of fuel and oxidizer in shear or mixing layers formed between two reactant streams. As shown in Fig. 5.1, using a burner with two separate jets, the mixing of $CH_4$-$H_2$ jet with $O_2$ jet has been analyzed [30].

The mixing layers are found in all types of non-premixed combustion including the initial region of jets or the wake region of bluff-body stabilized burner [101].

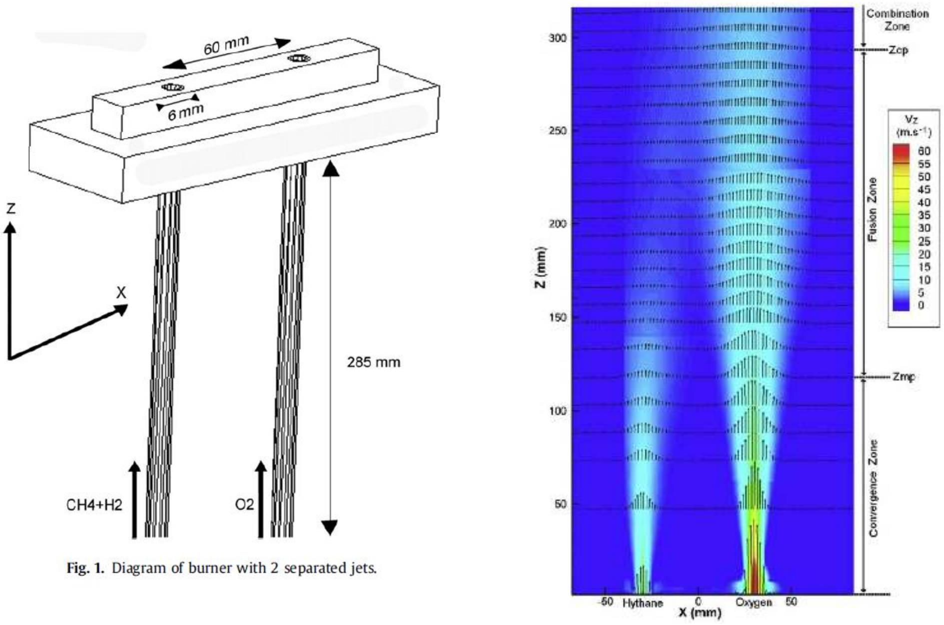

**Fig. 1.** Diagram of burner with 2 separated jets.

Fig. 5.1 Burner diagram (left) and mean two dimensional velocity fields (right, non-reacting) [30].

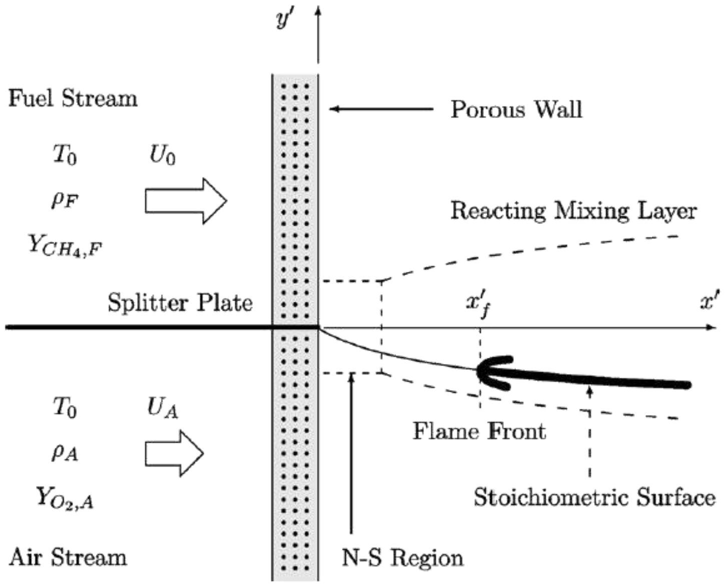

Fig. 5.2 Schematic illustration of the two-dimensional reacting mixing layer between parallel streams of fuel and air emerging from porous walls, which shows the coordinates and the upstream boundary conditions [102].

Fernández-Tarrazo et. al made a numerical analysis to describe the lift off and blow off of a diffusion flame in the mixing layer between two parallel streams of fuel (mainly methane diluted with nitrogen) and air emerging from porous walls [102]. The configuration of the model is shown in Fig. 5.2.

In planar mixing layer, to study the fundamental processes of mixing as well as chemistry, the flow configuration has been measured by various methods including LDV[103], OH LIF/soot LII technique [104] and PIV system [105]. In the left part of Fig. 5.3, the planar mixing layer configuration of heated-air with air-acetone under different temperatures and velocities are shown [104]; in the right pictures, the reacting mixing layer was visualized using a combined OH LIF/soot LII technique, wherein the reaction zone and the region of parent fuel entrainment and decomposition were simultaneously imaged.

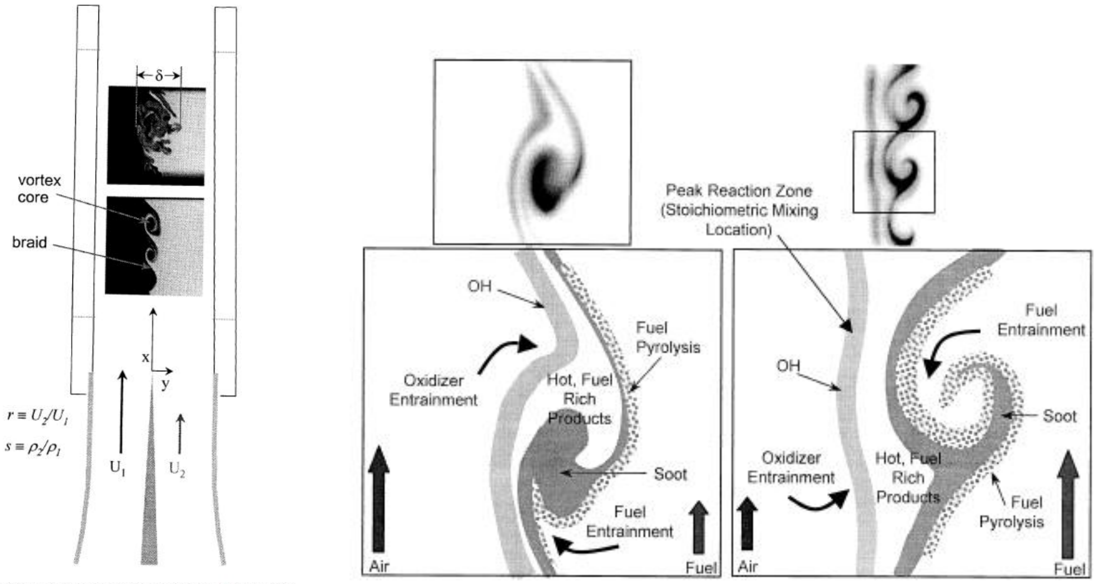

Fig. 1. Planar mixing layer configuration. Non-reacting passive scalar images insets shown were acquired at $p = 4$ atm with heated air in stream 1 ($T_1 = 400$ K and $U_1 = 2$ m/s) and air seeded with acetone vapor ($T_2 = 300$ K and $U_2 = 0.8$ m/s) in stream 2.

Fig. 7. Schematic depicting mixing layer structure for AHS case (left) and FHS case (right). The schematic is based on OH/LII images from Position B for the boxed region shown at the top for case A2 (left) and F2 (right).

Fig. 5.3 Planar mixing layer configuration (left) and schematic depicting mixing layer structure for AHS and FHS cases (right) [104].

The mixing layers between non-parallel streams have also been investigated by different structures [106, 107]. Specially, as an important aspect, the swirling mixing layers are addressed here. The swirling mixing layers form an integral part of many combustion and propulsion systems, contributing significantly to their performance and noise generation. With a swirl generator, Wood et al [108] investigated the detailed structure of a swirling turbulent mixing layer. While Chen and Driscoll [109] have investigated the role of the recirculation vortex in improving fuel-air mixing within swirling flames. They investigated the effects of swirl on flame length in detail, as shown in Fig. 5.4 [109]. The effects of fuel-air mixing on flame structures and $NO_x$ emissions in a swirling flame have been analyzed in gas turbine combustor [110] and jet flames [111].

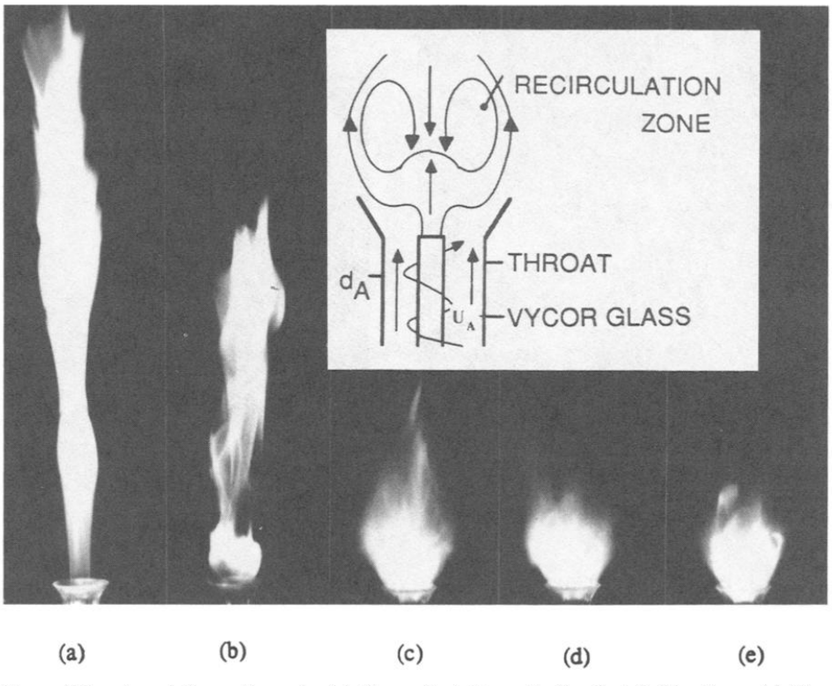

FIG. 1. Effect of Swirl on Flame Length. Methane fuel flowrate fixed at 0.03 g/sec. (a) No swirl, (b) S = 0.2, bulbous recirculation forms at base of "jet-like" flame, (c) S = 0.25, (d) S = 0.5, (e) S = 1.1.

Fig. 5.4 Effect of swirl on flame length [109].

### 5.1.2 Mixing process in rapidly mixed tubular flame combustion

However, the mixing layer developed in the rapidly mixed type burner has not yet been investigated. Due to the structure of the current burners, the configuration of the mixing layer developed in the swirling flow is totally new and different from the cases mentioned above.

In the rapidly mixed fuel/air tubular flame combustion, to achieve stable tubular flame as that of premixed type, the injection velocities higher than 20 m/s and swirl numbers larger than 5 are required for complete mixing of fuel and air [33]. And it also has been argued that the tubular flame front is stabilized at a position where the burning velocity balances the radial velocity [34, 55]. Due to very high reaction rate and significantly high burning velocity in pure oxygen combustion, it is unknown whether these requirements are still valid or enough for establishing tubular flame combustion. Comparing with fuel/air combustion, the mixing of fuel and oxygen will enhance a lot just by eliminating the diluent of $N_2$, however, the reaction rate will also increase owing to less heat loss carried away by $N_2$. Thus, quantitatively analysis between the mixing and reaction is necessary for investigating the establishment of tubular flame combustion under high oxygen mole fraction.

On the other hand, as has been introduced in Chap.3, by reducing the slit width, stable tubular flame (premixed flame) was obtained instead of diffusion flame (non-premixed flame). For further analysis, in this chapter, the mixing process is investigated with PIV system using three types of quartz burners whose slit widths are 3, 2, and 1 mm, respectively. The mixing layer thicknesses are measured and discussed under the same and different injection velocities of seeded and non-seeded flows.

With the relations between mixing layer thickness and injection velocity which are obtained under low flow rates, the mixing layer thicknesses of the combustion tests are estimated. It has been proved that the estimation is valid even under increased flow rates and combustion condition. Based on the mixing layer thickness mixing time has been calculated.

## 5.2 Mixing layer at the same injection flow rate

### 5.2.1 Low injection velocity

To capture the mixing process in the tubular flame burner, the flow field was investigated with using a PIV system (see chapter 2). Dry air and nitrogen supplied from cylinders were used. It should be noted that due to difficulties for visualization, the injection velocities were much lower than the combustion tests discussed in chapters 3 and 4.

#### 5.2.1.1 Flow visualization

Figure 5.5 shows the flow visualization inside the two optically accessible burners at the injection flow rate of $0.048\ \mathrm{m^3{}_N/h}$. The broken lines show the positions of the tangential slits and the broken circles show the positions of the burner walls. From two slits of upper left and lower right, nitrogen flows seeded with MgO particles were tangentially injected into the burner, while dry air flows without seeding were injected from another two slits of upper right and lower left. Flow visualizations were obtained in a plane parallel to the sheet 2 mm offset the center of the slit to get more particles, hence, higher quality images.

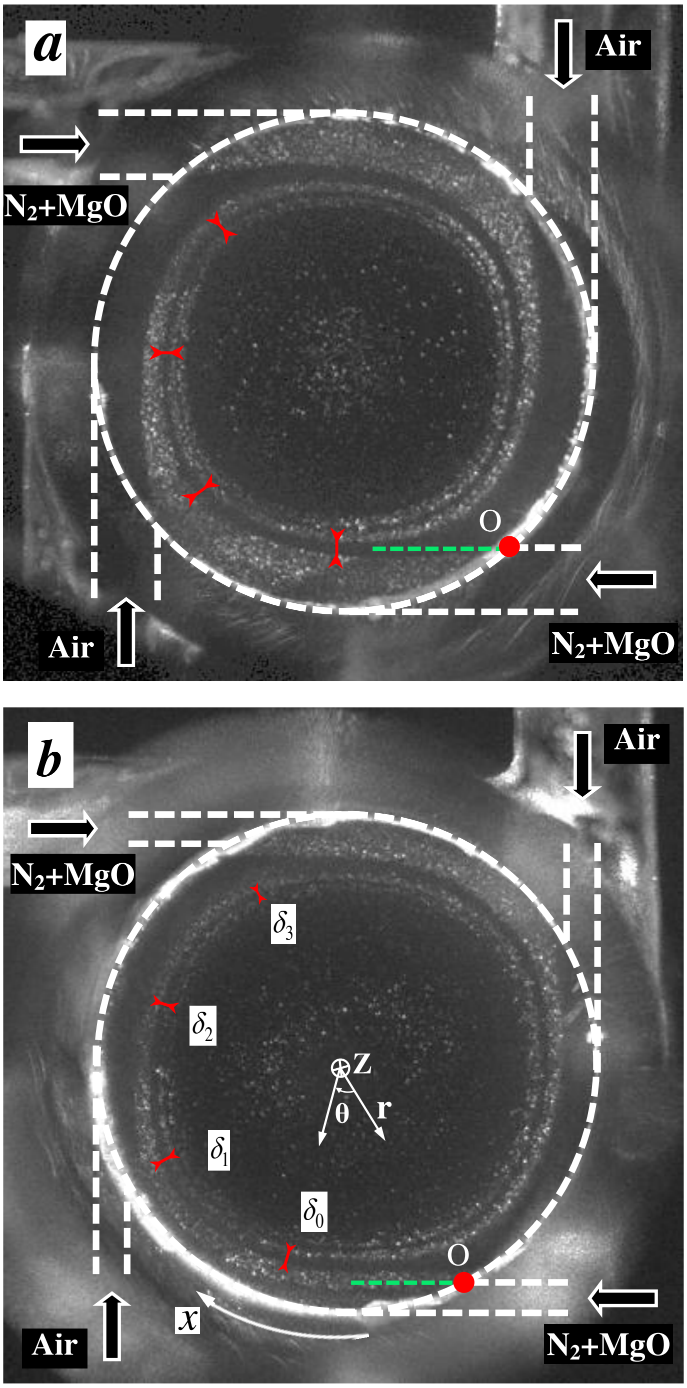

Fig. 5.5 Flow visualization ($Q = 0.048$ m$^3$/h   a: W=2mm, b: W=1mm).

In the case of W=2 mm, it is seen in Fig. 5.5a that the seeded flow from the lower right slit abruptly shrinks in width after the flow is injected from the 2 mm width slit through an interaction with the non-seeded flow from the upper right slit. This non-seeded flow also shrinks in width through the interaction with the flow from the upper left, and as illustrated by red arrows, the width of the flow from the upper right slit gradually decreases as the stream goes around.

In the case of W=1 mm, it is seen in Fig. 5.5b that the seeded flow from the lower right slit once slightly expands in width when the flow is just injected outside from the slit, however, the flow shrinks thereafter and the width gradually decreases. The non-seeded flow from the upper right slit also shrinks and its width, indicated by red arrows, decreases.

To quantify the decrease in the width, we define a starting point as the inner edge of the slit, which is shown by a red point (O), and take a coordinate along the circle. Beginning from the point O, we measured the width every 45°, and denoted the width by $\delta_0$, $\delta_1$, $\delta_2$ and $\delta_3$, as shown by the red arrows in Fig. 5.5b.

The values of $\delta_0$, $\delta_1$, $\delta_2$ and $\delta_3$, measured at a condition of average injection velocity $V_t = 0.833$ m/s with the 1 mm slit width burner, are shown in Fig. 5.6. Here, the lateral coordinate is the circumferential distance $(x)$ from the point O. The width gradually decreases with increasing $x$. These widths are carefully examined. Although the deviations are quite small, the scatters in the measurements are added in the form of error bars in the figures to show how well they match to their own curves. And it is found that $\delta_2$ and $\delta_3$ are almost inversely proportional to each other, whereas

$\delta_0$ and $\delta_1$ show quite different tendency from $\delta_2$ and $\delta_3$. This suggests that different types of flows coexist in the burner.

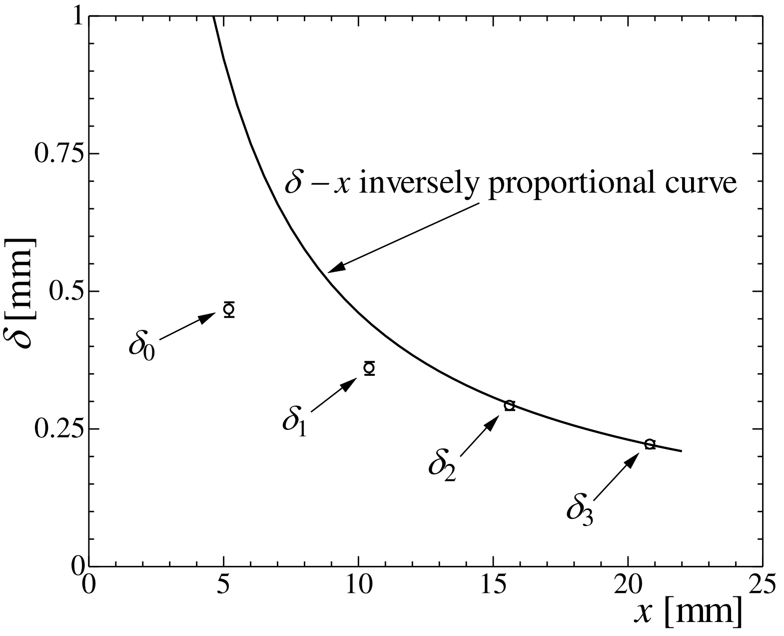

Fig. 5.6 Measured width at various circumferential distances (W=1 mm, $V_t = 0.833 \mathrm{m/s}$).

### 5.2.1.2 Boundary layer type flow

As well known, a boundary layer is developed along the wall, and a shear layer is developed between two streams of different velocities. Also, it is known that a potential flow is formed in such an axisymmetric flow field. Thus, it is reasonable to expect that the flow inside the burner consists of two types.

One is the boundary layer type flow along the wall or the shear flow between two streams [102], which situates around the periphery of the burner. The width may be dependent on the injection velocity in a form that

$$\delta \propto \sqrt{\frac{\nu x}{V_\mathrm{t}}} \quad , \qquad (5.1)$$

in which $\nu$ is a kinematic viscosity, $x$ is the distance from the starting point.

First, we examine the width $\delta_0$ by varying the injection velocity $V_\mathrm{t}$. Figure 5.7 shows the results, in which $\delta_0$ is plotted against $1/\sqrt{V_\mathrm{t}}$. It is seen that $\delta_0$ is proportional to $1/\sqrt{V_\mathrm{t}}$ very accurately. This means that the flow around the slit is dominated by a boundary layer type flow. In this figure, $\delta_2$ is also shown, which indicates that $\delta_2$ does not follow the relation of Eq. (5.1). Therefore, the flow a little bit away from the wall seems to belong to the other type of flow.

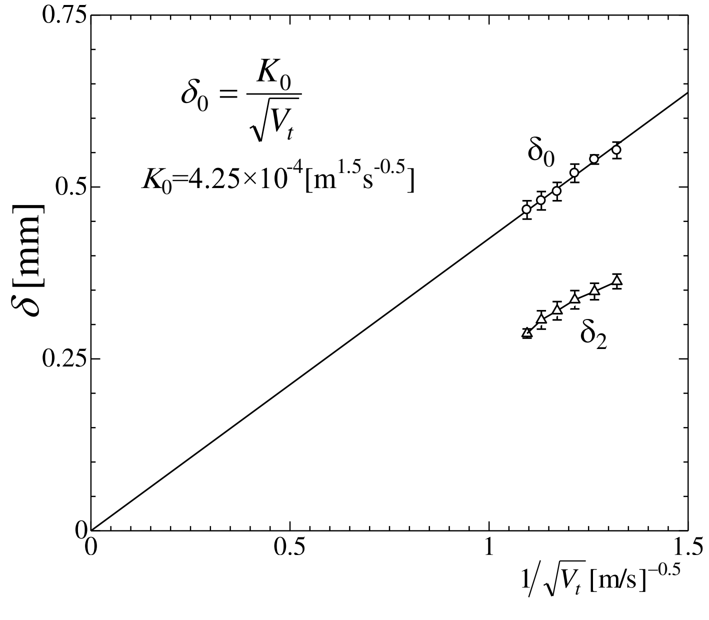

Fig. 5.7 Mixing layer thickness in the boundary layer type flow.

### 5.2.1.3 Axisymmetric type flow

The other is an axisymmetric stretched flow which occupies the center area of the burner. This flow has a stream function of the form that

$$\Psi = ar^2 Z, \tag{5.2}$$

in which $a$ is a velocity gradient, $r$ and $Z$ are the radial and axial distances from the origin (stagnation), respectively [44].

Next, we examine the width $\delta_2$ also by varying the injection velocity $V_{\mathrm{t}}$. As for the axisymmetric stretched flow, there exists a stream function of the form of Eq. 5.2). If we denote the outer and inner stream lines of the flow injected from the upper right slit as $\Psi_{\mathrm{o}}$ and $\Psi_i$, respectively, the following relation can be derived,

$$\Psi_{\mathrm{o}} - \Psi_{\mathrm{i}} = a{r_{\mathrm{o}}}^2 Z - a{r_{\mathrm{i}}}^2 Z = a(r_{\mathrm{o}} + r_{\mathrm{i}})(r_{\mathrm{o}} - r_{\mathrm{i}})Z, \tag{5.3}$$

in which $r_{\mathrm{o}}$ and $r_i$ are the outer and inner radii, respectively.

It should be noted that the value of $\Psi_0 - \Psi_{\mathrm{i}}$ corresponds to the flow rate between the two stream lines and $(r_0 + r_{\mathrm{i}}) = 2\bar{r}$ is an average diameter, while $(r_0 - r_{\mathrm{i}})$ corresponds to the width $\delta$ of this stream. If a stream tube of constant flow rate is focused, the width $\delta$ of this stream tube becomes almost inversely proportional to the axial distance $Z$. In the case of present rotating flow, the axial distance is proportional to the circumferential distance $x$, and hence, the following relation can be obtained.

$$\delta = r_\mathrm{o} - r_\mathrm{i} = \frac{\Psi_\mathrm{o} - \Psi_\mathrm{i}}{2a\bar{r}Z} \propto \frac{1}{x} \tag{5.4}$$

Namely, the width $\delta$ becomes almost inversely proportional to the circumferential distance $x$ through Eq. (5.4).

Figure 5.8 shows the variation of $\delta_2$ with $V_\mathrm{t}$, in which $\delta_2$ is plotted against $1/V_\mathrm{t}$. Owing to different axial positions, measurements of $\delta_2$ made from the front view show small deviation, however, it is seen that $\delta_2$ is almost proportional to $1/V_\mathrm{t}$, i.e., $\delta_2$ is almost inversely proportional to $V_\mathrm{t}$. This means that the flow inside is dominated by an axisymmetric stretched flow field. In this figure, $\delta_0$ is also shown, which indicates that $\delta_0$ does not follow the relation of the axisymmetric stretched flow.

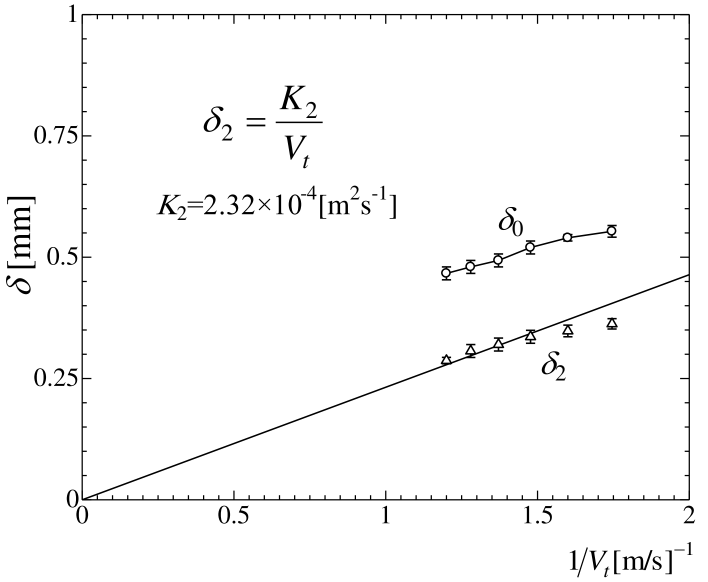

Fig. 5.8 Mixing layer thickness in the axisymmetric flow.

From the analyses, it is confirmed that there exist two types of flows in this burner.

One is the boundary layer type flow near the slit exit, and the other is an axisymmetric stretched type flow, the stream function of which is given in a form of $\Psi = ar^2 Z$ .

For the boundary layer type flow, the mixing layer thickness could be calculated from the following equation,

$$\delta_{\mathrm{m}} = \delta_0 = K_0 \Big/ \sqrt{V_{\mathrm{t}}} \tag{5.5}$$

in which $K_0 = 4.25 \times 10^{-4} [\mathrm{m}^{1.5}\mathrm{s}^{-0.5}]$ according to the results of Fig. 5.7. While, for the axisymmetric stretched flow field, the mixing layer thickness could be obtained by

$$\delta_{\mathrm{m}} = \delta_2 = K_2 / V_{\mathrm{t}} \tag{5.6}$$

in which $K_2 = 2.32 \times 10^{-4} [\mathrm{m}^2\mathrm{s}^{-1}]$ according to the results of Fig. 5.8.

### 5.2.2 Increased flow rate

In previous section (5.2.1), the mixing process in the burner of W=1 mm is investigated under much lower injection velocities. It proposes that two types of flows coexist and the mixing layer thicknesses have some relationships with injection velocity. To substantiate these results, in this section, on one hand the injection velocities are increased up to 0.079 $\mathrm{m}^3_{\mathrm{N}}$/h, on the other hand, the mixing process in the burners of W=3,2 and 1 mm are investigated, respectively.

#### 5.2.2.1 Flow visualization

At the injection flow rate of 0.069 $m^3{}_N/h$, Fig. 5.9 shows the flow visualization inside the three optically accessible burners W=3, 2 and 1 mm, respectively. The seeded and non-seeded flows are both dry air flows. The other conditions remain the same as that in section of 5.2.1.

It is seen that the flow visualizations as those of Q=0.048 $m^3{}_N/h$ (for W=1 mm, $V_t$=0.833m/s) could be obtained, however, due to difficulty of capture the particles under increased of injection velocity, especially for W=1 mm ($V_t$ =1.198 m/s), the quality of the image reduces.

In the case of W= 3 and 2 mm, it is seen in Fig. 5.9(a ) and (b) that the seeded flows from the lower right slits abruptly shrink in width after the flow are injected from the slits through the interactions with the non-seeded flow from the upper right slits. In the case of W=1 mm, it is seen in Fig. 5.9c that the seeded flow from the lower right slit once slightly expands in width when the flow is just injected outside from the slit, however, the flow shrinks thereafter and the width gradually decreases.

For these three cases, the non-seeded flows from the upper right slits also shrink and their widths, indicated by red arrows, decrease. To quantify the decrease in the width, with the same methods, we define the starting point and also $\delta_0$, $\delta_1$, $\delta_2$ and $\delta_3$, as shown by the red arrows in Fig. 5.9a.

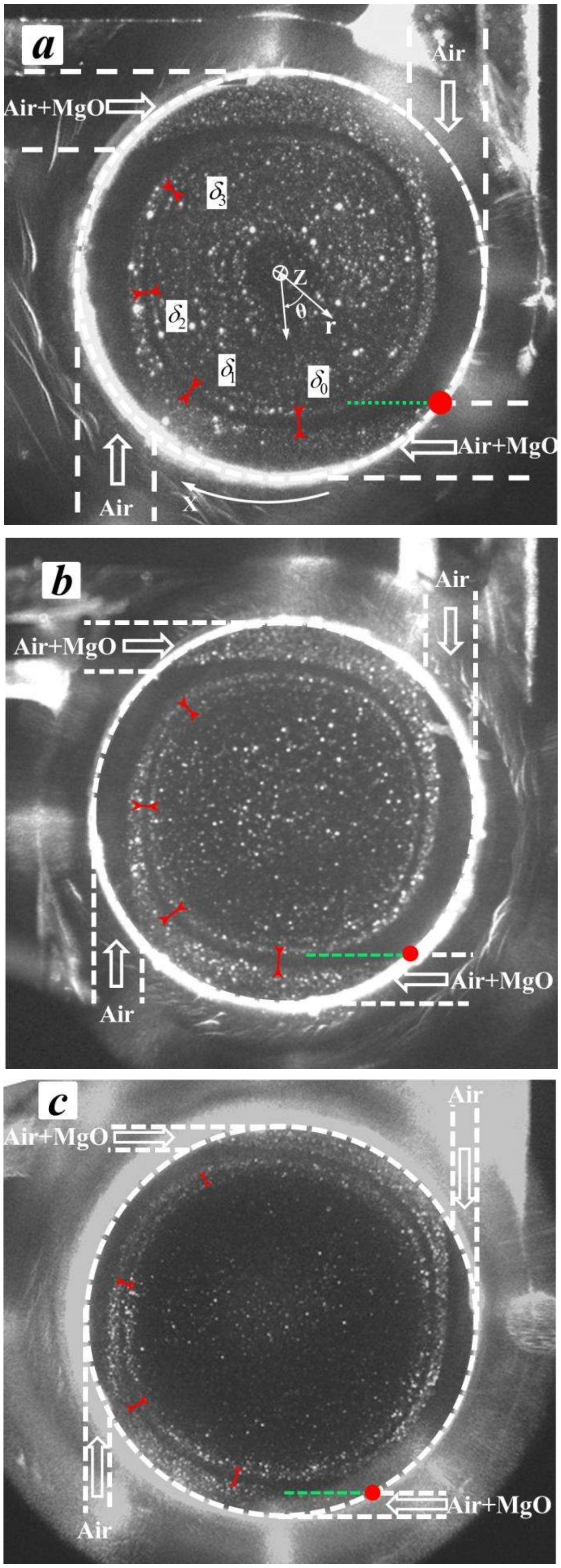

Fig. 5.9 Flow visualization ( $Q = 0.069\ \mathrm{m^3/h}$ , a: W= 3 mm, b: W= 2 mm, c: W= 1 mm).

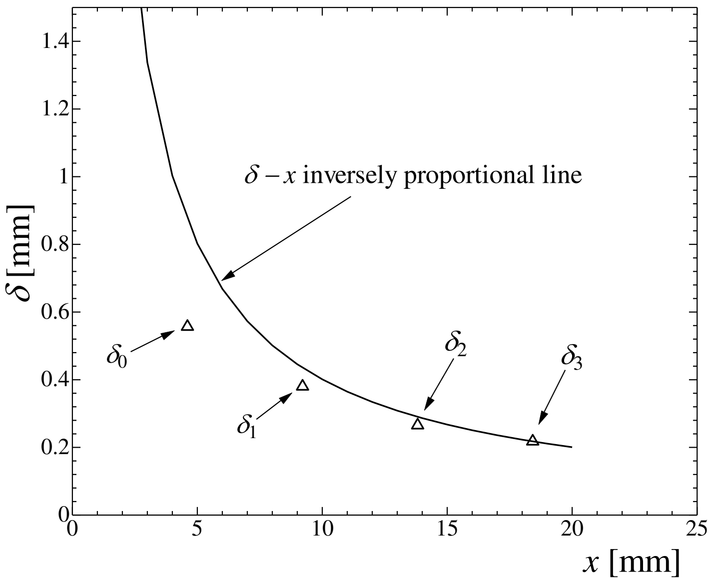

Fig. 5.10 Measured width at various circumferential distances (W=3 mm, $Q_{Air}$= 0.069 $m^3{}_N$/h).

The values of $\delta_0$, $\delta_1$, $\delta_2$ and $\delta_3$, measured at a condition of injection flow rate $Q_{Air}$= 0.069 $m^3{}_N$/h with the 3 mm slit width burner, are shown in Fig. 5.10. It is also found that $\delta_2$ and $\delta_3$ are almost inversely proportional to each other, whereas $\delta_0$ and $\delta_1$ show quite different tendency from $\delta_2$ and $\delta_3$. This suggests that different types of flows coexist in the burner of W=3 mm, as those of W=1 mm. Thus, we can further expand our conclusion that the boundary layer type flow and axisymmetric flow coexist in the rapidly mixed type tubular flame burner with such a configuration. In the following, the boundary type flows and the axisymmetric flows in three types of burners are examined, respectively.

#### 5.2.2.2 W=3mm

The width $\delta_0$ is examined by varying the injection velocity $V_t$, as shown in Fig.

5.11. It is seen that $\delta_0$ is proportional to $1/\sqrt{V_\mathrm{t}}$ with a coefficient of $K_0 = 3.51\times10^{-4}[\mathrm{m}^{1.5}\mathrm{s}^{-0.5}]$. This means that the flow around the slit is dominated by a boundary layer type flow. In Fig. 5.12, $\delta_2$ is plot against $1/V_\mathrm{t}$ , which indicates that $\delta_2$ is proportional to $1/V_\mathrm{t}$. This illustrates that the flow inside is dominated by an axisymmetric stretched flow field.

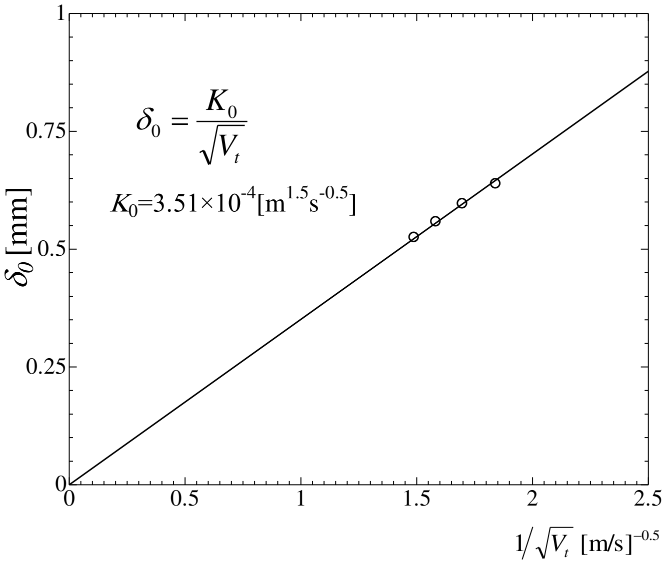

Fig. 5.11 Mixing layer thickness in the boundary layer type flow (W= 3 mm).

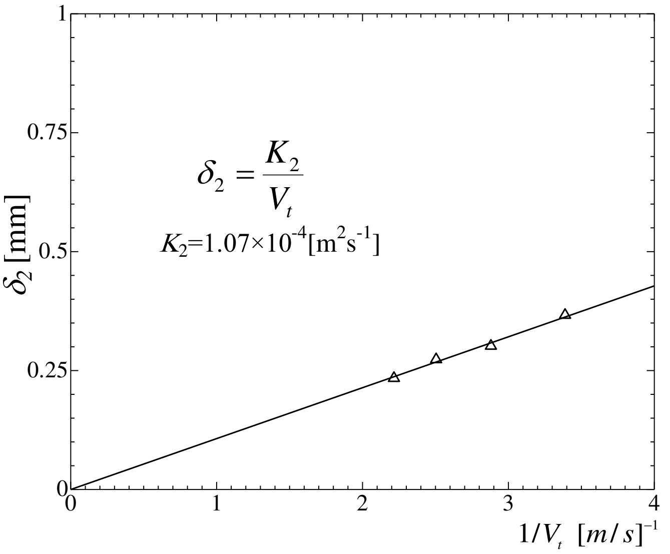

Fig. 5.12 Mixing layer thickness in the axisymmetric flow (W= 3 mm).

### 5.2.2.3 W=2mm

Under the same flow rates, for W= 2 mm the width $\delta_0$ and $\delta_2$ are examined by varying the injection velocities $V_t$, as shown in Figs. 5.13 and 5.14. It is seen that $\delta_0$ is proportional to $1/\sqrt{V_t}$ with a coefficient of $K_0 = 4.03\times10^{-4}[\mathrm{m}^{1.5}\mathrm{s}^{-0.5}]$. While $\delta_2$ is proportional to $1/V_t$ with a coefficient of $K_2 = 1.52\times10^{-4}[\mathrm{m}^2\mathrm{s}^{-1}]$.

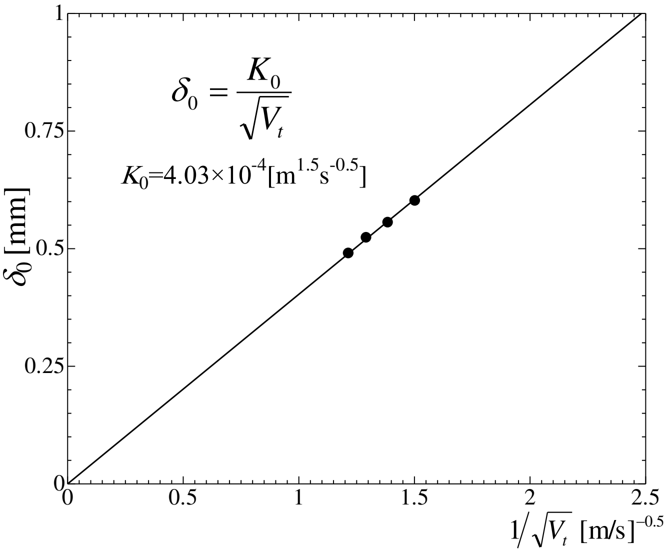

Fig. 5.13 Mixing layer thickness in the boundary layer type flow (W= 2 mm).

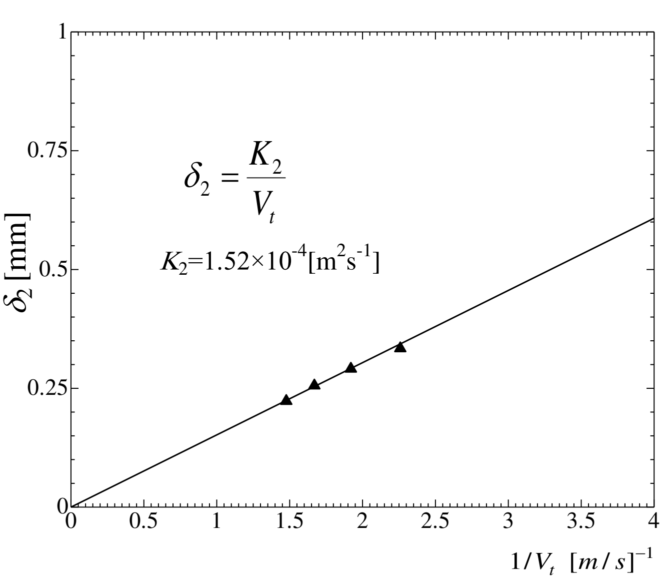

Fig. 5.14 Mixing layer thickness in the axisymmetric flow (W= 2 mm).

### 5.2.2.4 W=1mm

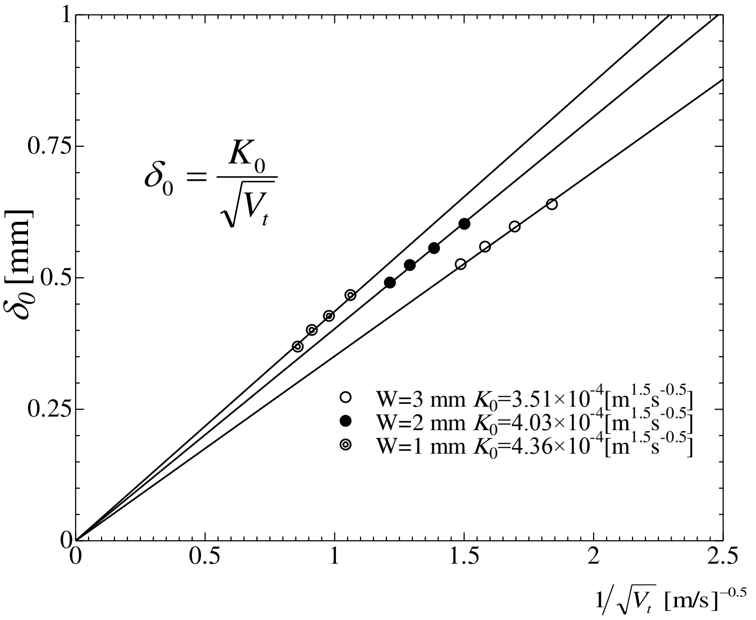

Fig. 5.15 Mixing layer thickness in the boundary layer type flow (W= 3, 2 and 1mm).

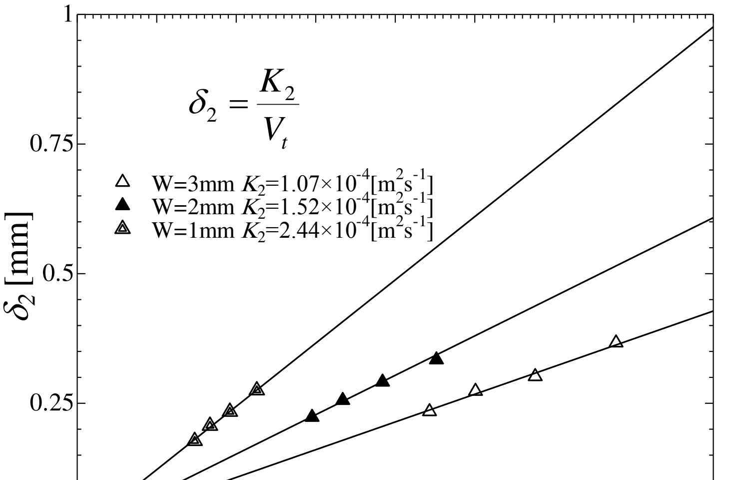

Fig. 5.16 Mixing layer thickness in the axisymmetric flow (W=3, 2 and 1 mm).

For W=1 mm, as shown in Figs. 5.15, $\delta_0$ is proportional to $1/\sqrt{V_t}$ with a coefficient of $K_0 = 4.36\times10^{-4}[\mathrm{m}^{1.5}\mathrm{s}^{-0.5}]$, which is almost equal to the coefficient obtained in section 5.2.1 ($K_0 = 4.25 \times 10^{-4}[\mathrm{m}^{1.5}\mathrm{s}^{-0.5}]$) within 2.59%. Figure 5.16 shows the accurate proportional relation between $\delta_2$ and $1/V_\mathrm{t}$. The coefficient is $K_2 = 2.44 \times 10^{-4}[\mathrm{m}^2\mathrm{s}^{-1}]$ which agrees with the value obtained under lower injection velocity ($K_2 = 2.32 \times 10^{-4}[\mathrm{m}^2\mathrm{s}^{-1}]$) within 5.17%. In Figs. 5.15 and 5.16, the relations in W= 3 and 2 mm are also shown. For the same injection velocity, where the flow rate of W= 1 mm is 1/2 or 1/3 of that in the W= 2 and 3 mm, respectively, due to the effect of stretch rate especially for 3 mm, the coefficients for W= 3 mm are the smallest.

### 5.2.2.5 Summary and comparison

In this section, the flow rate is increased up to 0.079 $\mathrm{m}^3_\mathrm{N}$/h and the mixing processes in three burners are examined respectively. The results confirm two types of flow: the boundary layer type flow and the axisymmetric flow, which dominate the region close to the injection slit and the center area downstream the slits, respectively. The mixing layer thickness in the boundary layer type flow is proportion to $1/\sqrt{V_\mathrm{t}}$, while the mixing layer thickness in the axisymmetric flow is proportional to $1/V_\mathrm{t}$. The concrete values of the coefficients are obtained by changing the injection velocities.

The injection velocity is proportion to the flow rate. And the measurements are made under the same flow rates for the three burners. For systematical analysis, the measured width $\delta_0$ and $\delta_2$ are examined by varying the flow rate. Figure 5.17 shows that the mixing layer thicknesses are in proportion to $1/\sqrt{Q}$ for the boundary layer type flow. The coefficient for W= 3 mm is the largest and slightly decreases for W= 2 mm; while that for W= 1 mm is relatively smaller. Since the flow visualizations for W=3 and 2 mm are close to each but different with W= 1 mm. The other factor is the

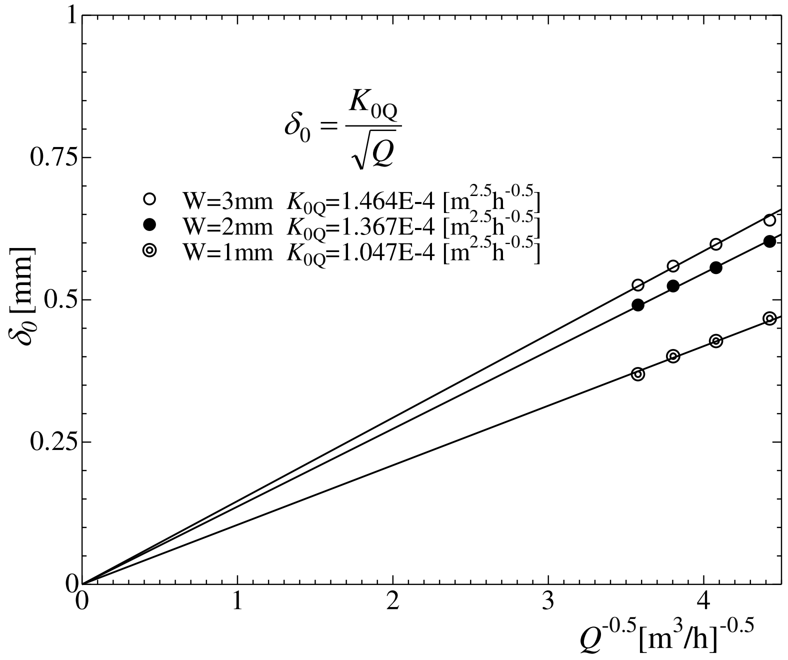

Fig. 5.17 Mixing layer thickness varying with flow rate in the boundary layer type flow.

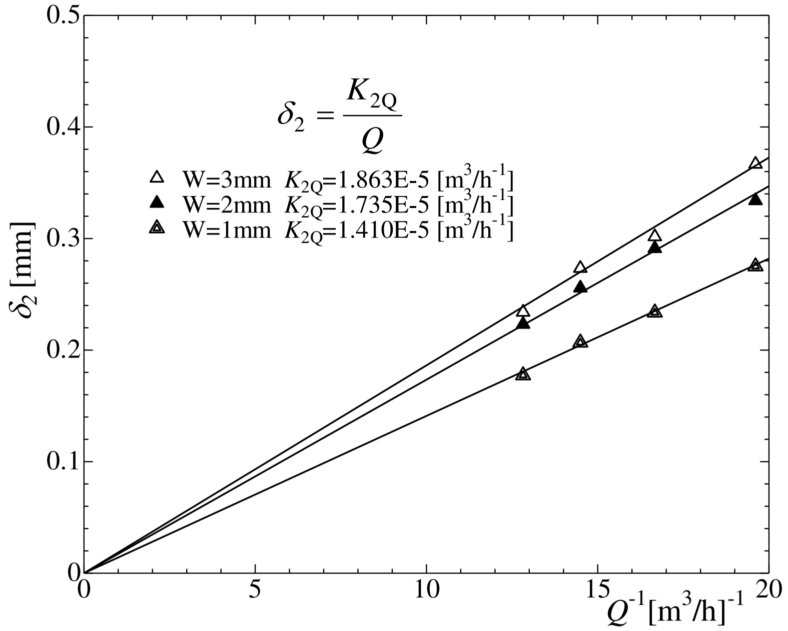

Fig. 5.18 Mixing layer thickness varying with flow rate in the axisymmetric flow.

injection velocity, which is smallest in W= 3 mm while largest in W= 1 mm.

Figure 5.18 shows the proportional relation between the mixing layer thickness ($\delta_2$) and the inverse value of flow rate in the axisymmetric flow. The coefficients are much smaller and decrease with a decrease of slit width. The results illustrates that the mixing occurring in the axisymmetric flow (center region) runs faster than in the boundary layer type flow (close to the exits of slits). And the mixing in W=1 mm performs best among three cases.

## 5.3 Mixing layer under different injection flow rate

The mixing processes in three burners have been investigated with the flow visualizations for which the injection velocities of seeded flows and non-seeded flows are the same. In actual it is common that the injection velocities of fuel and oxidizer are different and hence the mixing may be different from the case with same injection velocity. For stoichiometric methane/oxygen condition, the flow rate of oxygen is twice as that of the methane flow rate. In this section, the mixing processes where the injection velocity of the seeded flow is a half of the non-seeded flows are investigated in three burners. The results are analyzed in detail to give a general estimation of the mixing layer thickness.

### 5.3.1 Flow visualization

For different injection velocities, two methods have been tried. With injection velocity of the seeded flow twice as that of the non-seeded flow, the flow visualization is shown in Fig. 5.19. It is seen that the upper right non-seeded flow shrinks much after injected outside the slits and its width becomes much smaller when meets the lower right seeded flow. The mixing layer thickness is hard to measure under such condition. The other method is set the injection velocity of the seeded flow smaller than that of the non-seeded flow, say, a half, which will be discussed in the following.

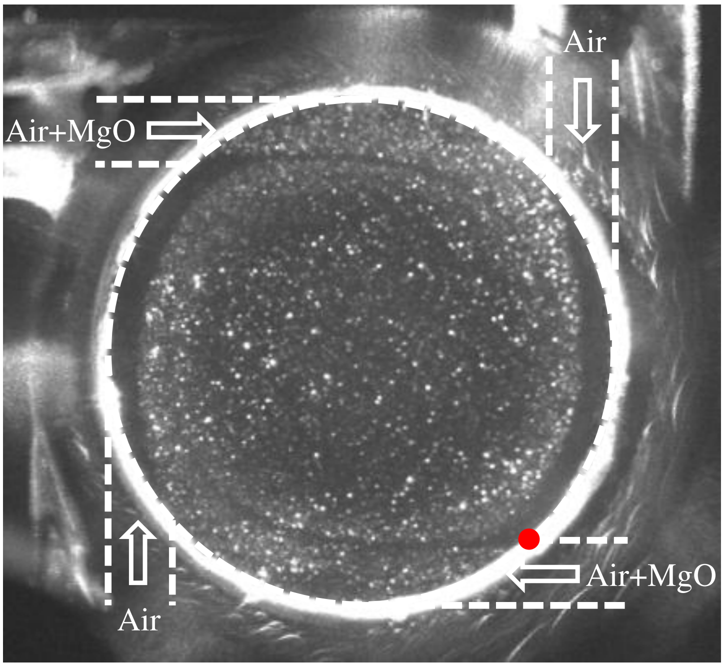

Fig. 5.19 Flow visualization for injection velocity of seeded flow ($Q_s$ =0.069 $m^3_N$/h) twice as that of the non-seeded flow ($Q_{nons}$ =0.0345 $m^3_N$/h), W=2 mm.

### 5.3.1.1 W=3mm

At the injection flow rates of $Q_s$ =0.0345 $m^3_N$/h for seeded flow and $Q_{nons}$ = 0.069 $m^3_N$/h for non-seeded flow, Fig. 5.20 shows the flow visualization inside the optically accessible burner W=3mm. The measured position is the same as previous measurements.

Comparing with the case of same injection velocity, the seeded flow from upper left shrinks much once meets the non-seeded flow from the upper right. The width of the non-seeded flow from upper right slit is almost twice as that of the seeded flow from the upper left and then decreases as the flow goes around (denoted by the red arrows).

In current study we focus on the mixing near the injection slit, i.e. as discussed previously the mixing in the boundary layer type flow. However, how to choose the mixing layer thickness, whether the boundary layer type still exists or not and which injection velocity should be used are needed to discussed firstly.

Despite the boundary type flow or the axisymmetric flow, the mixing layer thickness decreases with an increase of injection velocity. For the case of same injection velocities, the mixing layer could be measured by either of the flow. For the case of different injection velocities, the mixing layer mainly depends on the flow with lower velocity. This could also be explained in Fig. 5.20. For the higher velocity flow (non-seeded flow), the mixing means to diffuse into and even pass the seeded flow, and hence the width of the seeded flow could be considered as the mixing layer thickness for the non-seeded flow; while for the lower velocity flow (seeded flow), the mixing means to diffuse into the non-seeded flow. The width of the non-seeded flow

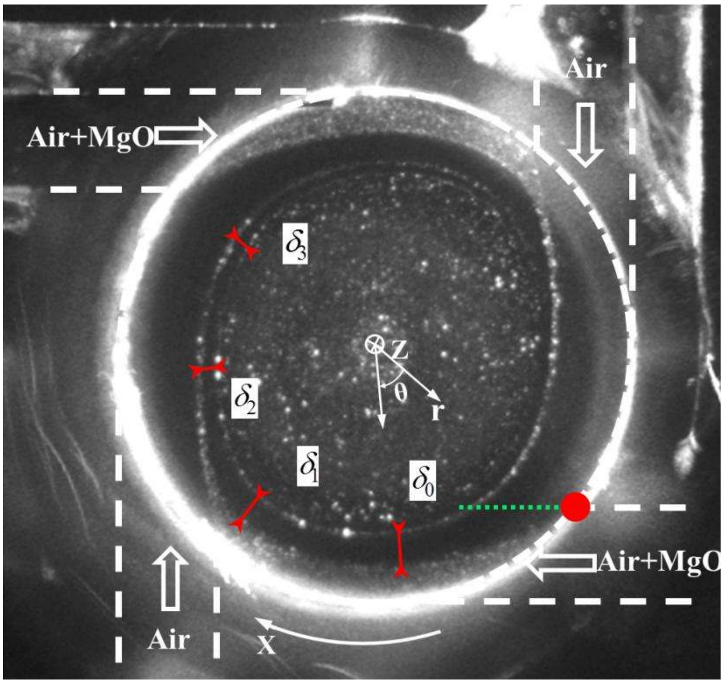

Fig. 5.20 Flow visualization under different injection flow rate ($Q_{nons}$=0.069 $m^3{}_N$/h, $Q_s$=0.0345 $m^3{}_N$/h, W= 3 mm).

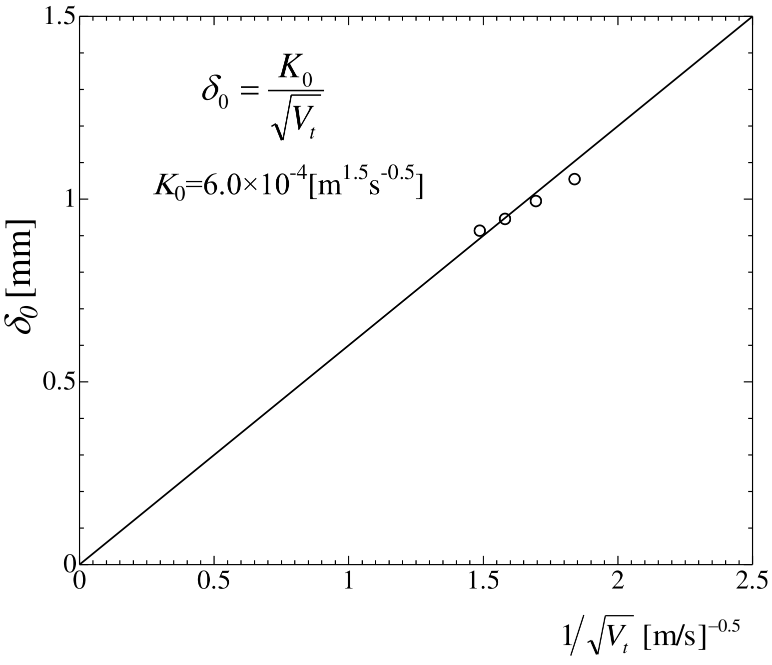

Fig. 5.21 Mixing layer thickness in the boundary layer type flow (W= 3 mm).

could be considered as the mixing layer thickness. It is seen in Fig. 5.20 that after injected outside the slit the width of the non-seeded flow is always larger than that of the seeded flow, hence rate determining process. Therefore, it is reasonable to choose $\delta_0$ (the width of non-seeded flow). And the width of the non-seeded flow is dependent on the flow rate hence the injection velocity of the non-seeded flow.

In Fig. 5.21, $\delta_0$ is plot against $1/\sqrt{V_t}$ . There is a proportion between them and the coefficient is 6.0E-4 m$^{1.5}$s$^{-0.5}$ which is slightly larger than that of the same injection velocity. The results means that the boundary layer type flow still dominant the flow close to the injection slits and if reduces the injection velocity of one flow the mixing layer thickness increases.

### 5.3.1.2 W=2mm

Figure 5.22 shows the flow visualization inside the optically accessible burner W=2 mm. And $\delta_0$ is plot against $1/\sqrt{V_t}$ in Fig. 5.23 which shows the proportional relationship between $\delta_0$ and $1/\sqrt{V_t}$ . The coefficient is 6.19E-4 $m^{1.5}s^{-0.5}$ which is a bit larger than that of the same injection velocity in W=2 mm.

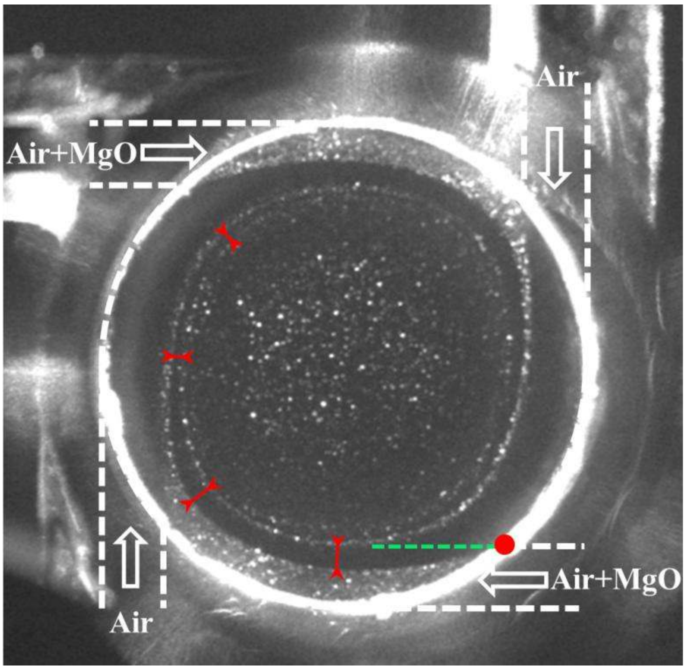

Fig. 5.22 Flow visualization under different injection flow rate ($Q_{un}$=0.069 $m^3{}_N$/h, $Q_s$=0.0345 $m^3{}_N$/h, W= 2 mm).

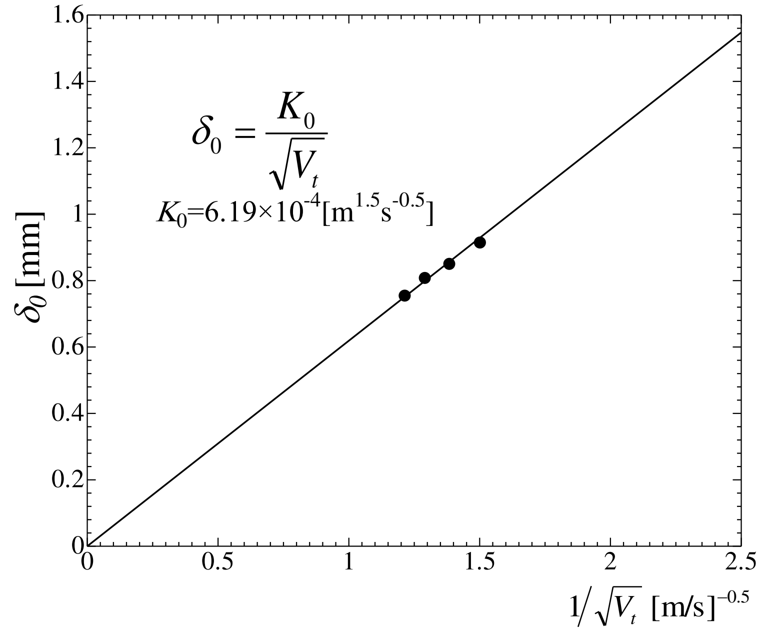

Fig. 5.23 Mixing layer thickness in the boundary layer type flow (W= 2 mm).

### 5.3.1.3 W=1mm

Figure 5.24 shows the flow visualization in the optically accessible burner of W=1mm. The non-seeded flow from the upper right slit becomes hard to measure when it flows downstream the lower left non-seeded flow. Figure 5.25 shows the proportional relation of $\delta_0$ and $1/\sqrt{V_t}$ . The coefficient is 5.99E-4 m$^{1.5}$s$^{-0.5}$ which is much close to those of in W=3 and 2 mm.

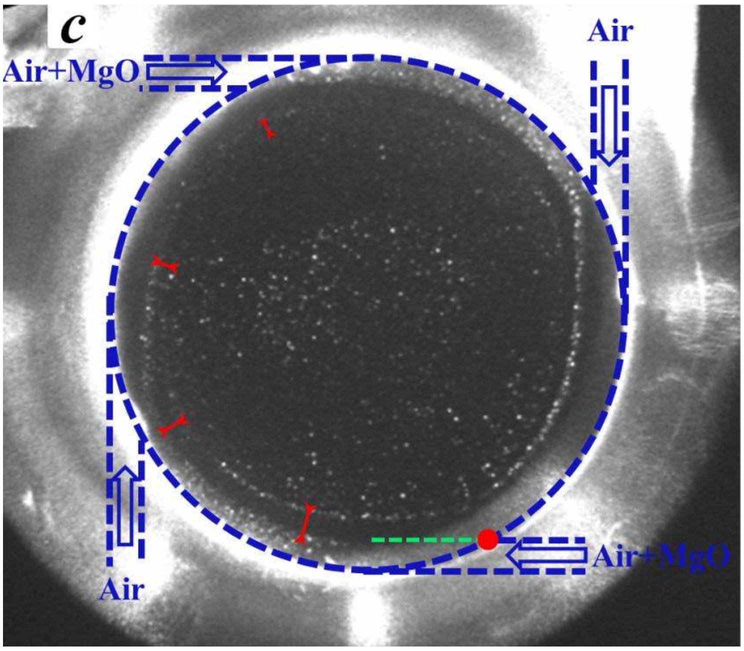

Fig. 5.24 Flow visualization under different injection flow rate ($Q_{un}$=0.069 $m^3_N$/h, $Q_s$=0.0345 $m^3_N$/h, W= 1 mm).

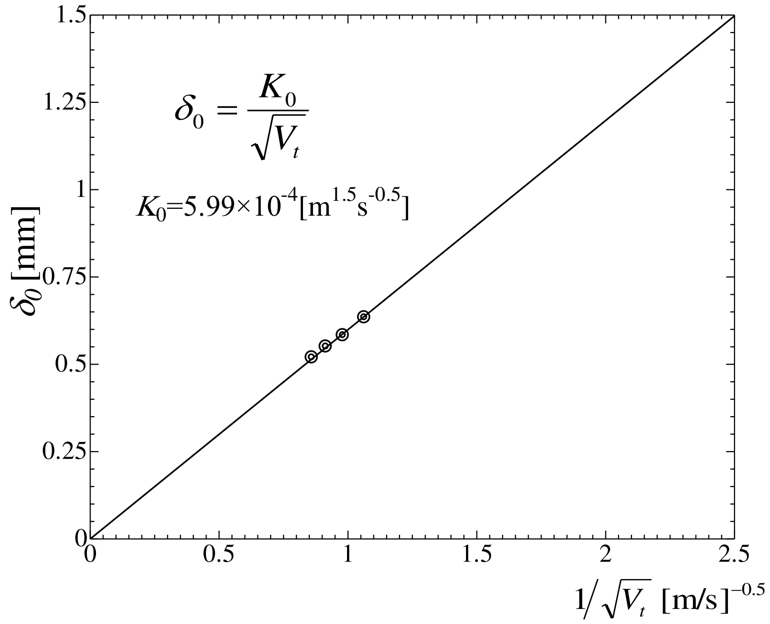

Fig. 5.25 Mixing layer thickness in the boundary layer type flow (W= 1 mm).

### 5.3.2 Analysis

#### 5.3.2.1 Coefficients of the boundary layer type flow

In the boundary layer type flow, the mixing layer thickness under the same flow rate and that with one flow rate twice as the other could be estimated by measured coefficient through Eq. (5.5). For other conditions, it is hard to measure all the coefficients through experiments. Based on the measured coefficients, we try to deduce a general relation to estimate the mixing layer thickness under various flow rates of fuel and oxidizer.

Here take the mixing layer thickness in the boundary layer type flow in the burner of W=1 mm as an example. For the case that seeded flow rate is half of the non-seeded flow, the injection velocity of the seeded flow ($V_{\mathrm{t\text{-}s}}$) is half as that of the non-seeded flow ($V_{\mathrm{t\text{-}non}}$). The mixing layer thickness could be estimated by two ways. One is based on the measured coefficient of different injection velocities obtained in 5.3.1.3 and the injection velocity of the non-seed flow (higher velocity). Thus the mixing layer thickness ($\delta_0$) could be given by the following relation that,

$$\delta_{\mathrm{m}} = \delta_0 = \frac{K_0}{\sqrt{V_{\mathrm{t-non}}}} = \frac{5.99\times10^{-4}}{\sqrt{V_{\mathrm{t-non}}}} = \frac{5.99\times10^{-4}}{\sqrt{2\times V_{\mathrm{t-s}}}} = \frac{4.236\times10^{-4}}{\sqrt{V_{\mathrm{t-s}}}} \tag{5.7}$$

The other is based on the measured coefficient under the same injection velocities obtained in 5.2.1, however, we assume the mixing occurs under the lower injection velocities ($V_{\mathrm{t\text{-}s}}$). Thus, $\delta_0$ could be given by Eq. (5.8),

$$\delta_{\mathrm{m}} = \delta_0 = \frac{K_0}{\sqrt{V_{\mathrm{t-s}}}} = \frac{4.25 \times 10^{-4}}{\sqrt{V_{\mathrm{t-s}}}} \tag{5.8}$$

Comparing these two methods, the mixing layer thickness obtained by Eq. (5.7) is 99.67% as that obtained by Eq. (5.8). The results are almost the same. Though it needs to be further approved, based on the analysis we make an assumption that the mixing layer thickness ($\delta_0$) of different injection velocity could be estimated by Eq. (5.8), in which $V_{t\text{-}s}$ stands for the lower injection velocity.

The same analyses are made for W = 2 and 3 mm. For W= 2 mm, the following two relations are obtained,

$$\delta_{\mathrm{m}} = \delta_0 = \frac{K_0}{\sqrt{V_{\mathrm{t-non}}}} = \frac{6.19 \times 10^{-4}}{\sqrt{V_{\mathrm{t-non}}}} = \frac{6.19 \times 10^{-4}}{\sqrt{2 \times V_{\mathrm{t-s}}}} = \frac{4.37 \times 10^{-4}}{\sqrt{V_{\mathrm{t-s}}}} \tag{5.9}$$

$$\delta_{\mathrm{m}} = \delta_0 = \frac{K_0}{\sqrt{V_{\mathrm{t-s}}}} = \frac{4.03 \times 10^{-4}}{\sqrt{V_{\mathrm{t-s}}}} \tag{5.10}$$

The mixing layer thickness obtained by Eq. (5.9) is 108.44% as that obtained by Eq. (5.10), which is within 10%. We still can roughly estimate the mixing layer thickness of different velocity ratio through Eq. (5.10).

For W=3 mm, the following two relations are obtained,

$$\delta_{\mathrm{m}} = \delta_0 = \frac{K_0}{\sqrt{V_{\mathrm{t-non}}}} = \frac{6.00 \times 10^{-4}}{\sqrt{V_{\mathrm{t-non}}}} = \frac{6.00 \times 10^{-4}}{\sqrt{2 \times V_{\mathrm{t-s}}}} = \frac{4.24 \times 10^{-4}}{\sqrt{V_{\mathrm{t-s}}}} \tag{5.11}$$

$$\delta_{\mathrm{m}} = \delta_0 = \frac{K_0}{\sqrt{V_{\mathrm{t-s}}}} = \frac{3.51 \times 10^{-4}}{\sqrt{V_{\mathrm{t-s}}}} \tag{5.12}$$

The mixing layer thickness obtained by Eq. (5.11) is 120.88% as that obtained by Eq. (5.12). For this case, using the Eq. (5.12) to estimate the mixing layer thickness may cause big deviation and the coefficients of various injection velocity ratios should be obtained through experimental measurements.

#### 5.3.2.2 Validity for applying to combustion tests

The mixing layer is so thin in practice that the measurements are made at low injection velocities. However, the boundary layer type thickness, which depends on the inverse square root of the approach velocity such as Eq. (5.5), can be hold as long as the laminar condition is maintained. The Reynolds numbers, defined as $V_t W/\nu$, at the low injection velocities for the thickness measurements were the order of 200, while those at actual combustion tests were the order of $2.0\times10^4$. According to a textbook by Schlichting, H. [112], the boundary layer thickness which is defined by Eq. (5.13), could be valid until the Reynolds number reaches $3.2\times10^5$, as shown in Fig. 5.26.

$$\delta = 5.0\sqrt{\frac{\nu \cdot x}{U_\infty}} \tag{5.13}$$

in which $\nu$ is viscosity, $x$ is the distance and $U_\infty$ is approach velocity. Eq. (5.13) has the same form as the boundary layer thickness in current study. Thus, it can be considered that Eqs. (5.5) and (5.7~ 5.12) are still valid for high injection velocities at the actual combustion tests.

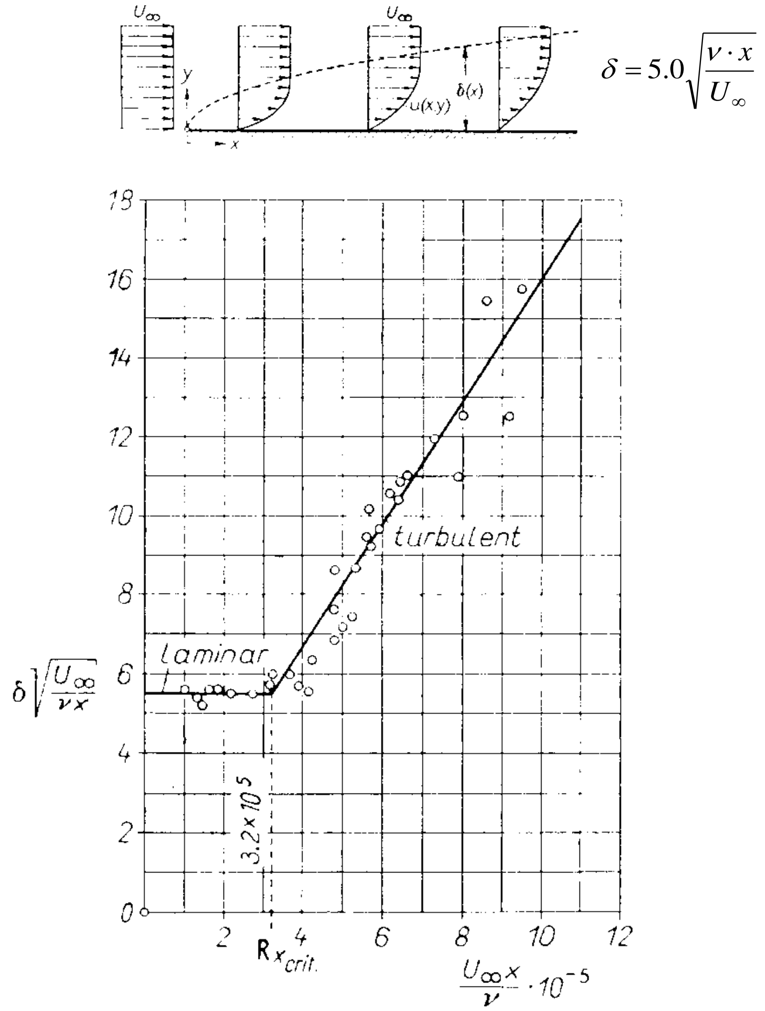

Fig. 5.26 The boundary layer thickness (upper) and the coefficient varying with Reynolds number (lower) [112].

Once ignited, the flow field inside the flame is changed due to high temperature and low density. However, the unburned cold flows outside the flame may not be significantly disturbed especially in the circumferential direction. As shown in Fig. 5.27, Shimokuri et al. [113] measured the circumferential velocity in a 2-inch tubular flame burner. It is seen that outside the flame front, the circumferential velocity of cold flow is much close to that of the combustion condition. Thus, it is reasonable to expect that Eqs. (5.5) and (5.7~ 5.12) are still valid for actual combustion tests.

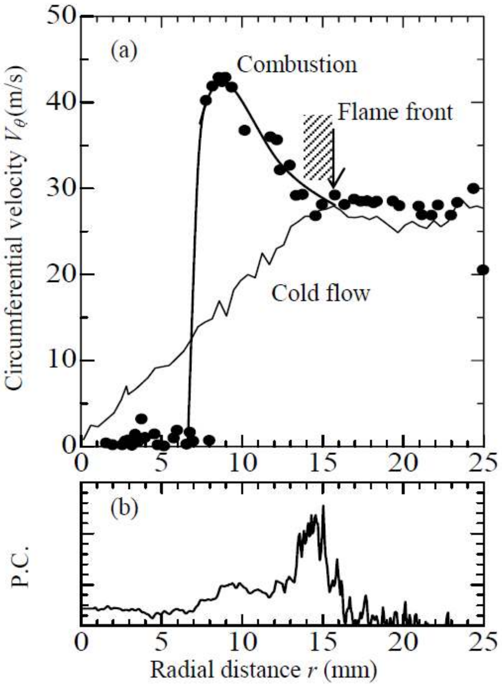

Fig. 5.27 Radial distributions of circumferential velocity $V_\theta$ of combustion flow (Upper: velocity, Lower: chemi-luminescent) [113].

## 5.4 Mixing time

Based on these two mixing layer thicknesses, the mixing time can be estimated through Eq. (5.14). Due to different injection velocities, hence different mixing layer thicknesses of methane and oxygen, as discussed in 5.3.2, for W=2 and 1 mm, the boundary layer thickness could be the calculated with lower injection velocity. Under very lean condition, due to lower injection velocity of fuel, the mixing layer thickness of methane becomes thicker, resulting in the rate determining process. Thus, the mixing layer thickness of methane should be taken to calculate the mixing time.

$$\tau_{\mathrm{m}} = \frac{\delta_{\mathrm{CH_4}} \delta_{\mathrm{CH_4}}}{D_{\mathrm{CH_4 - O_2}}}, \tag{5.14}$$

in which $\delta_{\mathrm{CH_4}}$ are the mixing layer thicknesses for methane flow, and $D_{\mathrm{CH_4-O_2}}$ is mass diffusivity of methane/oxygen mixture and here $D_{\mathrm{CH_4-O_2}} = 0.23\ \mathrm{cm^2/s}$ is adopted.

Based on above analysis, the mixing time has been calculated through Eq. (5.5) and Eq. (5.14). The results are plotted against the equivalence ratio in Fig. 5.28, where the oxidizer flow rate and oxygen mole fraction have given. Comparing with the decreasing trend of reaction time in Fig. 4.22, the decrease of mixing time is much slow. For the same oxidizer flow rate (10 $\mathrm{m^3_N/h}$), at the same equivalence ratio the mixing time of pure oxygen is smaller than that of $\beta$ =0.684. If decreases the oxidizer flow rate, then the mixing time increases.

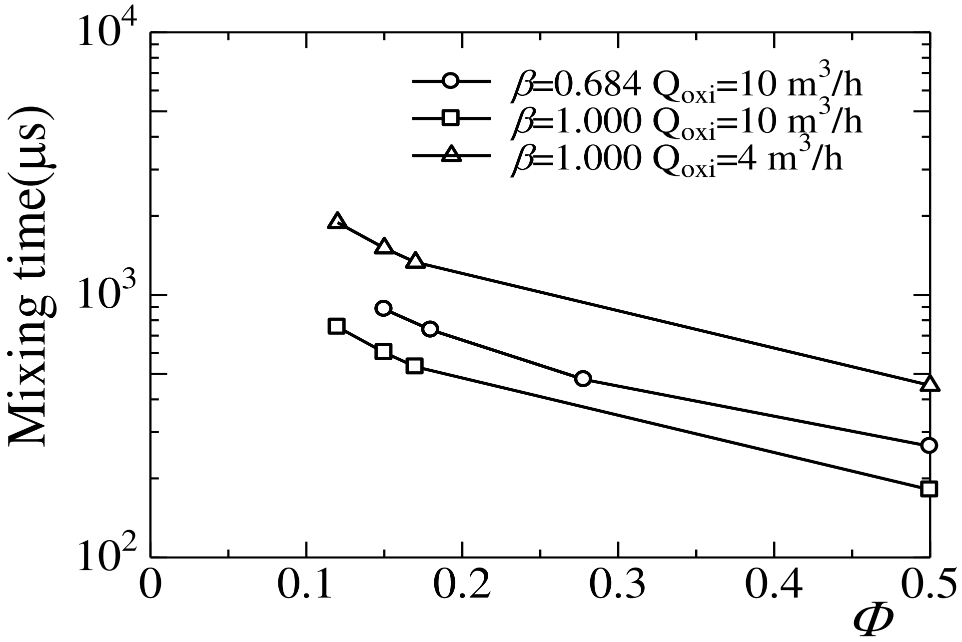

Fig. 5.28 Variation of mixing time with equivalence ratio at given oxidizer flow rate (W=1 mm, $Q_{oxi}$= 10, 4 $m^3_N$/h).

## 5.5 Summary

To quantify the mixing process in the rapidly mixed tubular flame combustion, the flow field is visualized by a PIV system. With three quartz burners of different slit widths, the mixing layer thicknesses are examined under the same and different flow rates of the seeded flow and non-seeded flow. The following are concrete conclusions:

(1) There exist two types of flows, a boundary layer type flow near the exits of the slits close to the wall, and an axisymmetric potential flow around the axis of rotation;

(2) The mixing layer thickness in the boundary layer type flow is proportional to the inverse square root of injection velocity; while for the axisymmetric flow, the thickness is in proportion to the inverse value of injection velocity. The coefficients of both type flows are discussed in three types of burners, respectively.

(3) For the mixing layer with injection velocity of seeded flow half of that the non-seeded flow, the thicknesses in boundary layer type flow are examined. For W=2 and 1 mm, the mixing thickness could also be roughly calculated by the coefficients obtained under the same injection velocity using the lower injection velocity (seeded flow). And this is further assumed to estimate the mixing layer thickness under various injection velocity ratios in W=2 and 1 mm.

(4) Mixing time can be calculated by the mixing layer thickness of the flow with lower injection velocity.

# Chapter 6 Discussion on the Requirement for Rapidly Mixed Oxygen Enhanced Tubular Flame Combustion

## 6.1 Introduction

In this chapter the requirement for establishment of rapidly mixed oxygen enhanced tubular flame combustion will be discussed. For conventional fuel/air rapidly mixed tubular flame combustion, swirl numbers larger than 5 and injection velocities higher than about 20 m/s are required for stable combustion [33]. Under high oxygen mole fraction, however, diffusion flames anchored at the exits of slits interrupt the mixing of fuel and oxidizer, resulting in an oscillatory combustion. Thus, the first step is to inhibit the diffusion flame.

For combustion of high oxygen mole fraction, the reaction rate increases much hence shorter reaction time. While for rapidly mixed tubular flame combustion, before the onset of reaction, mixing of fuel and oxidizer is required to be completed, resulting in that the mixing time should be smaller than reaction time. Therefore, Damkohler number ($D_a$), defined as the ratio of mixing time to reaction time (Eq. (6.1)), is referred to quantitatively analyze the establishment of rapidly mixed oxygen enhanced tubular flame combustion.

$$D_a = \frac{\tau_m}{\tau_r}. \qquad (6.1)$$

The Damkohler number is particularly important in combustion processes, which determines a number of conditions including whether complete mixing occurs and pollution formation [114]. Koutmos [115] employed the Damkohler number to derive an extinction criterion in turbulent methane jet diffusion flames. Ghoniem and Heidarinfjad [116] investigated the effect of Damkohler number on the reactive zone structure in a shear layer. And in many other studies Damkohler number has been discussed to illustrate various combustion processes [54, 102, 116].

As an example, the Damkohler number for rapidly mixed oxygen enhanced tubular flame combustion is discussed. In Chap.4 we have calculated the reaction time and based on the experimental results in Chap.5, mixing time could be estimated, and then the Damkohler number will be obtained.

## 6.2 Inhibit diffusion flame by reducing slit width

In combustion tests, the diffusion flame has been successfully inhibited by reducing the slit width from 2 mm to 1mm. Here, with the local flow visualization, the differences between burners of W= 2 and 1 mm are discussed.

Though the inner diameter of these burners are the same, due to different widths of injection slits, hence different injection velocities under the same flow rate, the flow visualization show some differences. For W= 3 and 2 mm the flows abruptly shrink in width after injected outside the slits, while for W= 1 mm, the flow expands after injected outside the slit and then shrinks. Here the local visualizations close to the lower right seeded flow inlets are discussed under different injection velocities. As shown in Fig. 6.1(a), the flow rate is Q=0.03 $m^3_N/h$. For W= 2 mm (upper), the width

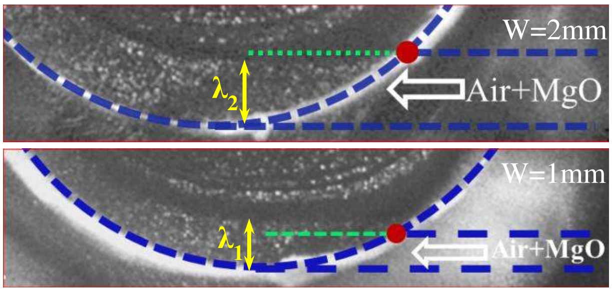

(a) Q=0.03 $m^3_N/h$

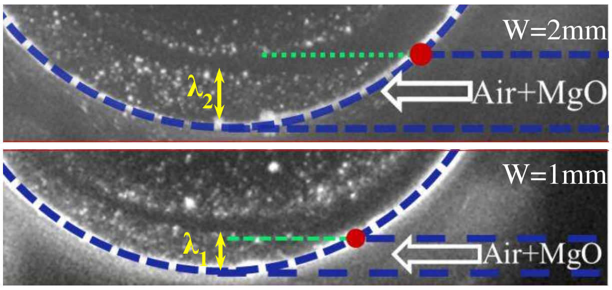

(b) Q=0.069 $m^3_N/h$

Fig. 6.1 Local flow visualization close to the seeded flow injection slit ((a) Q=0.03 $m^3_N/h$, (b) Q=0.069 $m^3_N/h$, upper: W=2 mm, lower: W=1mm).

of the seeded flow ($\lambda_2$) is smaller than the slit width (broken lines), which means the seeded flow shrinks; while for W=1mm (lower), the width of the flow ($\lambda_1$) is larger than the slit width (broken lines), which means the seeded flow expands. With an increase of flow rate (Q= 0.069 $m^3_N$/h), as shown in Fig. 6.1 (b), the widths of the flow ($\lambda_2$ and $\lambda_1$) reduces. Hence the flow in the burner of W=2 mm further shrinks; while in the burner of W=1 mm, though the flow width ($\lambda_1$) decreases it still larger than the slit width, which shows slightly expands. For the same flow rate, though the flow shrinks in the burner of W=2 mm while expands in W=1 mm, the width of the seeded flow ($\lambda_2$) in W=2 mm is larger than that of W=1 mm ($\lambda_1$). And the average injection velocity of W=2 mm is half that of W=1 mm. These two illustrate that the mixing in the burner of W=1mm performs better.

Due to the shrunk flow and weaker performance of mixing in W=2 mm(comparing with W=1 mm at the same flow rate), in the combustion tests diffusion flames are frequently anchored at the exits of fuel slits. Thus, to establish rapidly mixed tubular flame at high oxygen mole fraction, the slit should be thinner to inhibit the diffusion flame and promote mixing of fuel and oxidizer.

## 6.3 Damkolher number

At first, four cases of pure oxygen combustion in the lower pictures of Fig. 3.27, where the slit width W= 1mm and oxygen flow rate $Q_{O2}$= 4.0 $m^3_N$/h, are discussed on the requirement for the establishment of rapidly mixed tubular flame combustion.

According to the flow rates, the oxygen injection velocity is 69.44 m/s, while the methane velocities are 4.17, 5.21, 5.90 and 17.36 m/s. Based on the equivalence ratios the reaction times have been calculated in chapter 4. The mixing layer thicknesses, the mixing times and the Damkohler numbers for both types of flows are calculated and listed in Table 6.1.

For the case of $\Phi$ =0.12, the reaction time is 19000 μs; the average injection velocity of methane is much lower than the oxygen flow; in boundary layer type flow, the mixing layer thickness of methane is about four times as that of oxygen; based on the mixing layer thickness of methane, the mixing time is 1885μs, thus the Damkohler number is 0.099, which is much less than unity, suggesting that the mixing time is shorter than the reaction time. For the axisymmetric flow, the mixing layer thicknesses are much smaller than those of boundary layer type flow; the mixing time is 8.09 μs, which is about 1/200 that of the boundary layer type flow; the Damkohler number is also much smaller.

When $\Phi$ is increased to 0.15, the reaction time is significantly reduced to 2070 μs. While the mixing layer thickness of methane is slightly decreased, from 208 to 186 μm; the mixing time reduces to 1508 μs, and the Damkohler number is 0.725, which is also less than unity. For the axisymmetric flow, the mixing layer thicknesses are still much smaller; the mixing time is 6.47 μs and the Damkohler number is 0.0415, which is much smaller than that of boundary layer type flow and unity.

When $\Phi$ is further increased to 0.17, the reaction time is reduced to 981 μs; while the mixing layer thickness of methane changes little, decreasing from 186 to 175 μm; the mixing time reduces to 1331 μs; hence the Damkohler number is 1.356, which is larger than unity, suggesting that the mixing time is longer than the reaction time. For the axisymmetric flow, the Damkohler number is 0.0685, which is still much smaller than unity.

When $\Phi$ equals to 0.5, the reaction time is reduced to 32 μs; the mixing layer thickness of methane is 102 μm, which is twice as that of oxygen; the mixing time is 452 μs and the Damkohler number is 14.094, suggesting that the mixing time is longer than the reaction time. For the axisymmetric flow, the Damkohler number is 0.2412, which is still smaller than unity.

It is very important to note that in the cases when a tubular flame is established, i.e., $\Phi = 0.12 \text{ and } 0.15$, the Damkohler numbers for the boundary layer type flow are less than unity, suggesting that the mixing has completed before the onset of reactions, resulting in a tubular flame combustion of premixed type. In the cases when the tubular flame cannot be fully established, i.e., $\Phi = 0.17 \text{ and } 0.50$, Damkohler number become larger than unity, suggesting that the mixing has not yet completed before the onset of reactions. This means that $D_a$ based on the boundary layer type flow can well describe the establishment of tubular flame combustion. The Damkohler numbers for the axisymmetric type flow are much less than unity, and seem not related with the tubular flame establishment. This is reasonable since this flow is far away from the mixing region.

Table 6.1
Damkohler Number for pure oxygen combustion (W=1mm, $Q_{O2}$= 4.0$m^3_N$/h)

| $\Phi$ | $\tau_r$ [μs] | Boundary Layer Type Flow | | | | | | Axisymmetric Type Flow | | | | Tubular flame establishment |
|---|---|---|---|---|---|---|---|---|---|---|---|---|
| | | $V_{t\text{-O2}}$ [m/s] | $V_{t\text{-CH4}}$ [m/s] | $\delta_{\text{m-O2}}$ [μm] | $\delta_{\text{m-CH4}}$ [μm] | $\tau_m$ [μs] | $D_a$ | $\delta_{\text{m-O2}}$ [μm] | $\delta_{\text{m-CH4}}$ [μm] | $\tau_m$ [μs] | $D_a$ | |
| 0.12 | 19000 | 69.44 | 4.17 | 51 | 208 | 1885 | 0.099 | 3.34 | 55.7 | 8.09 | 0.0071 | Success |
| 0.15 | 2070 | 69.44 | 5.21 | 51 | 186 | 1508 | 0.725 | 3.34 | 44.5 | 6.47 | 0.0415 | Success |
| 0.17 | 981 | 69.44 | 5.90 | 51 | 175 | 1331 | 1.356 | 3.34 | 39.3 | 5.71 | 0.0685 | Failure |
| 0.50 | 32 | 69.44 | 17.36 | 51 | 102 | 452 | 14.049 | 3.34 | 13.4 | 1.94 | 0.2412 | Failure |

Table 6.2
Damkohler Number for tubular flame combustion under various $\beta$ (W=1mm, $Q_{Oxi}$= 10.0$m^3_N$/h)

| $\beta$ | $\Phi$ | $\tau_r$ [μs] | Boundary Layer Type Flow | | | | | | Tubular flame establishment |
|---|---|---|---|---|---|---|---|---|---|
| | | | $V_{t\text{-Oxi}}$ [m/s] | $V_{t\text{-CH4}}$ [m/s] | $\delta_{\text{m-Oxi}}$ [μm] | $\delta_{\text{m-CH4}}$ [μm] | $\tau_m$ [μs] | $D_a$ | |
| 0.684 | 0.18 | 11643 | 173.6 | 10.7 | 32 | 130 | 735 | 0.063 | Success |
| 0.684 | 0.278 | 475 | 173.6 | 16.5 | 32 | 105 | 475 | 1.000 | Success |
| 0.842 | 0.14 | 18882 | 173.6 | 10.2 | 32 | 133 | 767 | 0.041 | Success |
| 0.842 | 0.215 | 624 | 173.6 | 15.7 | 32 | 107 | 499 | 0.801 | Success |

Table 6.3
Damkohler Number W=2mm ($Q_{Oxi}$= 10.0$m^3_N$/h)

| $\beta$ | $\Phi$ | $\tau_r$ [μs] | Boundary Layer Type Flow | | | | | | Tubular flame establishment |
|---|---|---|---|---|---|---|---|---|---|
| | | | $V_{t\text{-Oxi}}$ [m/s] | $V_{t\text{-CH4}}$ [m/s] | $\delta_{\text{m-Oxi}}$ [μm] | $\delta_{\text{m-CH4}}$ [μm] | $\tau_m$ [μs] | $D_a$ | |
| 0.842 | 0.172 | 3232 | 86.8 | 6.3 | 43 | 161 | 1123 | 0.378 | Success |
| 0.842 | 0.215 | 624 | 86.8 | 7.8 | 43 | 144 | 899 | 1.44 | Failed |
| 1.0 | 0.136 | 18882 | 86.8 | 5.9 | 43 | 166 | 1196 | 0.191 | Success |
| 1.0 | 0.15 | 624 | 86.8 | 6.5 | 43 | 158 | 1084 | 0.521 | Failed, due to diffusion flame |

Based on the discussion of Damkohler number for pure oxygen combustion in W=1 mm, the Damkohler number calculated from the boundary layer type flow is also analyzed for oxygen-enriched air combustion, as listed in Table 6.2. The slit width is 1 mm and the oxidizer flow rate is 10.0 $m^3{}_N$/h. According to the results in Fig. 3.8, the upper stable tubular flame ranges for $\beta$ =0.684 and 0.842 are $\Phi$= 0.278 and 0.215, respectively. And for these two cases, the calculated Damkohler numbers based on the mixing layer thickness of methane are 1.0 and 0.801 (2nd and 4th rows), both of which are no more than unity. At lower equivalence ratio for each $\beta$, the Damkohler number is less than unity and stable tubular flame has been obtained. These results illustrate that the Damkohler number based on the boundary layer type flow is also valid to quantify the establishment of oxygen-enriched air tubular flame combustion.

Finally, the Damkohler number for the cases in W= 2 mm is discussed according to the stable tubular flame range plotted in Fig. 3.8. For the case of $\beta$=0.842, the stable tubular flame could be obtained up to $\Phi$= 0.172, and the Damkohler number based on the boundary layer type flow is 0.378. At $\Phi$= 0.215, $D_a$ becomes larger than unity and tubular flame is failed to establish, while that in W=1 mm tubular flame has been obtained. For $\beta$ =1.0, the stable tubular flame is obtained up to $\Phi$= 0.136, where $D_a$ = 0.19. With an increase of overall equivalence ratio to 0.15, the Damkohler number is 0.52, less than unity, however, tubular flame has not been obtained due to the establishment of diffusion flames at the exits of fuel slits. It can be seen that the discussion on Damkohler number is also very useful for W= 2 mm. However, only at low equivalence ratios, where diffusion flame has been inhibited and also the Damkohler number is less than unity, rapidly mixed tubular flame could be achieved.

## 6.3 Summary

Slit width of the burner should be thin to increase mixing and inhibit the diffusion flame. Based on the calculated reaction time and estimated mixing time, the Damkohler number has been yielded to successfully quantify the requirement of rapidly mixed oxygen enhanced tubular flame combustion. The following are concrete conclusions:

(1) Slit width of the burner should be much thin to inhibit diffusion flame and promote mixing of fuel and oxygen.

(2) The Damkohler number based on the boundary layer type flow gives useful insights on success/failure of rapidly mixed type tubular flame combustion. That is, for W= 1mm, the Damkohler number is less than unity, the mixing is completed before the onset of reactions, resulting in tubular flame combustion; for W= 2 mm, except that the Damkohler number should be less than unity, the diffusion flame should also be inhibited to achieve tubular flame combustion.

(3) The Damkohler number based on the axisymmetric flow failed to interpret the requirement due to far away from the mixing region.

# Chapter 7 Conclusions

In this study, an inherently safe technique, rapidly mixed oxygen enhanced tubular flame combustion has been proposed to save energy and reduce the $CO_2$ emissions. Demands for energy saving and lower $CO_2$ emissions, development of tubular flame combustion and oxygen enhanced combustion are overviewed. Oxygen enriched-air combustion under various oxygen mole fractions and pure oxygen combustion have been experimentally investigated with the rapidly mixed tubular flame technique. To quantify the requirement for rapidly mixed oxygen enhanced tubular flame combustion, reaction time has been numerically calculated while mixing time is estimated to yield the Damkohler numer. Based on the analytical results obtained from experimental analysis and numerical calculations the following results are obtained.

In Chap. 3 [**Flame Characeristics of Rapidly Mixed Oxygen Enhanced Tubular Flame Combustion**], under various oxygen mole fractions (including pure oxygen), the flame characteristics including flame appearances, inflammability limit, stability and oscillatory combustion have been experimentally investigated, and the following results are obtained.

(1) When the oxygen mole fraction in oxidizer is less than 40%, rapidly mixed tubular flame combustion of methane/oxygen-air could be achieved within flammable range, which has almost the same flame appearances as that of methane/air.

(2) When the oxygen mole fraction is increased to high value, say, above 77%, diffusion flames are anchored at the exits of the fuel slits, which inhibit the

mixing of fuel and oxidizer, resulting in intense oscillatory combustion. With a decrease of equivalence ratio, stable tubular flame is obtained, whose range is limited at the vicinity of lean limit.

(3) With an increase of oxygen mole fraction, stable tubular flame range in equivalence ratio becomes narrower while the oscillatory combustion range enlarges; the upper limit of stable tubular flame in W = 1 mm is larger than that of W = 2 mm, while the lean limits are almost the same.

(4) As for pure oxygen combustion, in the burner of W= 2 mm, diffusion flames are anchored at the exits of fuel slits interrupting the mixing of fuel and oxygen. By increasing the flow rate, hence increasing injection velocity, the diffusion flame cannot be totally inhibited and intense oscillatory combustion occurs.

(5) For W= 1 mm, when equivalence ratio is large, turbulent combustion become dominant; with a decrease of equivalence ratio, stable tubular flame combustion is obtained and remained until extinction. Under various oxygen flow rates, stable tubular flame ranges are examined, which is about 0.11 ~ 0.18 in equivalence ratio.

(6) The oscillatory combustions for oxygen-enriched air ($\beta = 0.661$ and 0.868) and pure oxygen are tested, respectively. The pressure fluctuations are almost over ± 10 kPa. And the oscillatory combustion seems belong to the acoustic resonance of axial mode.

In Chap. 4 [**Numerical Calculation of Burning Velocities and Reaction Time**], the burning velocity and reaction time are computed with the Chemkin Premix code, and the following results are obtained.

(1) The burning velocities of methane/oxygen-air mixtures under various oxygen

mole fractions and equivalence ratios are computed and the results show good agreements with experimental data.

(2) The burning velocities and flame temperature of $CH_4/O_2$-$CO_2$, $H_2/O_2$ and $C_3H_8/O_2$ are summarized for oxy-fuel combustion.

(3) Laminar flame thickness is computed through the temperature profile obtained along with the burning velocity calculation.

(4) The reaction time is calculated. For methane/oxygen mixture, with an increase of equivalence ratio, the reaction time reduces rapidly.

In Chap. 5 [**Mixing Process Analysis in the Rapidly Mixed Type Tubular Flame Burner**], the mixing layer thicknesses are examined under the same and different flow rate of the seeded flow and non-seeded flow, and the following results are obtained.

(1) There exist two types of flows, a boundary layer type flow near the exits of the slits close to the wall, and an axisymmetric potential flow around the axis of rotation;

(2) The mixing layer thickness in the boundary layer type flow is proportional to the inverse square root of injection velocity; while for the axisymmetric flow, the thickness is in proportion to the inverse value of injection velocity. The coefficients of both type flows are discussed in three types of burners, respectively.

(3) For the mixing layer with injection velocity of seeded flow half of that the non-seeded flow, the thicknesses in boundary layer type flow are examined. For W=2 and 1 mm, the mixing thickness could also be roughly calculated through the coefficients obtained under the same injection velocity but use the lower injection velocity (seeded flow).

(4) Mixing time has been calculated by the mixing layer thickness of the flow with lower injection velocity.

In Chap. 6 [**Discussion on the Requirement for Rapidly Mixed Oxygen Enhanced Tubular Flame Combustion**], with calculated reaction time and estimated mixing time, the Damkohler number is yielded to quantify the requirement for rapidly mixed oxygen enhanced tubular flame combustion. The following results are obtained:

(1) Slit width of the burner should be much thin to inhibit diffusion flame and promote mixing of fuel and oxygen.

(2) The Damkohler number based on the boundary layer type flow gives useful insights on success/failure of rapidly mixed type tubular flame combustion. That is, for W= 1mm, the Damkohler number is less than unity, the mixing is completed before the onset of reactions, resulting in tubular flame combustion; for W= 2 mm, except that the Damkohler number should be less than unity, the diffusion flame should also be inhibited to achieve tubular flame combustion.

(3) The Damkohler number based on the axisymmetric failed to interpret the requirement due to far away from the mixing region.

Finally, several recommendations are made for future researches in this field. As for the measurements of pressure fluctuations for oscillatory combustion, further measurements should be carefully conducted from two aspects: (a) try different the test positions and adjust the distance between the pressure sensor and flame; (b) measure the flame temperature, to provide accurate sound speed for resonance mode analysis.

The mixing layer thicknesses under different injection velocity ratios (flow rates) of seeded and non-seeded flow, like 2/3 or 1/3, would be further examined to yield more general results.

# References

---

[1] IEA, Energy Technology Perspective 2010, 2010.

[2] Ahmed F. Ghoniem, *Needs, resources and climate change: Clean and efficient conversion technologies*, Prog. Energy Combust. Sci. 37 (2011) 15-51.

[3] Lei Chen, Sze Zheng Yong, Ahmed F.Ghoniem, *Oxy-fuel combustion of pulverized coal: Characterization. fundamentals, stabilization and CFD modeling*. Prog. Energy Combust. Sci. 38(2012) 156-214

[4] Christopher R. Shaddix, Alejandro Molina, *Fundamental investigation of NOx formation during oxy-fuel combustion of pulverized coal*, Proc. Combust. Inst. 33 (2011) 1723–1730.

[5] Nobel Laureate Rick Smalley, April 2004, Testimony to U.S. Senate

[6] U.S. Energy Information Administration, *International Energy Outlook 2011*, Report Number: DOE/EIA-0484(2011).

[7] Baukal, C.E. ,Oxygen-Enhanced Combustion,CRC Press, Boca Raton, FL, 1998.

[8] Anders Lyngfelt, Bo Leckner, Tobias Mattisson, *A Fluidized-bed Combustion Process with Inherent $CO_2$ Separation; Application of Chemical-looping Combustion*, Chemical Engineering Science 56 (2001) 3101–3113.

[9] MohammadM. Hossain, Hugo I. de Lasa, *Chemical-looping Combustion (CLC) for Inherent $CO_2$ Separations—a Review*, Chemical Engineering Science 63 (2008) 4433 – 4451.

[10] Baukal, C. E., Jr., *Heat Transfer in Industrial Combustion*, CRC Press, Boca Raton, p.46 (2000).

[11] Nishimura, M., Suyari, M., Suzuki, T., and Takagi,T., *Studies on Fuel Savings and NOx Reduction Related to Oxygen-enriched Air Combustion*, Kobe Steel Engineering Reports, vol.51, No.2, pp.8-12 (2011).

[12] Global CCS Institute 2011, *The Global Status of CCS: 2011*, Canberra, Australia.

[13] http://www.ipcc.ch/index.htm.

[14] T.F. Wall, *Combustion processes for carbon capture*, Proc. Combust. Inst. 31 (2007) 31–47.

[15] http://en.wikipedia.org/wiki/Carbon_capture_and_storage.

[16] http://www.globalccsinstitute.com/ .

[17] http://sequestration.mit.edu/index.html .

[18] Wang M., Lawal A., Stephenson P., Sidders J., Ramshaw C., *Post-combustion $CO_2$ capture with chemical absorption: a state-of-the-art review*, Chemical Engineering Research and Design, in press, Corrected Proof.

[19] Blamey J., Anthony E.J., Wang J., Fennell P.S. *The calcium looping cycle for large scale CO2 capture*, Prog. Energy Combust. Sci. 36 (2010),260-279.

[20] Thiruvenkatachari R., Su S., An H., Yu X.X. *Post Combustion $CO_2$ Capture by Carbon Fiber Monolithic Adsorbents*, Prog. Energy Combust. Sci. 35 (2009),438-455.

[21] Merkel T.C., Lin H., Wei X., Baker R.,*Power Plant Post-Combustion Carbon Dioxide Capture: An Opportunity For Membranes*, Journal of Membrane Science 359(2010), 126-139.

[22] P. Heil, D. Toporov, M. Forster, R. Kneer, *Experimental Investigation on the effect of $O_2$ and $Co_2$ on Burning Rate During Oxyfuel Combustion Of Methane*, Proc. Combust. Inst. 33 (2011) 3407-3413.

[23] A. Amato, B. Hudak, P. D'Souza, P. D'Carlo, D. Noble, D. Scarborough, J. Seitzman, T. Lieuwen, *Measurements and Analysis of CO and* $O_2$ *Emissions in* $CH_4/CO_2/O_2$ *Flames*, Proc. Combust. Inst. 33 (2011) 3399-3405

[24] M. Taniguchi, T. Shibata, H. Kobayashi, *Prediction of Lean Flammability Limit and Flame Propagation Velocity for Oxy-Fuel Fired Pulverized Coal Combustion*, Proc. Combust. Inst. 33 (2011) 3391-3398.

[25] P. Kutne, B.K. Kapadia, W. Meier, M. Aigner, *Experimental Analysis of the Combustion Behavior of Oxyfuel Flames in A Gas Turbine Model Combustion*, Proc. Combust. Inst. 33 (2011) 3383-3390.

[26] T. Wall, *Combustion Processes for Carbon Capture*, Proc. Combust. Inst.33 (2007) 31–47.

[27] S.J. Willams, L.A. Cuervo and M.A. Chapman, *High-Temperature Industrial Process Heating: Oyxnge-Gas Combustion and Plasma Heating Systems*, Gas Research Institute report GRI-89/0256, Chicago, July, 1989.

[28] C.E. Baukal, P.B. Eleazer and L.K. Farmer, *Basis for Enhancing Combustion by Oxygen Enrichment, Ind. Heating*, LIX (2), 22,1992.

[29] R.J. Harris, W. Horne and A. Williams, *High Intensity Oxy-Methane Combustion in a Jet-Mixing Burner*, Combustion. Flame 26 (1976) 311-321.

[30] Sébastien Yon, Jean-Charles Sautet, *Flame Lift-Off Height, Velocity Flow and Mixing of Hythane in Oxy-Combustion in a Burner With Two Separated Jets*, Applied Thermal Engineering, Vol.32, (2012) 83-92.

[31] A. Beltrame, P. Porshnev, W. Merchan-Merchan, A. Saveliev, A. Fridman, L.A. Kennedy, O. Petrova, S. Zhdanok, F. Amouri, and O. Charon, *Soot and NO*

*Formation in Methane–Oxygen Enriched Diffusion Flames*, Combust. Flame 124 (2001) 295–310.

[32] S.K. Choi, J. Kim, S.H. Chung and J.S. Kim , *Structure of the Edge Flame in a Methane–Oxygen Mixing Layer*, Combustion Theory and Modelling 13 (1) (2009) 39–56.

[33] S. Ishizuka, T. Motodamari, D.Shimokuri, *Rapidly Mixed Combustion in A Tubular Flame Burner*, Proc. Combust. Inst. 31 (2007) 1085-1092.

[34] Ishizuka, S., *On the Behavior of Premixed Flames in a Rotating Flow Field: Establishment of Tubular Flames*, Twentieth Symposium (International) on Combustion, The Combustion Institute, Pittsburgh, (1984), 287-294.

[35] Ishizuka, S., *An Experimental Study on Extinction and Stability of Tubular Flames*, Combust. Flame 75 (1989) 367-379.

[36] Kobayashi, H., Kitano, M., Otsuka, Y., Trans. Japan Soc. Mech. Engrs. 52(1986)3811-3817, in Japanese.

[37] Ishizuka, S., Lecture Note in Physics 299 (1988) 93-102.

[38] Kobayashi, H., Kitano, M. Otsuka, Y., Combust. Flame 76 (1989) 89-105.

[39] Sakai, Y., Ishizuka, S., Trans. Japan Soc. Mech. Engrs. 56 (1990) 292-299.

[40] Kobayashi, H., Kitano, M., Combust. Sci. Technol. 75 (1991) 227-239.

[41] Sakai, Y., Ishizuka, S., *Extinction characteristics of tubular flames diluted with nitrogen in a rotating stretched flow field*, Twenty-fourth Symposium (International) on Combustion, The Combustion Institute, Pittsburgh, (1992), 153-159.

[42] Kobayashi, H., Kitano, M., Combust. Sci. Technol. 89 (1993) 253-263.

[43] Yamamoto, K., Ishizuka, S., Hirano, T., *Effects of Rotation on the Stability and Structure of Tubular Flame*, Twenty-fifth Symposium (International) on Combustion, The Combustion Institute, Pittsburgh, (1994), 1399-1406.

[44] Takeno, T., Ishizuka, S., *A Tubular Flame Theory*, Combust. Flame 64 (1986) 83-98.

[45] Takeno, T., Nishioka, M., Ishizuka, S., *A Theoretical Study of Extinction of A Tubular Flame*, Combust. Flame 66 (1986) 271-283.

[46] Takeno, T., Ishizuka, S., Nishioka, M., Buckmaster, J.D., Springer Series in Chemical Physics 47 (1987) 302-309.

[47] Nishioka, M., Takeno, T., Ishizuka, S., *Effects of Variable Density on a Tubular Flame*, Combust. Flame 73 (1988) 287-301.

[48] Kobayashi, H., Kitano, M., Otsuka, Y., Combust. Sci. Technol. 57 (1988) 17-36.

[49] Libby, P.A., Peters, N., Williams, F.A., *Cylindrical Premixed Laminar Flames*, Combust. Flame 75 (1989) 265-280.

[50] Smooke, M.D., Giovangigli, V., *Extinction of Tubular Premixed Laminar Flames with Complex Chemistry*, Twenty-fourth Symposium (International) on Combustion, The Combustion Institute, Pittsburgh, (1992), 447-454.

[51] Yamamoto, K., Hirano, T., Ishizuka, S., *Effects of pressure diffusion on the characteristics of tubular flames*, Twenty-sixth Symposium (International) on Combustion, The Combustion Institute, Pittsburgh, (1996) , 1129-1135.

[52] Zhang, Y., Ishizuka, S., Zhu, Y., Kee, R.J., *The Effects of Rotation Rate on the Characteristics of Premixed Propane–Air Swirling Tubular Flame*, Proc. Combust. Inst. 31 (2007) 1101-1107.

[53] Kee, R.J., Colclasure, A.M., Zhu, H., Zhang, Y., *Modeling Tangential Injection into Ideal Tubular Flames*, Combust. Flame 152 (2008) 114-124.

[54] Zhang, Y., Ishizuka, S., Zhu, H., Kee, R.J., *Effects of Stretch and Pressure on the Characteristics of Premixed Swirling Tubular Methane-Air Flames*, Proc. Combust. Inst. 32 (2009) 1149-1156.

[55] Ishizuka, S., *Characteristics of Tubular Flame*, Prog. Energy Combust. Sci. 19 (1993) 187-226.

[56] Ishizuka, S., *Determination of Flammability Limits Using A Tubular Flame Geometry*, J. Loss Prevention 4 (1991) 185-193.

[57] Ogawa, Y., Saito, N., Liao, C., *Burner Diameter and Flammability Limit Measured By Tubular Flame Burner*, Twenty-seventh Symposium (International) on Combustion, The Combustion Institute, Pittsburgh, (1998), 3221-3227.

[58] Shimokuri, D., Ishizuka, S., *Flame Stabilization with a Tubular Flame*, Proc. Combust. Inst. 30 (2005) 399-406.

[59] Ishizuka, S., Hagiwara, R., Suzuki, M., Nakamura, A., Hamaguchi, O., Trans. Japan Soc. Mech. Engrs. 65(1999)3845-3852, in Japanese.

[60] Hagiwara, R., Okamoto, M., Ishizuka, S., Kobayashi, H., Nakamura, A., Suzuki, M., Trans. Japan Soc. Mech. Engrs. 66(200)3226-3232, in Japanese.

[61] Ishizuka, S., Shimokuri, D., Ishii, K., Okada, K., Takashi, K., Suzukawa, Y., *Development of Practical Combustion Using Tubular Flames*, J. Combust. Soc. Japan. 156 (2009) 104-113, in Japanese.

[62] CHEMKIN-PRO, Reaction Design: San Diego, 2008.

[63] Beer, J.M. and Chigier, N.A., *Combustion Aerodynamics*, Applied Science Publishers Ltd., London,1972.

[64] Syred, N. and Beer, J.M., *Combustion in Swirling Flow: a Review*, Combust. Flame 23 (1974) 143-201.

[65] Claypole, T.C. and Syred, N., *The Effect of Swirl Burner Aerodynamics on NOx Formation*, Proc. Combust. Inst. 18 (1981) 81-89.

[66] Kee, R. J., Grcar, J. F., Smooke, M. D. and Miller, J. A. *A Fortran Program for Modeling Steady Laminar One-Dimensional Premixed Flames*, Sandia National, Laboratories Report SAND85-8240 (1985).

[67] Kee, R. J., Dixon-Lewis, G., Warnatz, J., Coltrin, M. E., and Miller, J. A., *A FORTRAN Computer Code Package for the Evaluation of Gas-phase Multicomponent Transport Properties*, Tech. Rep. SAND86-8246, Sandia National Laboratories, 1986.

[68] Smith, G., Golden, D., Frenklach, M., Moriarty, N., Eiteneer, B., Goldenberg, M., Bowman, C. T., Hanson, R., Song, S., Gardiner, W., Lissianski, V., and Qin, Z., GRI-Mech. *– An Optimized Detailed Chemical Reaction Mechanism for Methane Combustion*, Tech. Rep. available at http: //www.me.berkeley.edu/gri_mech, Gas Research Institute, 1999.

[69] M. D. Smooke, J. A. Miller, and R. J. Kee, *Determination of adiabatic flame speeds by boundary value methods*, Combustion Science and Technology 34:79 (1983).

[70] Shimokuri, D., Eto, Y., Ishizuka, S. , *Effect of swirl intensity on the rapidly mixed tubular flame established in a 2-inch tubular flame burner*, 7th Asia-Pacific Conference on Combustion, National Taiwan University, Taipei, Taiwan, 24-27 May 2009.

[71] Shimokuri, D., Watanabe, D., Eto, Y., Wang, E., Shi, B., Ishizuka, S., *A fundamental investigation on the effect of the ejection velocity ratio on the characteristics of the rapidly mixed tubular flame combustion*, 8th Asia-Pacific Conference on Combustion, Hyderabad, India, December 2010

[72] Yamaoka, I., Tsuji, H., *Determination of burning velocity using counterflow flames*, Twentieth Symposium (International) on Combustion, The Combustion Institute, (1985), 1883-1892.

[73] Coward, C.F. and Jones, G.W. , *Limits of Flammability of Gases and Vapors* ,US Bureau of Mines, Bulletin 503,p.44 (1952).

[74] Tsuji, H., Nensho-Gensho-Ron (19), *Kikai – No – Kenkyu*, Vol29, No.12 (1977), 1451-1454.

[75] Tsuji, H., Nensho-Gensho-Ron (20), *Kikai – No – Kenkyu*, Vol.30, No.1 (1978), 59-64.

[76] Hirano, T., *Nen-Shou-Gaku*, Kaibundou, (1986), 189-191.

[77] Kishimoto K., Kateiyou-nensyouki-no-souon-to- shindou, *Nensyou - Kenkyu*, Vol. 101, (1995), 15-25.

[78] Gordon, A. and McBride, B. J.*, Computer Program for Calculation of Complex Chemical Equilibrium Compositions,* NASA Spec. Publ., 273 (1971).

[79] Ito, T., *Onkyo-Kougaku-Genron*, Corona, Tokyo, (1951), Vol.1, p.109.

[80] Shiraki, K., *Souon-Boushi-Sekkei-To-Simyureishon*, Ouyou-Gijutsu Shuppan, Tokyo, (1987), p. 31.

[81] Shimokuri, D., Shiraga, Y., Ishizuka, S., Ishii, K., Toh, H., *High-Frequency Oscillatory Combustion in Tubular Flame Burners*, Japan Soc. Mech. Engrs. 75(2009)1197-1204, in Japanese.

[82] Jahn, G., Der Zündvorgang in Gasgemischen(Dissertation), Oldenbourg, Berlin, 1934.

[83] Strehlow.R.A , *Fundamentals of Combustion,* McGraw-Hill, New York,1984.

[84] Scholte, T.G., Vaags, P.B., Combust.Flame 3 (1959), 495-501.

[85] Tanford, C., *The Role of Free Atoms and Radicals In Burner Flames*, Third Symp. on Combustion and Flame and Explosion Phenomena, Williams & Wilkins, (1949) 140-146.

[86] Golovina, E.S., Fyodorov, G.G., Sixth Symposium (International) on Combustion, Reinhold, (1957) 88-96.

[87] S.D. Tse, D.L. Zhu, C.K. Law, *Morphology and Burning Rates of Expanding Spherical Flames in* $H_2/O_2$*/Inert Mixtures up to 60 Atmospheres*, Proc. Combust. Inst.28 (2000), 1793-1800.

[88] O. C. Kwon, and G. M. Faeth, *Flame/Stretch Interactions of Premixed Hydrogen-Fueled Flames: Measurements and Predictions*, Combust. Flame 124 (2001) 590–610.

[89] R. Gunther and G. Janisch, *Measurements of Burning Velocity in a Flat Flame Front*, Combust. Flame 19 (1972) 49-53.

[90] Dixon-Lewis, G. *Arch. Combustionis* 4:279-295 (1984).

[91] R. Zitoun , B. Deshaies, *Burning Velocities of Rich* $H_2$-$O_2$ *Flames under Cryogenic Conditions*, Combust. Flame 109 (1997) 427-435.

[92] Chemical-Kinetic Mechanisms for Combustion Applications http://web.eng.ucsd.edu/mae/groups/combustion/sdmech/sandiego20051201/sandiego20051201_CK.txt, Mechanical and Aerospace Engineering (Combustion Research), University of California at San Diego (http://combustion.ucsd.edu).

[93] C.J. Sung, B. Li, C.K. Law, H. Wang, *Structure and Sooting Limits in Counterflow Methane/Air and Propane/Air Diffusion Flames from 1 to 5 Atmospheres*, Twenty-Seventh Symposium (International) on Combustion (1998) 1523-1530.

[94] T. Poinsot, D. Veyhante, *Theoretical and Numerical Combustion*, Edwards, Philadelphia, 2001, p.57.

[95] John R. Henry, *Recent research on Fuel injection and Mixing and Piloted-Ignition for Scramjet Combustors*, Symposium (International) on Combustion 12 (1969) 1175–1182.

[96] Joseph A. Schetz, Harold E. Gilreath, Stephen C. Lubard, *Fuelinjection and Mixing in A Supersonic Stream*, Symposium (International) on Combustion 12 (1969) 1141–1149.

[97] Changkook Ryu, Donghoon Shin, Sangmin Choi, *Effect of Fuel Layer Mixing in Waste Bed Combustion*, Advances in Environmental Research 5 (2001) 259-267.

[98] David Pallarès, Filip Johnsson, *Modeling of Fuel Mixing in Fluidized Bed Combustors*, Chemical Engineering Science 63 (2008) 5663- 5671.

[99] W. R. Hawthorne, D. S. Weddell, and H. C. Hottel, *Mixing and Combustion in Turbulent Gas Jets*, Third symposium on combustion, flame and explosion phenomena, Vol.3 (1949) 266-288

[100] Yin Zhao-qin, Zhang Hong-jun, Lin Jian-zhong, *Experimental Study on the Flow Field Characteristics in the Mixing Region of Twin Jets*, Journal of Hydrodynamics, Ser.b, 2007,19(3), 309-313

[101] C.M. Coats, *Coherent Structures in Combustion,* Prog. Energy Combusti.Sci. 22, (1996) 427–509.

[102] Eduardo Fernández-Tarrazo, Marcos Vera, Amable Liñán, *Lift off and blow off of a diffusion flame between parallel streams of fuel and air*, Combustion. Flame 144 (2006) 261–276.

[103] K. Hishida, A. Ando, M. Maeda, *Experiments on Particle Dispersion in A Turbulent Mixing Layer*, Int. J. Multiphase Folw, Vol. 18, No. 2 (1992), 181-194.

[104] Lyle M. Pickett, Jaal B. Ghandhi, *Structure of a Reacting Hydrocarbon-Air Planar Mixing Layer*, Combustion and Flame 132 (2003) 138–156.

[105] Chiuan-Ting Li, Keh-Chin Chang, Muh-Rong Wang, *PIV Measurements of Turbulent Flow in Planar Mixing Layer*, Experimental Thermal and Fluid Science 33 (2009) 527–537.

[106] H. GRUNDEL and H.E. FIEDLER, *The Mixing Layer Between Non-Parallel Streams*, Applied Scientific Research 51 (1993) 167-171.

[107] Michael W. Plesniak, Rabindra D. Mehta, James P. Johnston, *Curved Two-stream Turbulent Mixing Layers Revisited*, Experimental Thermal and Fluid Science (1996) 190–205.

[108] D.H. Wood, R.D. Mehta, S.G. Koh, *Structure of A Swirling Turbulent Mixing Layer*, Experimental Thermal and Fluid Science, 5 (1992) 196-202.

[109] Ruey-hung Chen and James F. Driscoll, *The Role of The Recirculation Vortex in Improving Fuel-Air Mixing Within Swirling Flames*, Symposium (International) on Combustion Vol.22 (1988) 531-540.

[110] Takashi Terasaki, Shigeru Hayashi, *The Effects of Fuel–Air Mixing on* $NO_x$ *Formation in Non-Premixed Swirl Burners*, Symposium (International) on Combustion 26 (1996) 2733–2739.

[111] T.S. Cheng, Y.C. Chao, D.C. Wu, T. Yuan, C.C. Lu, C.K. Cheng and J.M. Chang, *Effects of Fuel-Air Mixing on Flame Structures and* $NO_x$ *Emissions in Swirling Methane Jet Flames*, Symposium (International) on Combustion 27 (1998) 1229-1237.

[112] H. Schlichting, Boundary Layer Theory, 7th ed., McGraw-Hill, NewYork, 1979, p.40.

[113] D. Shimokuri, Y. Zhang, S. Ishizuka, PIV measurements on a 2-inch tubular flame burner, Proc. of the 6th Asia-Pacific Conference on Combustion, Nagoya, Japan, 2007, 154-157.

[114] S. McAllister, J.Y. Chen, A.C. Fernandez-Pello, Fundamentals of Combustion Processes, Springer, 2011, p.86, p.144-145.

[115] P. Koutmos, *A Damkohler Number Description of Local Extinction in Turbulent Methane Jet Diffusion Flames*, Fuel 78 (1999) 623–626.

[116] A.F. Ghoniem and G. Heidarinfjad, *Effect of Damkohler Number on the Reactive Zone Structure in a Shear Layer*, Combust. Flame 83(1991) 1-16

# Acknowledgements

I would like to express my deep gratitude to my supervisor, Professor Satoru Ishizuka, for his constant guide, academic direction, kind attention and strong supports during my Ph.D. course. Besides great efforts to broaden my horizons and deepen my insights in academic researches, Prof. Ishizuka also gives kind cares in my daily life. His inspiration and warm personality have won my highest respect. I also want to express my appreciation to Assistant Professor Daisuke Shimokuri for providing me plenty of expert advices during researches. Furthermore, I would like to express my sincere gratitude to the committee members, Professors Keiya Nishida, Yukihiko Matsumura, Takuma Endo, for their attentions on my graduation thesis.

Especially, I would like to appreciate Professor Xinyu Zhang in Chinese Academy of Sciences, for his kindness and numerous helps and encouragements both in academic research and normal life.

Moreover, I gratitude my colleagues in our lab group: Mr. Kowari, for providing me helps in the experiments; Mr. Yamashita, for his assistance in PIV measurement; special thanks go to Mr. Peng, Mr. Wang and Mr. Hu, for their big supports and helps in my experiments and daily life. Finally, I would like to thank other exceptional friends for their attention and supports.

Finally, I want to express my deepest appreciation to my family. I would like to dedicate this work to them for their everlasting love and consistent encouragement.